Title
MULTIPLE FREQUENCY EFFECTS IN WAVEGUIDE FREE-ELECTRON LASERS

Author
Sternbach, E.J.

Publication Date
1989-06-01

Lawrence Berkeley Laboratory
UNIVERSITY OF CALIFORNIA

Accelerator & Fusion Research Division

Multiple Frequency Effects in Waveguide Free-Electron Lasers

E.J. Sternbach
(Ph.D. Thesis)

June 1989

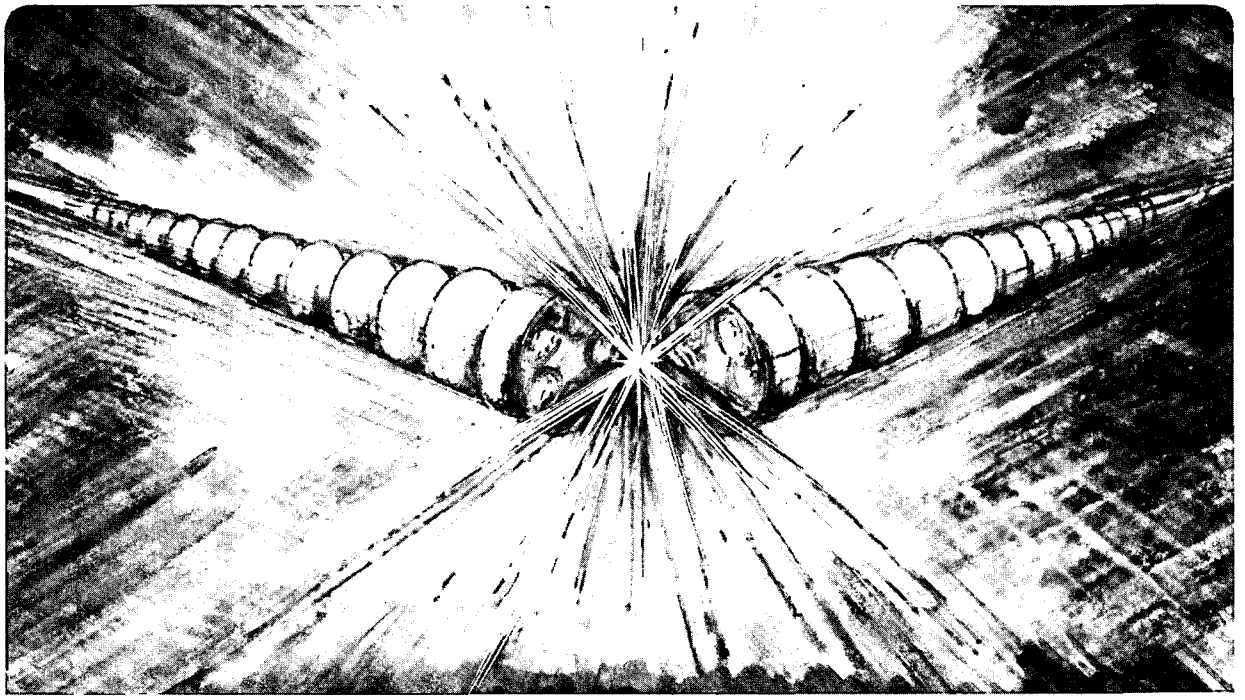

Prepared for the U.S. Department of Energy under Contract Number DE-AC03-76SF00098.

DISCLAIMER

LBL-27294

MULTIPLE FREQUENCY EFFECTS IN WAVEGUIDE FREE-ELECTRON LASERS

by

Efrem J. Sternbach*

Accelerator & Fusion Research Division
Lawrence Berkeley Laboratory
University of California
1 Cyclotron Road
Berkeley, California 94720

June, 1989

---

*Work performed under the auspices of the U.S. Department of Energy by the Lawrence Berkeley Laboratory under contract No. DE-AC03-76SF00098.

LBL-27294

MULTIPLE FREQUENCY EFFECTS IN WAVEGUIDE FREE-ELECTRON LASERS

by

Efrem J. Sternbach

ABSTRACT

For a wide variety of Free Electron Laser(FEL) applications, waveguides are used to confine and guide the radiation produced. In many of these applications, the dispersive effects in these waveguides can significantly alter the FEL physics from the case of free space propagation where the radiation phase and group velocity are both equal to c. The eikonal approximation usually used in FEL calculations breaks down in the regime where dispersion is an important effect. A formalism is developed with both integral and differential forms for dealing with an FEL in a dispersive waveguide. It is shown that in the limit of no dispersion and only a single radiation frequency, this formalism reduces to the standard FEL evolution equations. A computer code developed from the differential formalism is used to simulate waveguide FEL's.

The effects of dispersion on FEL sidebands are examined in depth. The dispersion caused by the waveguide can affect both the position and the gain of FEL sidebands. It is also possible to suppress the sideband instability completely.

The generation of FEL sidebands is shown to be a process similar in all respects to stimulated scattering. A theory based on the equations for parametric amplification in nonlinear optics is used to describe sideband generation. It is found that no more than four waves are necessary to explain the spectrum of FEL sidebands. Dispersion equations for three-wave and four-wave processes are derived and these are found to accurately predict sideband growth rates for the full waveguide computer simulation.

It is found that both upper and lower FEL sidebands can exhibit more than one peak in a waveguide. The FEL sideband instability is found to be primarily a three-wave process that drives the lower sideband. The upper sideband is not driven by a stimulated scattering process. It is found that the beating between the lower sideband and the fundamental is what drives the upper sideband spectrum.

---

*Work performed under the auspices of the U.S. Department of Energy by the Lawrence Berkeley Laboratory under contract No. DE-AC03-76SF00098.

Acknowledgements

I would like to thank my research advisor Andrew Sessler for his help and guidance during my graduate career. He has taught me how to choose and pursue research topics, which are the skills one hopes to learn by the time a PhD. is awarded. He also provided encouragement when the writing of this thesis appeared to be an impossible dream.

I would also like to thank Wulf Kunkel who acted as my academic advisor even after he officially had retired. His interest in my career and his good humor were a great encouragement.

Many thanks also go to the others on my thesis committee, Michael Lieberman, and Joel Fajans. Neither of them were required to perform any academic duties during the period I was writing this thesis, yet each kindly consented to read this thesis.

I am also indebted to those I have interacted with in the Beam Research Group at the Lawrence Livermore National Laboratory. In particular, I would like to thank Bill Fawley for discussions on numerical simulations of FEL's, and Bill Sharp for listening to my ideas on sidebands in waveguides and making useful suggestions.

At LBL, I was glad to be able to work with Don Hopkins. His calm demeanor and his attention to detail made him very easy to work with. He also ordered all the computer equipment and software that I requested. Carol Adams also helped out with her great enthusiasm. I also wish to thank David Whittum and Gil Travish for many useful

discussions and Jonathan Wurtele for getting me started on the MFECC computer system.

I also wish to thank my karate instructor Mohammed Ali Sharifi for his continued moral support and encouragement.

Even though I've learned a great deal in the last several years, it feels great to be finished with this thesis!

Work performed under the auspices of the U.S. Department of Energy by the Lawrence Berkeley Laboratory under contract No. DE-AC03-76SF00098.

Table of Contents

page

Chapter 1 Introduction 1

Chapter 2 Review of FEL Physics 9

2.1 **Basic Description of FEL's** 10

2.2 **KMR FEL Theory** 13

2.3 **Dynamics of the KMR FEL equations** 21

2.4 **Low energy corrections to KMR equations** 28
Derivation of equations.Averaging of equations. Hamiltonian for equations.

2.5 **Gain in an FEL** 35

2.6 **1-D Numerical Simulations of FEL's** 39
Untapered results. Bunching and gain. Effect of energy spread. Tapered results.

2.7 **Transverse Effects in FEL's** 52
Particle effects. Need for focusing. "Real" wiggler fields. Focussing and emittance. "Ted" poles on magnets. Effect of betatron oscillations on resonance. Effect of beam distribution on gain. Radiation effects. Waveguide modes. Optical guiding.

2.8 **2-D FEL simulations (FRED)** 61
Description of FRED. No guiding. With guiding.

page

Chapter 3 Basic formalism 70

3.1 FEL's in dispersive media 71

3.2 Derivation of the Waveguide Green's function 73

3.3 Derivation of Differential Equation Form 79

3.4 Reduction of Differential Equations to KMR Form . 89

Chapter 4 Effects of dispersion on single frequency FEL's 92

4.1 Waveguide corrections to the KMR theory 93
Effects on wiggler field strength. Effect on bucket height. Effect on gain magnitude. Effect on FEL resonance. Gain curve for ELF (plot of resonance intersections). Dispersion curve for an FEL.

4.2 Efficiency Enhancement in Waveguide FEL's 100

Chapter 5 Sidebands in Waveguide FEL's 111

5.1 Simple Model of sidebands 112

5.2 Description of Previous FEL Sideband Research 116
Kroll and Rosenbluth paper. Coulson simulations. Davidson and Wurtele. NRL work. 2-D sideband theory. Paper by Sharp and Yu.

5.3 Previous Work on FEL Sidebands in Waveguides ... 124
Waveguide model (Yu et al.). 1-D waveguide results. Description of results. Limitations of theory.

page

5.4 **Multiple Frequency Waveguide Simulation** 129
Description of equations. Effect of averaging. Effect of particle loading, Noise level.

5.5 **Physics from FEL Sideband Simulations** 140
Full simulation of waveguide code. ELF-like parameters; no taper. ELF-like parameters; with taper. Validity of "single-particle" simulations.

5.6 **FEL Sidebands as Stimulated Scattering** 151
Stimulated scattering description. Demonstration of stimulated scattering behavior.

5.7 **FEL Sideband Dispersion Analysis** 158

5.8 **Three-wave Analysis** 170
Dispersion relation and phase matching conditions. Derivation of three-wave scattering dispersion relation. Comparison to computer simulation.

5.9 **Four-wave Analysis** 182
Dispersion relation for 4-wave instability. Comparison to computer simulation. "Forced" frequencies.

5.10 **Explanation of ELF Sideband Results** 195
"Explanation" of previous ELF results. Notes on FEL startup with multiple input frequencies.

Chapter 6 Conclusion 204

References 209

List of Figures

page

Figure 2.1	Generic FEL	10
Figure 2.2	FEL resonance	12
Figure 2.3	Pendulum phase space	23
Figure 2.4	FEL phase space	24
Figure 2.5	FEL gain curve	37
Figure 2.6	Phase space evolution. FEL with no initial energy spread	42
Figure 2.7	Radiation evolution. FEL with no initial energy spread	43
Figure 2.8	Phase space evolution. FEL with large initial energy spread	44
Figure 2.9	Radiation evolution. FEL with large initial energy spread	45
Figure 2.10	Trapping in a tapered wiggler FEL	48
Figure 2.11	Fields in a tapered wiggler FEL	49
Figure 2.12	Electron beam emittance	53
Figure 2.13	"Ted" poles in wiggler magnets	55
Figure 2.14	Radiation guiding in an optical fiber	59
Figure 2.15	Radiation profile demonstrating radiation guiding	63
Figure 2.16	Radiation power and spot size with and without guiding	64
Figure 2.17	Radiation intensity profile	65
Figure 2.18	Radiation phase profile	66
Figure 2.19	Radiation intensity profile with guiding removed	67
Figure 2.20	Radiation phase profile with guiding removed	68
Figure 3.1	Linear wiggler FEL in a rectangular waveguide	73
Figure 3.2	Domain of integration for integral equation	79
Figure 3.3	Integration domain for forward traveling waves	82
Figure 3.4	Change to pondermotive coordinates	89
Figure 4.1	Dispersion curve for waveguide FEL	97
Figure 4.2	Radiation spectrum amplified from noise; waveguide FEL	99
Figure 4.3	Configuration to enhance waveguide FEL efficiency	101
Figure 4.4	Comparison of bucket area for two waveguide sizes	106
Figure 4.5	Comparison of trapping fraction for two waveguide sizes	107
Figure 4.6	Comparison of radiation power for two waveguide sizes	108
Figure 4.7	Comparison of the tapers for the different waveguide sizes	109
Figure 5.1	Motion of electron bunches in pondermotive well	113
Figure 5.2	Synchrotron oscillations in average gamma plot	114
Figure 5.3	Motion of electron bunches in phase space	115

page

Figure 5.4	Sideband growth rate for waveguide and paraxial equations	127
Figure 5.5	Regions of stability and instability for sidebands in waveguides	127
Figure 5.6	Average gamma. Comparison of averaged and unaveraged equations	133
Figure 5.7	2nd harmonic. Comparison of averaged and unaveraged equations	134
Figure 5.8	3rd harmonic. Comparison of averaged and unaveraged equations	135
Figure 5.9	Radiation spectra for different input noise powers	139
Figure 5.10	Total radiation power for untapered and tapered wigglers	141
Figure 5.11	Slow radiation phase for untapered and tapered wigglers	142
Figure 5.12	Sideband spectra for untapered and tapered wigglers	143
Figure 5.13	Comparison of simulations with different numbers of particles	146
Figure 5.14	Slow radiation phase. Single particle per bucket simulations	148
Figure 5.15	Sideband spectrum. Many particles per bucket simulation	149
Figure 5.16	Sideband spectra. Single particle per bucket with different initial phase	149
Figure 5.17	Three-wave processes	151
Figure 5.18	Four-wave processes	152
Figure 5.19	Harmonic oscillator model of sidebands	153
Figure 5.20	Only the lower sideband is unstable in a three-wave process	154-155
Figure 5.21	Spectrum of upper sideband from equilibrium with large synchrotron oscillation	156
Figure 5.22	Upper sideband can grow only at the expense of the synchrotron oscillation	156
Figure 5.23	Four-wave process produces upper and lower sidebands from equilibrium with no initial synchrotron oscillation	157
Figure 5.24	Sideband gain. Compare half spectrum simulation and three-wave dispersion analysis without slow radiation phase	174-175
Figure 5.25	Sideband gain. Compare half spectrum simulation and three-wave dispersion analysis with slow radiation phase	176-177
Figure 5.26	Imaginary part of sideband gain. Compare half spectrum simulation and three-wave dispersion analysis with slow radiation phase	178-180
Figure 5.27	Sideband location as a function of dispersion	181
Figure 5.28	Real and imaginary sideband gain. Compare half spectrum simulation and three-wave dispersion analysis without slow radiation phase	185
Figure 5.29	Real and imaginary sideband gain. Compare full spectrum simulation and three-wave dispersion analysis with slow radiation phase	186
Figure 5.30	Full sideband spectrum with identification of peaks	188
Figure 5.31	Spectra for forced beat frequencies	191

page

Figure 5.32	Radiation power for forced beat frequencies	192
Figure 5.33	Startup gain curve for ELF sideband experiment	196
Figure 5.34	Radiation power for single input frequency	198
Figure 5.35	Radiation power for two input frequencies. Second frequency is on initial gain curve	199
Figure 5.36	Power for frequencies on and off initial gain curve	200
Figure 5.37	Spectra for second input frequency off initial gain curve and on sideband peak	201

List of Tables

		page
Table I	FEL simulation parameters	40
Table II	Parameters for optical guiding simulations	69
Table III	Parameters for efficiency enhancement simulations	105
Table IV	ELF parameters	132
Table V	Parameters for sideband simulations	140
Table VI	Parameters for single particle per bucket sideband runs with different waveguide heights	172
Table VII	Parameters for ELF sideband experiment	195

Chapter 1

Introduction

1 Introduction

It has been just over a dozen years since the operation of the first Free-Electron Laser(FEL) by John Madey and his group at Stanford[59]. In that time, great strides have been made in building and understanding FEL's. FEL's of high efficiency[61] and short wavelength[60] have been demonstrated. The potential of the FEL is only just now beginning to be tapped and a greater theoretical understanding of FEL physics is necessary to design future applications.

An FEL uses some mechanism to induce a periodic transverse velocity modulation in an electron beam. This has several advantages over conventional lasers. First of all there is no medium to heat up and destroy. Therefore FEL's should be capable of unusually high powers. Since the FEL interaction does not involve transitions between quantum mechanical energy levels, the FEL can be tuned to a wide range of radiation frequencies. FEL's of various configurations have been demonstrated from the microwave regime[61] to the near UV regime[60].

Generally, magnetic fields are used to modulate the electron beam in a device called a wiggler. There are two general types of magnetic wigglers. Helical wigglers consist of two wires wrapped around a cylindrical guide. These wires are wrapped in a helix such that alternate wires along the length of the cylinder carry current in opposite directions. These helical wigglers are limited in strength by the current that can be carried by the wires and therefore tend to be used in small experiments. In a linear wiggler, a set of magnetic dipoles are arranged in a line with each successive dipole pointing in the opposite direction. Since ferromagnetic materials can be used in the manufacture of these wigglers, the fields can be made quite large. However it is harder to make linear wigglers with small periods, i.e. the spacing between the magnets can't be too small. Thus linear wigglers are a good choice for applications with large wiggler periods and fields.

An FEL can be run as either an amplifier or an oscillator. In regimes where good mirrors exist, an oscillator configuration can be desirable. This has the advantage of needing smaller gain in the FEL and therefore smaller beam current. In regimes where there are cheap low power radiation sources, the FEL might be run as a high gain amplifier. This gives one the advantage of using the low power source to achieve a radiation beam of high spectral purity which can then be amplified to extremely large

powers by the FEL. In the regimes where there are neither low power sources or good mirrors, the FEL can amplify the spontaneous emmision of the electron beam. This requires large beam currents to be practical. An FEL operating in this manner is analogous to a traditional laser acting as a superradiant amplifier.

As far as the electron beam interaction with the radiation is concerned, there are two general regimes of FEL operation. When electrostatic oscillations play a large roll in the longitudinal motion of the electrons, it is necessary to calculate the collective interaction of the electrons. This regime is called the *Raman* FEL regime. When the electron beam current is small, or the beam is sufficiently relativistic, space charge effects can be ignored. Relativistic effects can reduce the space charge interaction. In the electron's rest frame the electron density is smaller than the density in the lab frame. In the case that space charge effects can be neglected, the motion of each electron can be thought of as independent. The electron motion is determined only through external fields. This regime is known as the *Compton* FEL regime.

The theory of FEL's has evolved to a relative maturity. Some highlights are described here briefly. It was demonstrated by Colson that the FEL equations for particle motion can be written in the form of a pendulum equation[6]. This is really the basis for

almost all analyses of the electron motion in an FEL. The pendulum potential is the ponderomotive potential formed by the radiation field and the wiggler field. Kroll, Morton, and Rosenbluth took the formalism from accelerator physics where "buckets" of electrons are accelerated and applied it to FEL's where the electrons are bunched in FEL buckets and can be decelerated in a "tapered" wiggler[1]. The self consistent set of equations they derived are known as the KMR equations. Recently, Jonathan Wurtele extended these KMR equations to describe transverse modes in waveguides[5][21].

Waveguides are important since they provide an external means of guiding radiation. In real devices, waveguides are used for wavelengths down to 400μ[62]. This encompasses a wide range of frequencies of interest. For practical purposes, 2-D effects can be included for the radiation fields by expanding in a finite number of transverse modes. The interaction can be complicated since the modes have different transverse profiles and each transverse mode will move at a different velocity. Even for a single transverse mode, different frequencies can move at different speeds. This dispersion can have interesting effects since the group velocity and the phase velocity of the radiation are now different.

Of major importance in any coherent radiation source is the spectral purity of the output. Depending on the application, there will be some constraints on the linewidth of

the radiation produced. Also the coherence can effect the FEL performance. A large energy spread in the electron beam or some other effect reducing coherence can limit the total possible output power of a device. It is possible in some FEL's for parasitic frequencies to grow that widen the output spectrum. These parasitic frequencies are known as *sidebands* after the terminology of Kroll and Rosenbluth[42]. Aside from widening the spectrum, these sidebands can cause the electron motion to turn stochastic and thereby degrade FEL performance[47]. These sidebands are expected mostly to occur most often in FEL oscillators where they can grow easily from noise, although high power amplifiers should also be susceptible to sidebands.

One application that was expected to be susceptible to the sideband instability is the Two-Beam Accelerator(TBA). In this scheme, a microwave FEL was configured to power an accelerator structure. The FEL is meant to be long enough that any significant sideband growth would be catastrophic. It was noted that in a waveguide, the group velocity of the radiation could be set to be the same as the electron beam velocity. In this case, longitudinal instabilities would be expected to be suppressed since it would be difficult for information to travel along the beam. These observations were the motivation for the work in this thesis.

In this work, the longitudinal effects due to waveguides are studied for FEL's. The goal is to provide physical insight into multiple-frequency effects for FEL's in dispersive waveguides. Special emphasis is placed on the physics of FEL sidebands in waveguides.

In chapter 2, a review of general FEL physics is given. Using the KMR formalism[1], the basic equations of evolution for FEL's are derived. The dynamics of these equations are examined and it is shown that the equations can be written in a form analogous to the equations for a pendulum. It is shown that the entire set of FEL equations can be derived from a single Hamiltonian. Computer simulations are performed with the derived equations of evolution and some basic properties of FEL's are illustrated. Some 2-D effects in FEL's are described with special emphasis on the effect known as "optical guiding." 2-D computer simulations are used to illustrate the principles of optical guiding.

In chapter 3, a formalism is developed to systematically deal with a range of frequencies in each transverse mode in a waveguide. It is shown that a Green's function can be derived for the evolution of each transverse mode in a waveguide. From the integral equation that has been derived, a differential form of the equations is developed to follow discrete frequencies. The evolution for each frequency is described by two first order differential equations representing the radiation amplitude and phase for that frequency.

This differential form is shown to reduce to the KMR equations for radiation in an FEL when only a single radiation frequency is allowed.

In chapter 4, it is shown that the size of the waveguide can strongly affect FEL parameters. It is shown that the waveguide dimensions affect the resonance wiggler field, the gain, and the efficiency of the FEL. It is shown how waveguides can limit the efficiency of FEL's and how one might design a waveguide FEL to improve efficiency.

In chapter 5, sidebands in waveguides are studied in great depth. A review of previous work on sidebands is presented. A computer simulation based on the formalism of Chapter 3 is described. This computer simulation is used to show that the production of sidebands is a process analogous to that of stimulated scattering. Following this analogy, the FEL equations are altered to be similar in form to the equations used to study parametric amplification in nonlinear optics. It is shown that the physics of the sideband instability can be described as a combination of processes that involve three or four waves. In a waveguide it is shown that there can be more than the two sidebands that can be observed in free space. Lastly, the results of an attempted sideband experiment at the ELF facility at Livermore are explained. The use of the formalism for parametric amplification allows greater physical insight into the sideband process than previous analyses.

Chapter 2

Review of FEL Physics

2.1 Basic Description of FEL Physics

To begin, we start with a heuristic description of FEL physics. This physical picture will be used to motivate the calculations to be performed.

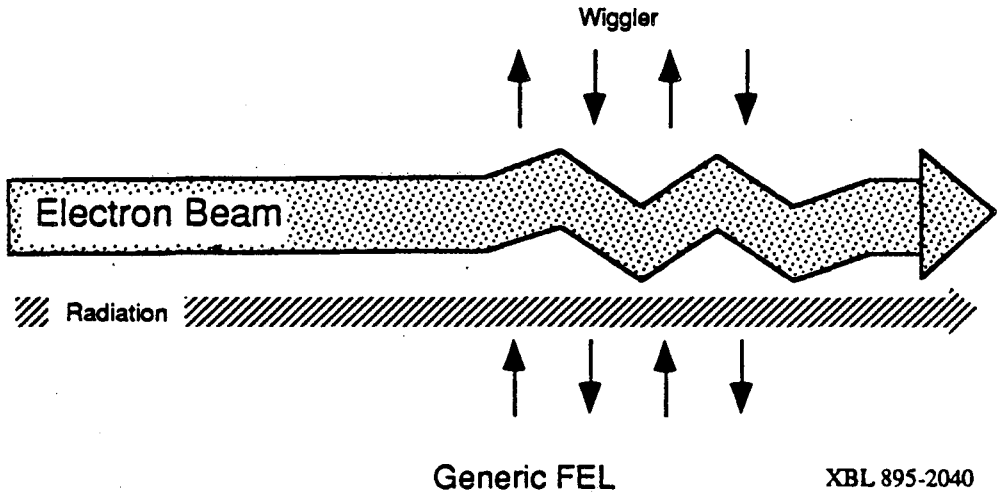

Figure 2.1 Diagram of configuration common to all FEL schemes. The wiggler is any scheme for modulating the transverse velocity of the electron beam in a periodic fashion.

In Fig. 2.1 is a general schematic of an FEL. It consists of an electron beam that is propagated through a periodic wiggler field. This wiggler field generally consists of a periodic magnetic field, although electromagnetic and electrostatic wigglers have also been proposed[40][41]. In the most general of terms, the purpose of the wiggler field is to

impart a periodic transverse velocity modulation to the electron beam. This transverse velocity modulation allows the electron beam to interact with a radiation field copropagating with the electron beam.

An FEL becomes interesting when there is a resonance between the electron beam modulation and the radiation field. In Fig. 2.2 there is a graphical representation of the primary FEL resonance. Here, in the distance required for an electron to undergo a single oscillation, one radiation wavelength passes over the electron. For the electron in the diagram, the force from the electric field of the radiation always opposes the motion of the electron.This electron will therefore lose energy. An electron that is one half oscillation behind the first electron will always experience a force from the radiation fields in the same direction as its motion.This electron will gain energy. With electrons gaining or loosing energy depending on their phase relative to the radiation field, bunches in the electron beam will be formed. These bunches are the basis for the strong coherent interaction in an FEL. If the electron beam energy is slightly too high for the resonance pictured in Fig. 2.2, then on average, more electrons will loose energy than will gain energy. This is the basis for FEL gain.

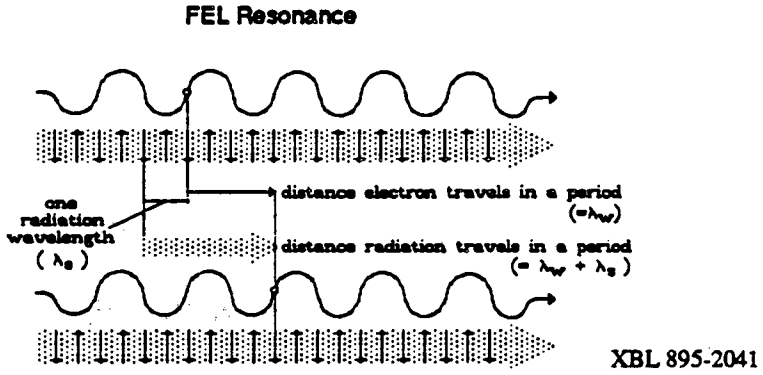

Figure 2.2 Diagram illustrating FEL resonance. One radiation wavelength passes over the electron for each oscillation of the electron.

2.2 Derivation of Highly Relativistic KMR Equations

We will use this simple one dimensional model to derive a set of equations to describe FEL evolution. The normalizations and approximations we use will produce a set of equations known in the FEL literature as the KMR(Kroll, Morton, and Rosenbluth) equations[1]. Other equivalent formulations have been derived[2][3], but here we will use the notation of the KMR equations. We will begin with

$$\frac{d\mathbf{p}}{dt} = q\left[\mathbf{E} + \frac{\mathbf{v}}{c} \times \mathbf{B}\right], \tag{2.2.1}$$

and $$\frac{\partial^2 \mathbf{A}}{\partial z^2} - \frac{1}{c^2}\frac{\partial^2 \mathbf{A}}{\partial t^2} = -\frac{4\pi}{c}\mathbf{J}\ , \tag{2.2.2}$$

where (2.2.1) is just the Lorentz force law for charged particles, and (2.2.2) is the electromagnetic wave equation in radiation gauge[4].

There are two types of magnetic wigglers that are normally used. A linear wiggler causes the electron trajectories to be confined to a plane. The electron trajectories and radiation modes are simple in this case, but the interaction of the two adds an extra term to the equations of motion. A helical wiggler has a cylindrical symmetry and the electron wiggles are in the radial direction. This type of wiggler has a more complicated geometry,

but the equations are simpler if a particular form of the fields are used. For the discussion here we will use the linear wiggler because the physical picture is simpler.

Let's start by defining the fields. We write the wiggler field as

$$\mathbf{B}_w = B_{w_y}(z)\,\hat{y}\,\cos\left[k_w z + \phi_w\right] \quad , \tag{2.2.3a}$$

and the radiation field as

$$\mathbf{E}_s = E_{s_x}(z,t)\,\hat{x}\,\cos\left[k_s z - \omega t + \phi_s(z,t)\right] \quad , \tag{2.2.3b}$$

$$\text{and} \quad \mathbf{B}_s = B_{s_y}(z,t)\,\hat{y}\,\cos\left[k_s z - \omega t + \phi_s(z,t)\right] \quad . \tag{2.2.3c}$$

For these definitions of the fields, the electron motion will be confined to the xz plane. The fields have all been defined with amplitudes that are allowed to vary slowly in z. By slowly varying amplitude we mean explicitly that if a field is defined $a(u)\sin\phi(u)$, then $\frac{da(u)}{du} << a(u)\frac{d\phi(u)}{du}$ .We now write (2.2.1) in terms of its nonzero components

$$\frac{dp_x}{dt} = q\left\{E_{s_x}\cos\left(k_s z - \omega t + \phi_s\right) - \frac{v_z}{c}\left[B_{s_y}\cos\left(k_s z - \omega t + \phi_s\right) + B_{w_y}\cos\left(k_w z + \phi_w\right)\right]\right\} \quad , \tag{2.2.4a}$$

$$\text{and} \quad \frac{dp_z}{dt} = q\left\{\frac{v_x}{c}\left[B_{s_y}\cos\left(k_s z - \omega t + \phi_s\right) + B_{w_y}\cos\left(k_w z + \phi_w\right)\right]\right\} \quad . \tag{2.2.4b}$$

If we use q=-e, and the relations for the vector potential $E_x = -\frac{1}{c}\frac{\partial A_x}{\partial t}$, and $B_y = \frac{\partial A_x}{\partial z}$,

then we can solve (2.2.4a). Thus

$$p_x = \frac{e}{c}\left[A_{s_x} \sin\left(k_s z - \omega t + \phi_s\right) + A_{w_x} \sin\left(k_w z + \phi_w\right)\right] \quad , \tag{2.2.5}$$

where $E_{s_x} = \frac{\omega}{c} A_{s_x}$, $B_{s_y} = k_s A_{s_y}$. and $B_{w_y} = k_w A_{w_y}$. The transverse momentum is just proportional to the total vector potential. With an appropriate choice of coordinates, the same result would have been obtained for a helical wiggler.

We now utilize the relativistic energy-momentum relationship

$$\mathcal{E}^2 = \gamma^2 m_e^2 c^4 = m_e^2 c^4 + p^2 c^2 \quad , \tag{2.2.6}$$

$$\text{or} \qquad \gamma = \left[1 + \frac{p^2}{m_e^2 c^2}\right]^{\frac{1}{2}} \quad .$$

If we take the derivative of γ with respect to t and substitute from relations (2.2.4) and (2.2.5), we obtain

$$\frac{d\gamma}{dt} = -\frac{\omega a_s a_w}{2\ \gamma}\left\{\sin\left[(k_s + k_w)\, z - \omega t + \phi_s + \phi_w\right] - \sin\left[(k_s - k_w)\, z - \omega t + \phi_s - \phi_w\right]\right\} \quad , \tag{2.2.7}$$

where we have introduced the normalizations $a_s = \frac{e}{m_e c^2} A_{s_x}$, and $a_w = \frac{e}{m_e c^2} A_{w_x}$, and we have used an approximation for (2.2.5)

$$p_x \cong \frac{e}{c} A_{w_x} \sin\left(k_w z + \phi_w\right) \quad . \tag{2.2.8}$$

which is almost always valid.

We define a phase, $\psi = (k_s + k_w)\, z - \omega t + \phi_s + \phi_w$, for the electron trajectories. An electron moving along with this phase will interact strongly with the radiation field. This phase is usually referred to as the ponderomotive phase of the electron since the right side of (2.2.7) is a direct result of the ponderomotive force. For simplicity, it is usually assumed that the electron beam is traveling somewhere near the velocity of the ponderomotive phase. Thus, the second sin term in (2.2.7) can be ignored since it will oscillate rapidly compared to the first sin term and therefore will not contribute on the average(For a more complete discussion of averaging, see section 2.4 of this chapter, or see ref. 5, chapter 3). At this point we would also like to change independent variables. One usually wishes to follow FEL evolution as a function of distance down the wiggler. Therefore we write $\frac{d}{dt} = v_z \frac{d}{dz}$. For most FEL's it is sufficient to set $v_z = c$ in this derivative. We obtain

$$\frac{d\gamma}{dz} = -\frac{\omega a_s a_w}{2c\ \gamma} \sin\psi \quad . \tag{2.2.9}$$

To complete the equations for particle motion, we need an equation for the evolution of ψ. Differentiating with respect to z gives

$$\frac{d\psi}{dz} = k_w + k_s + \frac{d\phi_s}{dz} - \frac{\omega}{v_z} \quad . \tag{2.2.10}$$

If we simply set $v_z = c$ in this equation we will remove all the physics. Therefore we will expand v_z and take the first order term. We note that $p_z = \gamma m_e v_z$, so along with the expression for p_z (2.2.8) and the relativistic energy-momentum relation(2.2.6) we can write v_z in terms of γ and z as

$$v_z = c\left[1 - \frac{1 + a_w^2 \sin^2\left(k_w z + \phi_w\right)}{\gamma^2}\right]^{\frac{1}{2}} \quad . \tag{2.2.11}$$

For most FEL parameters it is a good approximation to say that $a_w << \gamma$. In that case we can expand $1/v_z$ in eq. (2.2.10) to obtain

$$\frac{d\psi}{dz} = k_w + \frac{d\phi_s}{dz} - \frac{\omega}{2c\gamma^2}\left[1 + a_w^2 \sin^2\left(k_w z + \phi_w\right)\right] \quad , \tag{2.2.12}$$

where we have used $\frac{\omega}{c} = k_s$. If we now average over a wiggler period ($k_w z$), we obtain

$$\frac{d\psi}{dz} = k_w + \frac{d\phi_s}{dz} - \frac{\omega}{2c\gamma^2}\left[1 + \frac{a_w^2}{2}\right] \quad . \tag{2.2.13}$$

To complete the set of equations, we need to derive equations for the evolution of the radiation field. If we use (2.2.3) to describe the radiation field, then we need only use the x component of (2.2.2). We can define J_x as

$$J_x = - en_e \int v_x f_e(\gamma,\psi)\, d\gamma\, d\psi \quad ,$$

where f_e is the normalized distribution of the electron beam. If we use the normalizations for the fields introduced in (2.2.7), and if we use $v_x = \frac{p_x}{\gamma m_e}$ where p_x is given by (2.2.8), then the wave equation for the fields in an FEL is

$$\left[\frac{\partial^2}{\partial z^2} - \frac{1}{c^2}\frac{\partial^2}{\partial t^2}\right]\left\{a_s(z,t)\, \sin\left[k_s z - \omega t + \phi_s(z,t)\right]\right\} =$$

$$\frac{4\pi n_e e^2}{m_e}\frac{a_w}{c^2}\int \frac{\sin\left(k_w z + \phi_w\right)}{\gamma} f_e(\gamma,\psi)\, d\gamma\, d\psi \quad , \qquad (2.2.14)$$

where we are allowing the amplitude of the vector potential to be slowly varying in z. On the right side of (2.2.14) we can substitute $\omega_{pe}^2 = \frac{4\pi\, n_e e^2}{m_e}$, where ω_{pe} is the plasma frequency of the unbunched electron beam.

We now invoke the the *eikonal* approximation[28] which allows us to drop second derivatives. Then (2.2.14) becomes

$$\frac{da_s(z,t)}{dz}\cos\left[k_s z - \omega t + \phi_s(z,t)\right] - a_s(z,t)\frac{d\phi_s(z,t)}{dz}\sin\left[k_s z - \omega t + \phi_s(z,t)\right] =$$

$$\frac{\omega_{pe}^2 a_w}{2k_s c^2}\int \frac{\sin\left(k_w z + \phi_w\right)}{\gamma} f_e(\gamma,\psi)\, d\gamma\, d\psi \quad . \tag{2.2.15}$$

Next, both sides are multiplied by $\cos[\, k_s z - \omega t + \phi_s]$. We then use the definition of ψ and perform an average over z. This gives

$$\frac{da_s(z)}{dz} = \frac{\omega_{pe}^2 a_w}{k_s c^2}\left\langle \frac{\sin\psi}{\gamma} \right\rangle \quad . \tag{2.2.16}$$

Multiplying (2.2.15) by $\sin[\, k_s z - \omega t + \phi_s(z)]$ and averaging gives

$$\frac{d\phi_s(z)}{dz} = \frac{\omega_{pe}^2 a_w}{a_s k_s c^2}\left\langle \frac{\cos\psi}{\gamma} \right\rangle \quad . \tag{2.2.17}$$

The brackets in (2.2.16) and (2.2.17) represent an average over the particles.

We have now derived a full set of equations for following FEL evolution in one dimension. Rewriting them in one place for reference, they are

$$\frac{d\gamma_j}{dz} = -\frac{\omega}{2c}\frac{a_s a_w}{\gamma_j}\sin\psi_j \quad , \tag{2.2.18a}$$

$$\frac{d\psi_j}{dz} = k_w + \frac{d\phi_s}{dz} - \frac{\omega}{2c\gamma_j^2}\left[1 + \frac{a_w^2}{2}\right] \quad , \tag{2.2.18b}$$

$$\frac{da_s}{dz} = \frac{\omega_{pe}^2 a_w}{k_s c^2}\left\langle \frac{\sin\psi}{\gamma} \right\rangle \quad , \tag{2.2.18c}$$

$$\frac{d\phi_s}{dz} = \frac{\omega_{pe}^2 a_w}{a_s k_s c^2}\left\langle \frac{\cos\psi}{\gamma} \right\rangle \quad , \tag{2.2.18d}$$

where the subscript j refers to the fact that there are many particles to follow in an ordinary FEL. If there are N particles to follow, then eqs. (2.2.18) represent 2N+2 equations of motion. These equations are known as the KMR equations[1].

2.3 Dynamics of the KMR equations

In this section we will examine the dynamics of particle motion in an FEL. We will assume for the time that the electric vector potential a_s is a constant parameter. Treating the electric field as constant is not generally a good approximation, but it will allow us to introduce several useful concepts.

The first step is to search for equilibria by setting $\frac{d\gamma}{dz} = \frac{d\psi}{dz} = 0$. From eqs. (2.2.18a) and (2.2.18b) we see that these conditions can be met if $\psi = 0$ or π, and if

$$\gamma_r^2 = \frac{\omega}{2ck_w}\left(1 + \frac{a_w^2}{2}\right) \quad , \tag{2.3.1}$$

where we have neglected $\frac{d\phi_s}{dz}$ compared to k_w, and we have denoted the value of γ at equilibrium as γ_r. If we expand γ around γ_r and keep only the largest nonzero terms, we obtain a set of equations identical to that of a pendulum. Using the notation $\gamma=\gamma_r+\delta\gamma$, these equations become

$$\frac{d\delta\gamma}{dz} = -\frac{\omega a_s a_w}{2c\,\gamma_r}\sin\psi \quad , \tag{2.3.2a}$$

$$\frac{d\psi}{dz} = \frac{\omega\,\delta\gamma}{c\gamma_r^3}\left[1 + \frac{a_w^2}{2}\right] \quad . \tag{2.3.2b}$$

For some analyses, the eqs. (2.3.2) are combined to form the "pendulum equation." This can be written

$$\frac{d^2\psi}{dz^2} + \frac{a_s a_w \omega^2}{2c^2\gamma_r^4}\left[1 + \frac{a_w^2}{2}\right]\sin\psi = 0 \quad . \tag{2.3.3}$$

These equations have been analysed in great detail by Colson [6] and Kroll, Morton , and Rosenbluth[1].

The equations (2.3.2) have the following Hamiltonian

$$H = \frac{\omega}{2c\gamma_r^3}\left[1 + \frac{a_w^2}{2}\right](\delta\gamma)^2 - \frac{\omega a_s a_w}{2c\ \gamma_r}\cos\psi \quad , \tag{2.3.4}$$

where $\frac{d\delta\gamma}{dz} = -\frac{\partial H}{\partial\psi}$, and $\frac{d\psi}{dz} = \frac{\partial H}{\partial\delta\gamma}$.

Since the form of these equations are identical to that of a pendulum, we can take the results from the standard analysis of a pendulum. If we have the following Hamiltonian

$$H = Fp^2 - G\cos q\ , \qquad \frac{dp}{dt} = -\frac{\partial H}{\partial q}, \quad \frac{dq}{dt} = \frac{\partial H}{\partial p}, \tag{2.3.6}$$

then the phase space orbits of the system are as shown in fig 2.3.

The first important point is that one equilibrium can be shown to be stable and one can be shown to be unstable. Around the stable equilibrium, the orbits are called *center orbits*. Those orbits close to the resonance point have a frequency of $\omega = \sqrt{2FG}$. As one goes further from the resonance point, one reaches the *separatrix*. All orbits inside of the separatrix close in upon themselves. All orbits outside the separatrix are open orbits. This separatrix has a height which is given by $p_{max} = \sqrt{\frac{2G}{F}}$ [7].

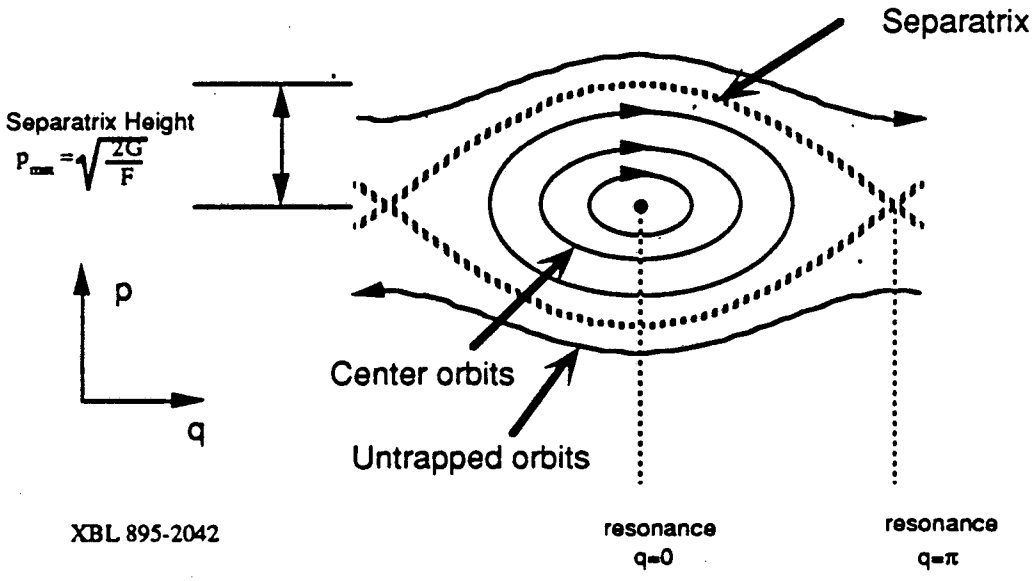

Figure 2.3 Pendulum Phase Space. Phase space for the Hamiltonian of (2.3.6). Orbits inside the separatrix are self connected and are therefore periodic. Orbits outside the separatrix are unconnected.

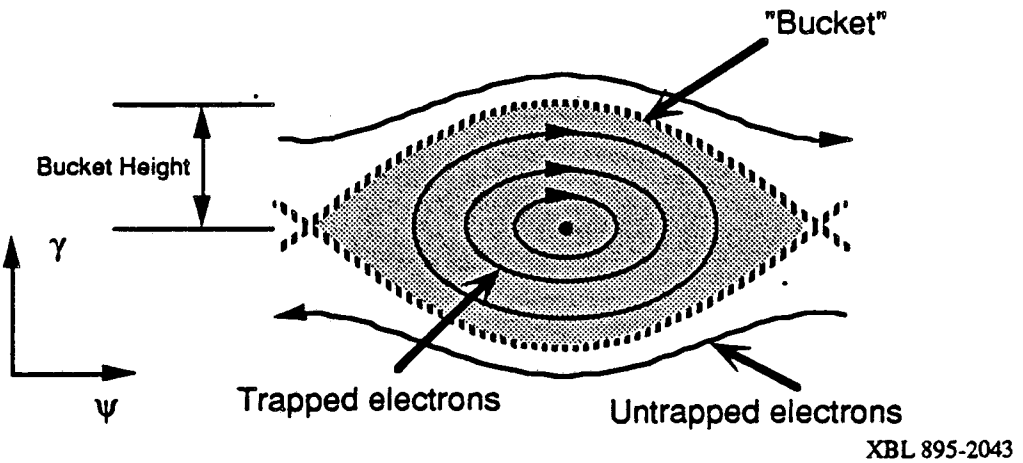

Figure 2.4 FEL Bucket. Linearized FEL equations produce a phase space like that of a pendulum. The use of the term "bucket" comes from accelerator physics.

Fig. 2.4 shows the same physics as Fig. 2.3, but the terminology has been altered to that used in the FEL literature. In accelerator physics, the area inside the separatrix, which is shaded in Fig. 2.4, is known as a *bucket*. All electrons inside the bucket are trapped in the ponderomotive well. These electrons can bunch on the length scale of the ponderomotive well and therefore interact coherently with the radiation. All electrons outside the bucket are untrapped. These electrons cannot interact coherently with the radiation. The frequency (actually wave number) at which electrons deep in the bucket orbit in phase space is known in the FEL literature as the synchrotron frequency. From (2.3.4), we can write down the synchrotron frequency and the bucket height as

$$k_{synch} = k_w \left[\frac{2a_s a_w}{1 + \frac{a_w^2}{2}} \right]^{\frac{1}{2}} , \qquad (2.3.7)$$

and $$\delta\gamma_{max} = \left[\frac{\omega a_s a_w}{c k_w} \right]^{\frac{1}{2}} , \qquad (2.3.8)$$

where we have used the expression for γ_r from (2.3.1).

At this point it is useful to introduce the concept of a tapered wiggler. The equations for a tapered wiggler FEL have been derived by Kroll, Morton, and Rosenbluth[1], and have been shown to be valid over a wide range of tapers[8] The location of the resonance point is determined by the relation (2.3.1). In a coherent FEL interaction, the electrons become bunched in the bucket and follow the phase space trajectories indicated in Fig. 2.4. Despite the fact that the bucket height increases as the radiation field increases, there will come a point at which the electrons on average collect in the bottom of the bucket. This point is where the average of the ponderomotive phases of the electrons becomes zero. From eq. (2.2.18c) one can see that the derivative of the electric field amplitude also becomes zero. Since the electrons are now lower in energy on the average than the resonance point, they will fall behind and the average over the ponderomotive phases will become negative. The electric field amplitude will then decrease. If the wiggler field a_w is a

constant, then this point marks the maximum amount of energy that can be removed from the electrons, or in other words, the FEL radiation field reaches saturation.

If we now allow the wiggler field to drop slowly(tapering the wiggler), thus slowly lowering the resonance point, then we find that most of the orbits inside the FEL bucket remain nearly periodic. What this means in practice is that if electrons are trapped in the bucket and the wiggler is then tapered, then the electrons will be decelerated along with the bucket. Since the resonance point can in practice be lowered a distance of many times the bucket height, a great deal more power can be extracted from the electrons. This will be demonstrated later in section 2.5 on FEL computer simulations.

Since we are discussing the dynamics of the FEL, it is worthwhile to note that the system of equations (2.2.18) can be rewritten so that all of the equations can be derived from a Hamiltonian, not just the particle equations[9][10][11]. One such Hamiltonian is

$$\mathbf{H} = \sum_{j}^{\#\ \text{particles}} k_w \gamma_j + \frac{\omega}{2c\gamma_j}\left\{ 1 + \frac{a_w^2}{2} + i\frac{a_w}{2}\beta\left[\mathcal{A}e^{i\varphi_j} + i\bar{\mathcal{A}}e^{-i\varphi_j}\right]\right\} \quad , \qquad (2.3.9)$$

where we have defined

$$\varphi_j = (k_w + k_s)z_j - \omega t_j \quad , \qquad (2.3.10a)$$

$$\mathcal{A} = i\beta^{-1} a_s e^{i\phi_s} \quad , \tag{2.3.10b}$$

with $$\beta = \sqrt{\frac{4\,\omega_{pe}^2}{\omega c\, k_s\, N_{particles}}} \quad ,$$

and $$\bar{\mathcal{A}} = i\mathcal{A}^* \quad . \tag{2.3.10c}$$

Here the definition for γ is unchanged. The canonical conjugates are γ_j and φ_j for each particle, and $\mathcal{A}$ and $\bar{\mathcal{A}}$ for the radiation field. $\mathcal{A}^*$ in eqn (2.3.10c) represents the complex conjugate of $\mathcal{A}$. The variable φ is the ponderomotive phase, ψ, minus the term for the slowly varying radiation phase ϕ_s. The equations of motion are obtained by the relations

$$\frac{d\gamma}{dz} = -\frac{\partial H}{\partial \varphi} \quad , \qquad \frac{d\varphi}{dz} = \frac{\partial H}{\partial \gamma} \quad ,$$

$$\frac{d\bar{\mathcal{A}}}{dz} = -\frac{\partial H}{\partial \mathcal{A}} \quad , \qquad \frac{d\mathcal{A}}{dz} = \frac{\partial H}{\partial \bar{\mathcal{A}}} \quad .$$

These can be seen to give the original equations (2.2.18) by substituting the original variables for the canonical variables.

2.4 FEL Equations in the Low Energy Limit

In this section the we develop a modified set of FEL equations. The standard KMR equations are the high energy limit of these modified equations[12]. The modified FEL equations are shown to be transformable to Hamiltonian form and to conserve energy. The equations developed here also include waveguide dispersion. For the sake of comparison to the KMR equations, we will confine the equations here to follow a single radiation frequency.

Most formulations of FEL equations assume that the velocity of the electron beam is approximately equal to c, the velocity of light, in the lab frame. For the equations to be developed here, we avoid this approximation. This is the regime where the dimensionless wiggler amplitude a_w is not extremely small compared to the γ of the electron beam. The ELF experiment at Livermore falls into this category[13].

A set of equations can be derived where the only assumption is that the dimensionless radiation amplitude a_s is much less than a_w . It is also possible to produce a

relatively simple set of equations that have been averaged over a wiggler period. These averaged equations can be shown to produce essentially the same results as the unaveraged equations, and to preserve energy conservation.

The high energy approximation in the KMR equations consists primarily of an expansion where $v_x/c \ll 1$. Here v_x is the x component of the electron velocity. The set of equations describing FEL evolution with z as an independent variable all have a factor of v_z in them. Explicitly

$$v_z^{-1} = \frac{1}{c}\left[1 - \frac{1}{\gamma^2} - \frac{v_x^2}{c^2}\right]^{-\frac{1}{2}} \cong \frac{1}{c}\left[1 - \frac{1 + a_w^2(z)}{\gamma^2}\right]^{-\frac{1}{2}}, \qquad (2.4.1)$$

where a_w is the dimensionless vector potential of the wiggler field. In the KMR equations(section 2.2), a_w is considered small compared to γ, so the square root is expanded and the series is truncated after terms that go as γ^2. This approximation is valid only when the wiggle velocity is a negligible fraction of c.

If we follow the derivation of the KMR equations without expanding v_z, and without performing any averages, then we arrive at the following low energy equations

$$\frac{d\gamma}{dz} = -\frac{\frac{\omega}{c} a_w a_s [\sin\psi - \sin(\psi - 2k_w z)]}{\sqrt{\gamma^2 - 1 - a_w^2 \sin^2 k_w z}} , \qquad (2.4.2a)$$

$$\frac{d\psi}{dz} = (k_w + k_s + \frac{d\phi}{dz}) - \frac{\frac{\omega}{c}\gamma}{\sqrt{\gamma^2 - 1 - a_w^2 \sin^2 k_w z}} , \qquad (2.4.2b)$$

$$\frac{da_s}{dz} = \frac{\omega_{p,eff}^2}{c^2 k_s} F^{mn} a_w \left[\left\langle \frac{\sin\psi}{\sqrt{\gamma^2 - 1 - a_w^2 \sin^2 k_w z}} \right\rangle - \left\langle \frac{\sin(\psi - 2k_w z)}{\sqrt{\gamma^2 - 1 - a_w^2 \sin^2 k_w z}} \right\rangle \right] , \qquad (2.4.2c)$$

$$\frac{d\phi_s}{dz} = \frac{\omega_{p,eff}^2}{c^2 k_s} F^{mn} \frac{a_w}{a_s} \left[\left\langle \frac{\cos\psi}{\sqrt{\gamma^2 - 1 - a_w^2 \sin^2 k_w z}} \right\rangle - \left\langle \frac{\cos(\psi - 2k_w z)}{\sqrt{\gamma^2 - 1 - a_w^2 \sin^2 k_w z}} \right\rangle \right] , \qquad (2.4.2d)$$

with

$$\omega_{p,eff}^2 = \frac{4\pi I e}{m_e c a b} , \quad \text{and} \quad F^{mn} = \frac{2 \cos\frac{m\pi}{2} \sin\frac{n\pi}{2}}{1 + \delta_{m0}} .$$

Here we have used the notation for an FEL in a waveguide. In free space, $\omega_{p,eff}$ would take the regular form for the plasma frequency of the electron beam and F^{mn} would go to 1. The only approximations made for these equations are that only a single radiation frequency is followed, and that $a_s << a_w$.

At this point we would like to average the above equations. This is important since if we wish to calculate a γ_r for this set of equations, we can only do so on the average. The equations can be averaged, but one must be careful because of the explicit z dependence in

the denominator of each equation. To begin, we expand the square root in the particle equations and keep only those terms where there is no explicit z dependence or where the z dependence goes as $2k_w z$. There are terms that go as multiples of $2k_w z$, but computer studies show that these terms are much smaller than the $2k_w z$ term. The expansion gives

$$\left[1 - \frac{1 + a_{w0}^2 \sin^2 k_w z}{\gamma^2}\right]^{-\frac{1}{2}} \cong K_1 - K_2 \cos 2k_w z \quad , \tag{2.4.3}$$

where

$$K_1 = 1 + \frac{1 + \frac{1}{2}a_w^2}{2\gamma^2} + \frac{3\left(1 + a_w^2 + \frac{3}{8}a_w^4\right)}{8\gamma^4} + \frac{15\left(1 + \frac{9}{8}a_w^2 + \frac{3}{2}a_w^4 + \frac{5}{16}a_w^6\right)}{48\gamma^6} + \ldots \quad , \tag{2.4.4a}$$

and

$$K_2 = \frac{a_w^2}{4\gamma^2} + \frac{3\left(a_w^2 + \frac{1}{2}a_w^4\right)}{8\gamma^4} + \frac{15\left(\frac{3}{2}a_w^2 + \frac{3}{2}a_w^4 + \frac{15}{32}a_w^6\right)}{48\gamma^6} + \ldots \quad . \tag{2.4.4b}$$

The particle equations can then be written as

$$\frac{d\gamma}{dz} = F\left[\sin\psi - \sin(\psi - 2k_w z)\right]\left[H_1 - H_2 \cos 2k_w z\right] \quad , \tag{2.4.5a}$$

$$\frac{d\psi}{dz} = \left(k_w + k_s + \frac{d\phi_s}{dz}\right) - \frac{\omega}{c}\left[K_1 - K_2 \cos 2k_w z\right] \quad , \tag{2.4.5b}$$

where

$$H_{1,2} = \frac{K_{1,2}}{\gamma} \quad , \quad \text{and} \quad F = \frac{-\omega a_s a_w}{2c} \, .$$

From these equations we expect that the solutions for γ and ψ are of the form

$$\gamma = \gamma_0 + \gamma_{2c} \cos(2k_w z) + \gamma_{2s} \sin(2k_w z) \quad , \tag{2.4.6a}$$

$$\psi = \psi_0 + \psi_{2s} \sin(2k_w z) \quad , \tag{2.4.6b}$$

where the coefficients are average values over a wiggler oscillation. For the current analysis, we will assume that $\gamma_0 >> \gamma_{2s}, \gamma_{2c}$. Substituting eqs. (2.4.6) into eqs. (2.4.5) and using the following Bessel function identities[14]

$$\sin (r \sin \theta) = 2 \sum_{n=0}^{+\infty} J_{2n+1} (r) \sin ((2n + 1) \theta) \quad , \tag{2.4.7a}$$

$$\cos (r \sin \theta) = J_0 (r) + 2 \sum_{n=0}^{+\infty} J_{2n} (r) \cos (2n \theta) \quad , \tag{2.4.7b}$$

we can perform a straightforward average on the equations of motion. Ignoring terms that depend explicitly on γ_{2s} and γ_{2c}, we obtain

$$\frac{d\gamma}{dz} = F \left\{ H_1 [J_0 (\psi_2) - J_1 (\psi_2)] + \frac{1}{2} H_2 J_0 (\psi_2) \right\} \sin \psi \quad , \tag{2.4.8a}$$

$$\frac{d\psi}{dz} = \left(k_w + k_s + \frac{d\phi_s}{dz} \right) - \frac{\omega}{c} K_1 \quad , \tag{2.4.8b}$$

with

$$\psi_2 = \frac{\omega K_2}{2 c k_w} \quad .$$

These are the appropriate, averaged particle equations that include the case of a low γ FEL. Through similar manipulations, the averaged field equations are found to be

$$\frac{da_s}{dz} = \frac{\omega_{p,eff}^2}{c^2 k_s} F^{mn} a_w \left\langle \left\{ H_1 [J_0(\psi_2) - J_1(\psi_2)] + \frac{1}{2} H_2 J_0(\psi_2) \right\} \sin\psi \right\rangle , \qquad (2.4.9a)$$

$$\frac{d\phi_s}{dz} = \frac{\omega_{p,eff}^2}{c^2 k_s} F^{mn} \frac{a_w}{a_s} \left\langle \left\{ H_1 [J_0(\psi_2) - J_1(\psi_2)] + \frac{1}{2} H_2 J_0(\psi_2) \right\} \cos\psi \right\rangle . \qquad (2.4.9b)$$

If we set $H_2 = 0$, and if we truncate H and K after their first terms, this reduces to the proper average for the regular KMR equations for a linear wiggler[5].

The low energy FEL equations have the same invariants as the high γ equations. For instance, eqs. (2.4.2) can be written in Hamiltonian form. If we make the following transformations

$$\mathcal{A} = i\beta^{-1} a_s e^{i\phi_s} \quad , \text{and} \quad \bar{\mathcal{A}} = i\mathcal{A}^* \quad , \qquad (2.4.10)$$

with $\beta = \sqrt{\dfrac{4\omega_{p,eff}^2 F^{mn}}{\omega c k_s N_{particles}}}$,

where $\mathcal{A}^*$ is the complex conjugate of $\mathcal{A}$, then $\mathcal{A}$ and $\bar{\mathcal{A}}$ will be canonical conjugate variables.

The Hamiltonian for an FEL without space charge is

$$H = \sum_{j}^{\#\ particles} (k_w + k_s)\,\gamma_j -$$

$$\frac{\omega}{c}\left\{\gamma_j^2 - 1 - a_w^2 \sin^2(k_w z) + i\,a_w\beta\left[\mathcal{A}\left(e^{i\varphi_j} - e^{i[\varphi_j - 2k_w z]}\right) + i\bar{\mathcal{A}}\left(e^{-i\varphi_j} - e^{-i[\varphi_j - 2k_w z]}\right)\right]\right\}^{\frac{1}{2}}, \tag{2.4.11}$$

where the variable φ is the same as that defined in (2.3.10a). This Hamiltonian is an invariant for the system and is valid for both high and low γ regimes. The equations of motion yield 2N equations for the particles and 2 equations for the fields. These equations can be seen to be physically identical to eqs. (2.4.2) by substituting the original variables ψ, a_s and ϕ_s into the equations.

The energy can also be shown to be an invariant of the system of eqs. (2.4.2). Through a careful integration of the fields, it can be shown that the energy in an FEL bucket is given by

$$\mathcal{E} = \sum_{j}^{N_{buc}} \gamma_j\, m\, c^2 + \frac{m^2 c^4\, a\, b\,(1 + \delta_{m0})\, k_s}{16\, e^2}\, a_s^2 \quad , \tag{2.4.12}$$

where the sum is over all the electrons in the bucket.

2.5 Gain in an FEL

In this section we write down some results for gain in an FEL. This subject has been covered exhaustively by others[6][15][16]. Here we will use the notation of Colson and Sessler[17].

The procedure is to take a set of equations for an FEL, eqs. (2.2.18) for instance, and to perturb these equations about an equilibrium. Most analyses take an unbunched electron beam with no energy spread as the equilibrium. Colson and Sessler start with the pendulum equation and the radiation field equation written in complex form with a normalized time as the independent variable.

From this analysis they derive a cubic dispersion relation with the form

$$\alpha_r^3 - i\nu_0\alpha_r^2 - i\frac{j}{2} = 0 \quad , \tag{2.5.1}$$

where the assumed form of the complex radiation field was $a = a_0 e^{-i\nu_0\tau} \sum_{r=1}^{3} e^{\alpha_r\tau}$. Here ν_0 is the initial phase velocity of the electron relative to the ponderomotive well, j is a normalized form of the current, and τ is a dimensionless time. Explicitly

$$v_0 = \frac{c}{L}\left[(k_w + k_s)\, v_0 - \omega\right] \quad ,$$

$$j = \frac{8N(\pi e a_w L)^2 n_e}{\gamma_r^3\, m_e c^2} \quad ,$$

and $\tau = \frac{c}{L}\, t$. To define a few more terms, L is the length of the wiggler, N is the number of wiggler periods, n_e is the electron number density, and v_0 is the original velocity of the electron beam.

To start, we wish to examine the regime where j is large. This is the high gain regime where the v_0 term is negligible. Here, the important real root is $\alpha_r = \frac{\sqrt{3}}{2}\left(\frac{j}{2}\right)^{1/3}$ which gives exponential growth. This is an important regime of interest for waveguide FEL's where one usually wishes to run as a high gain amplifier rather than as an oscillator.

There are, however, FEL's for which the high gain assumption is not valid. The full solution of (2.5.1) is necessary. The solution is given by

$$G(v_0) = j\frac{[2 - 2\cos v_0 - v_0 \sin v_0]}{v_0^3} = -\frac{j}{2}\frac{d}{dv_0}\left(\frac{\sin v_0/2}{v_0/2}\right)^2 \quad , \qquad (2.5.2)$$

with $G(v_0)$ given by

$$G(v_0) = \left[a^2_{final} - a^2_{initial}\right] / a^2_{initial} \quad .$$

The phase shift given by this solution is

$$\phi(\nu_0) = j\frac{[\,2\sin\nu_0 - \nu_0(1+\cos\nu_0)]}{\nu_0^3} \quad . \tag{2.5.3}$$

The gain function and the accompanying phase shift are illustrated in Fig. 2.5.

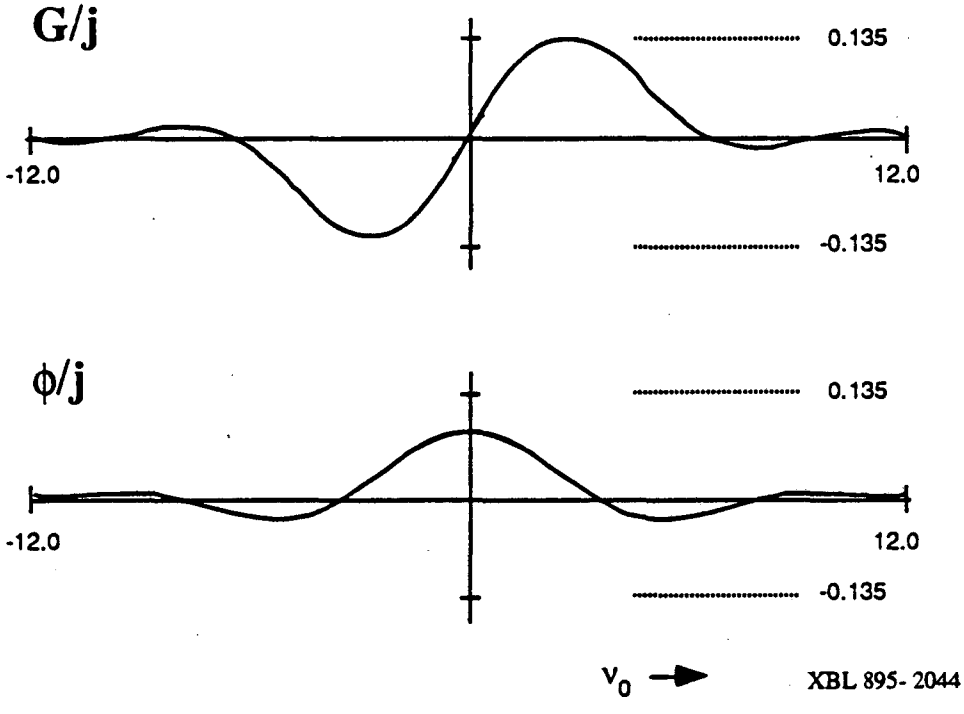

Figure 2.5 Plots of the real and imaginary parts of the gain in an FEL.

The first result from (2.5.2) is that the FEL gain goes as the derivative of the spontaneous emission spectrum $\left(\frac{\sin\nu_0/2}{\nu_0/2}\right)^2$. This result is usually referred to as Madey's theorem[18]. Another theorem for small signal gain attributed to Madey is that

$$\langle \gamma_{final} - \gamma_{initial} \rangle = \frac{1}{2}\frac{\partial}{\partial\gamma_{initial}}\langle (\gamma_{final} - \gamma_{initial})^2 \rangle \quad , \tag{2.5.4}$$

where the brackets < > represent an ensemble average of the particles. This relates the energy extracted by the FEL to the resulting spread in electron energies. This means that even a completely cold electron beam will have a temperature after transferring energy in an FEL.

It is worth noting that the results in this section can be arrived at through many different methods. Some have achieved the small gain results by following the particle trajectories and averaging over the initial electron distribution[6]. Others have used a Vlasov perturbation scheme[15]. This lends credibility to the idea that these results are physically correct and not just the result of a particular mathematical approximation.

2.6 1-D Numerical Simulations of FEL's

In this section we perform a numerical integration of the KMR equations (2.2.18). The integration is performed on a CRAY 2 computer at the Magnetic Fusion Energy Computer Center(MFECC) at Livermore California. The GEAR integration package utilizing the Adam's method was used. The simulation described in this section is used to illustrate some general features of FEL physics. The code used is similar to that developed by Prosnitz, Szoke, and Neil[19]

The parameters used for the simulation are similar to those of the ELF experiment at Livermore, California[13][20]. These are tabulated in Table I. The magnetic field value is a calculated quantity rather than an input parameter. It is calculated from the resonance gamma by eq. (2.3.1).

Some small modifications need to be made to equations (2.2.18) to model an FEL in a waveguide. The equations for a single transverse mode in an FEL waveguide are almost identical to (2.2.18)[5][21]. The changes are

Table I

Beam Energy	3.68 Mev
Beam Energy in γ	7.2
Beam Current	800 amperes
Wiggler wavelength	9.8 cm
Radiation frequency	34.6 GHz
Waveguide width	9.8 cm
Waveguide height	2.9 cm
Input radiation power	60 KWatts / TE^{01} mode
Wiggler Peak Field	4.09 KGauss

$$\omega_{pe}^2 \rightarrow \omega_{p,eff}^2 = \frac{8\pi I e}{m_e c a b} \frac{\cos\frac{m\pi}{2}\sin\frac{n\pi}{2}}{\left(1+\delta_{m0}\right)} \quad , \tag{2.6.1}$$

and

$$\frac{d\psi_j}{dz} = k_w + \delta k_s + \frac{d\phi_s}{dz} - \frac{\omega}{2c\gamma_j^2}\left[1+\frac{a_w^2}{2}\right] \quad . \tag{2.6.2}$$

Here, following Wurtele's notation, we substitute (2.6.1) for the plasma frequency in the radiation equations. It is to be substituted for ω^2_{pe} in eqs. (2.2.18c) and (2.2.18d). This is to make the form of the FEL equations in a waveguide the same as the form of the equations for free space. The expression (2.6.1) is not actually the effective plasma

frequency for an electron beam in a waveguide. In this expression, a is the waveguide width, b is the waveguide height, I is the beam current, and m and n represent the waveguide mode indices. eq. (2.6.2) is identical to (2.2.18b) with the addition of the term $\delta k_s = k_s - \omega/c$. This term accounts for the fact that the phase velocity of the radiation in a waveguide is different from that of radiation in a vacuum. In other words, δk_s results because $k_s \neq \omega/c$ in a waveguide.

In order to demonstrate the effect of energy spread on FEL gain, two cases are used. In the first case, $\Delta\gamma = 0$, and in the second case $\Delta\gamma = \pm 0.4$. These cases are run for an untapered wiggler with the parameters from Table I. These parameters are in the high gain regime as described in section 2.5. The results are shown in Figs. 2.6 -2.9.

Starting with Fig. 2.6, we can identify some general phenomena associated with FEL phase space evolution. In the beginning of the wiggler in Fig. 2.6a we see the particles take the shape of an inverted sine wave. This follows directly from eq. (2.2.18a) where the γ derivative goes as $-\sin\psi$. In Fig. 2.6b we see the FEL as it reaches saturation. The bulk of the electrons have reached the bottom of the bucket and are beginning to be reaccelerated. The diagram in Fig. 2.6d shows the phase

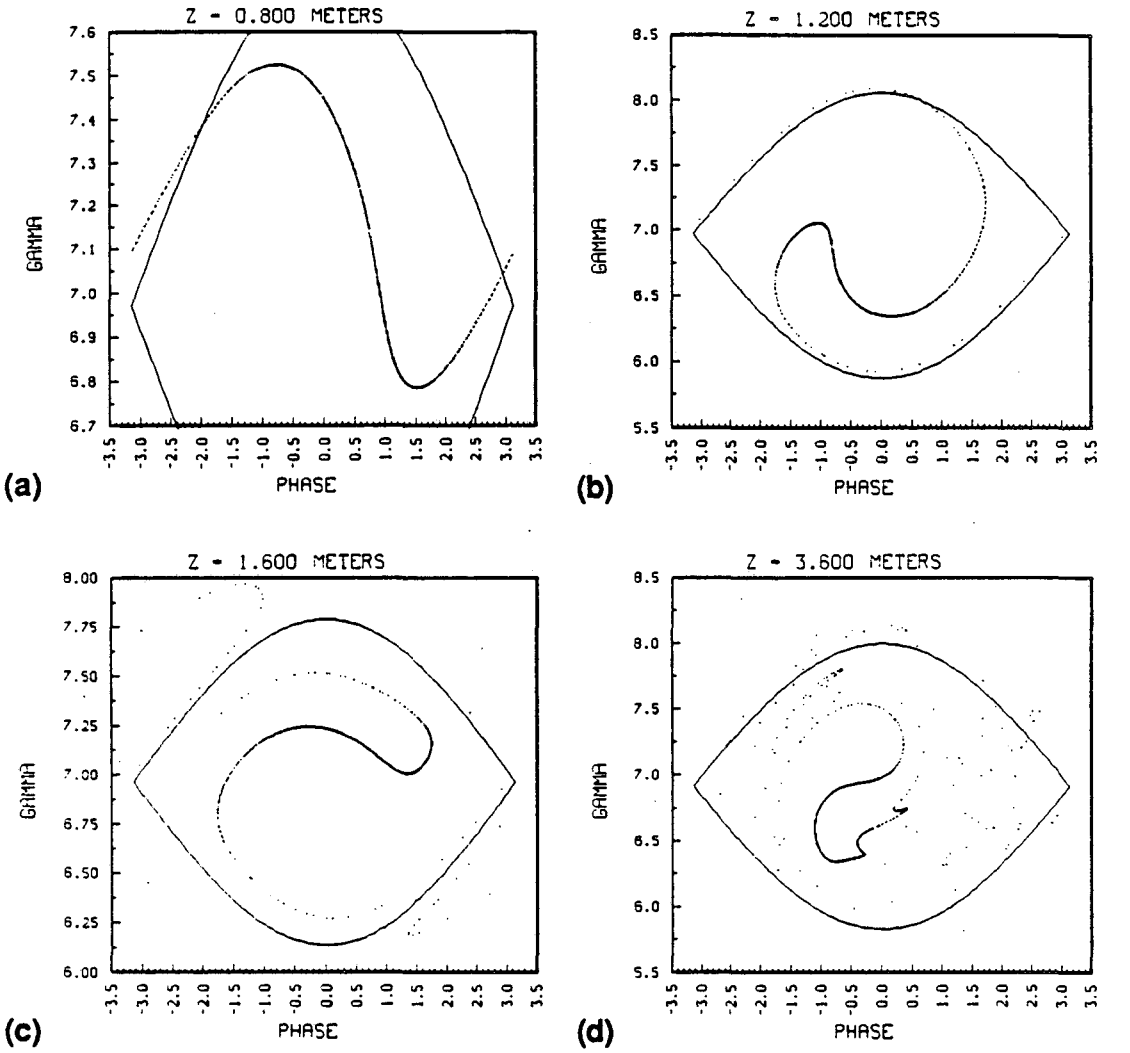

Figure 2.6 Phase space evolution for an FEL with an input electron beam with no initial energy spread.

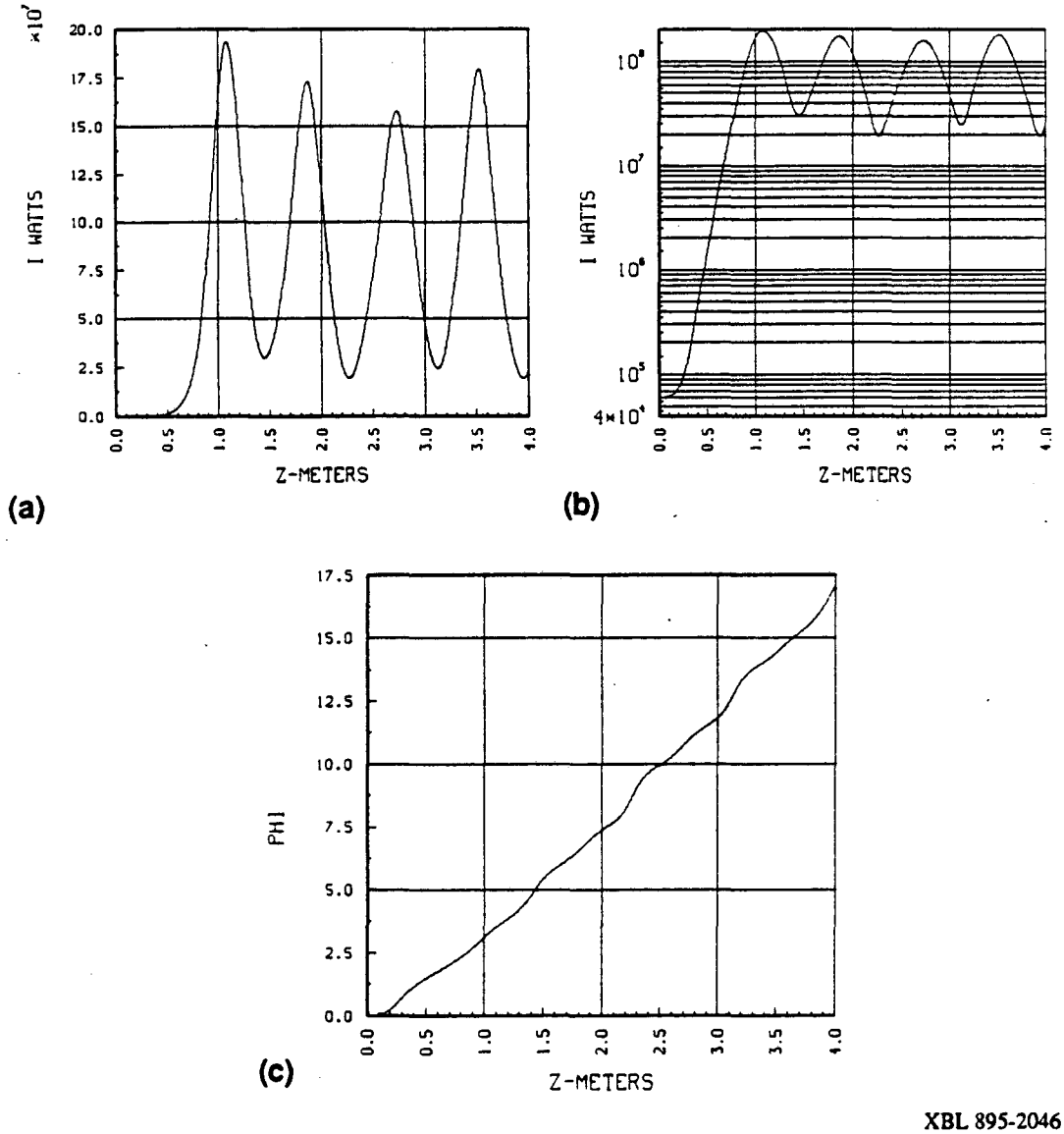

Figure 2.7 Radiation fields for an FEL with an input electron beam with no initial energy spread.

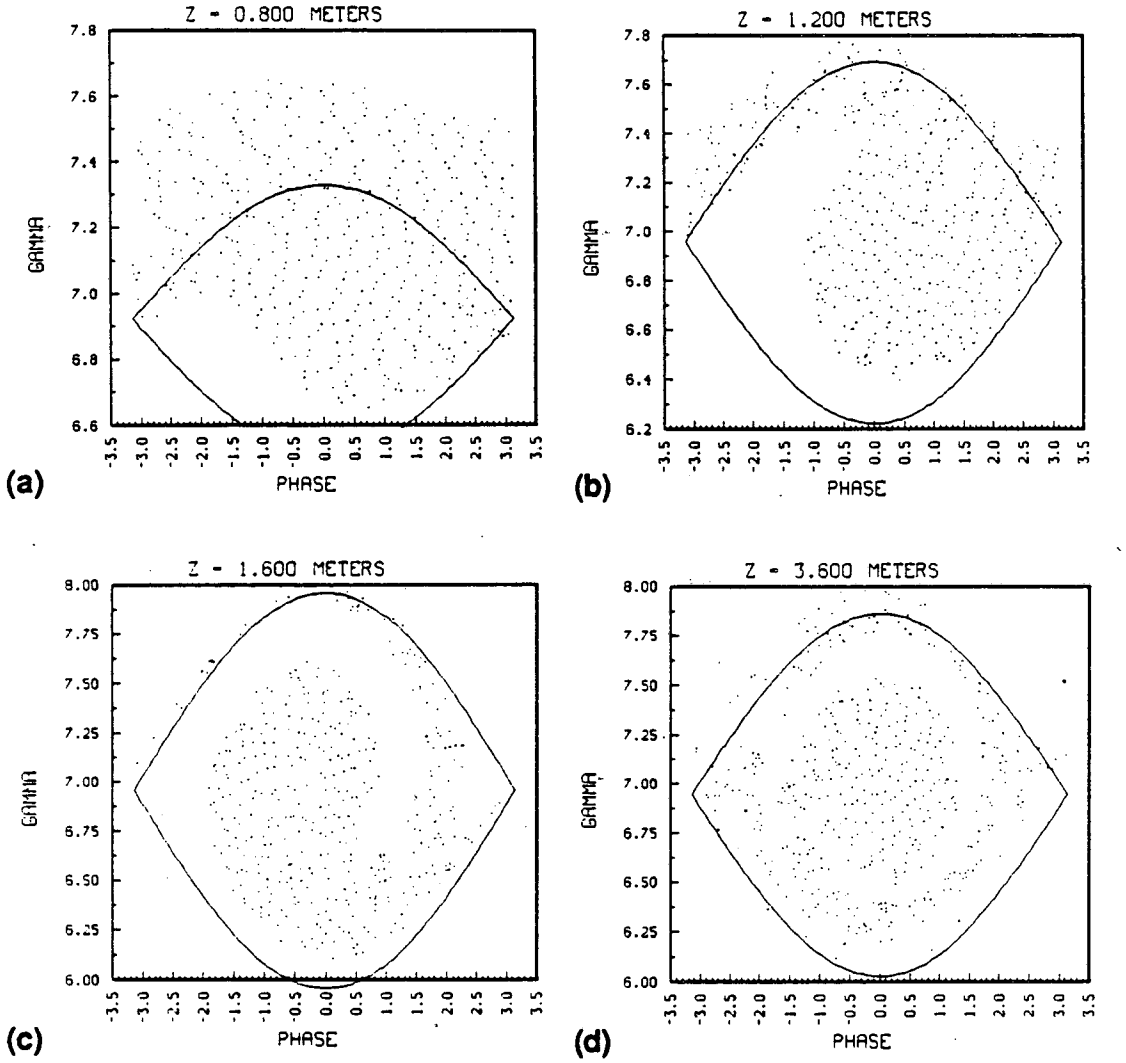

Figure 2.8 Phase evolution for an FEL with an input electron beam with a large energy spread.

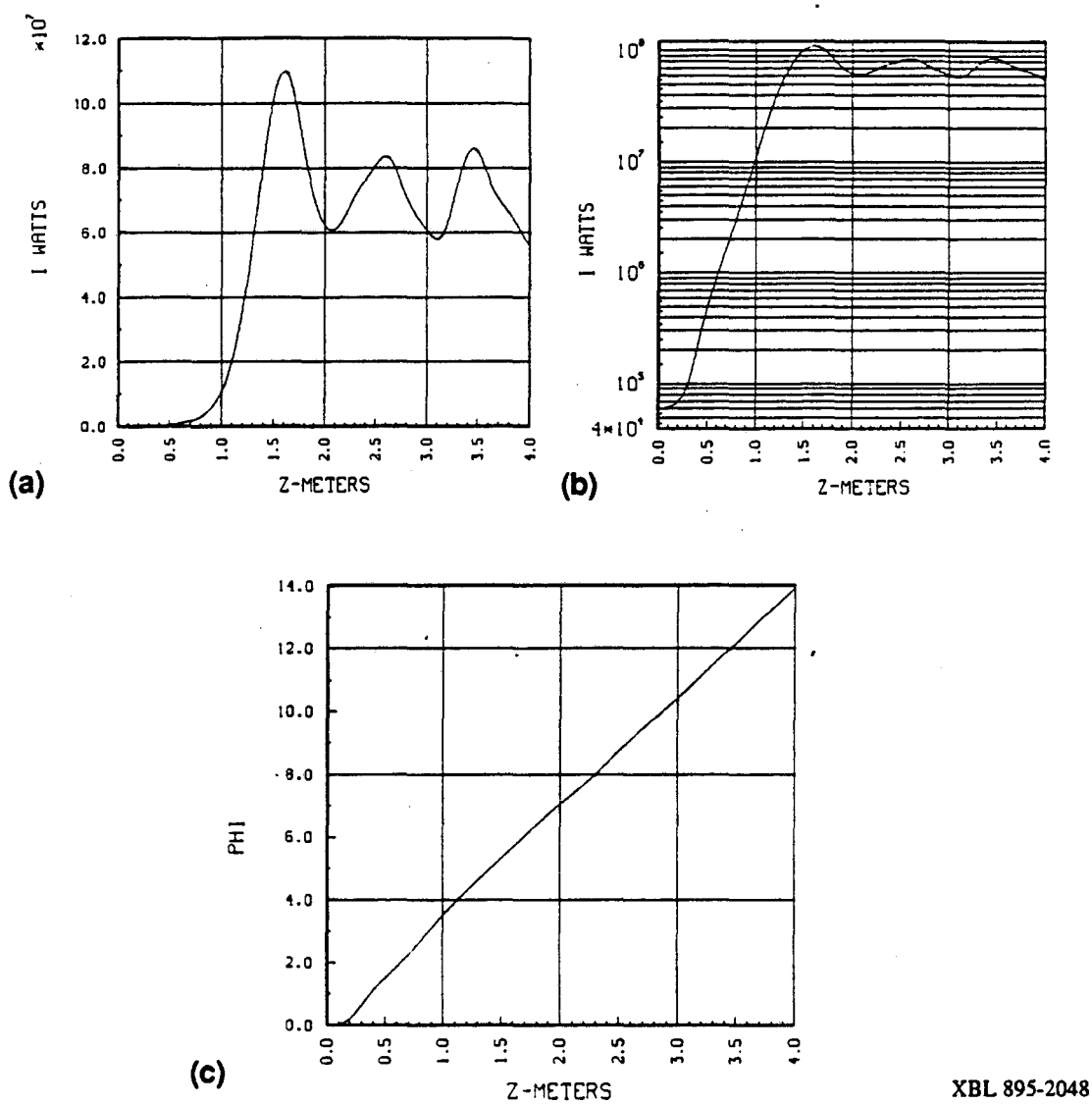

Figure 2.9 Radiation fields for an FEL with an input electron beam with a large energy spread.

space far down the wiggler. Note that in the center of the bucket, the original phase distribution can be seen. By this we mean that the electrons are still more or less distributed along a line. The electrons near the separatrix seem to be scattered about relatively randomly. This is because the neighborhood of the separatrix contains islands due to nonlinear terms and the electron orbits can become rather chaotic there.

In Fig. 2.7 we can see those features relevant to an FEL in the exponential gain regime. In Fig. 2.7b, we see a log plot of the radiation field amplitude versus distance. This confirms that after an initial bunching period, the gain for the radiation field is exponential. The oscillations seen in Figs. 2.7a and 2.7b after saturation are known in the literature as "synchrotron oscillations." The period of these oscillations is given in linear theory by eq. (2.3.7). The other important point to notice is that after the initial bunching period, the slowly varying phase ϕ_s is linear as shown in Fig. 2.7c. It is not only linear in the exponential growth region as one would expect from section 2.5, but its slope is essentially unchanged after saturation.

Now turning to Figs. 2.8 and 2.9, we see the effects of a finite energy spread on FEL evolution. The observations just made for the cold beam case are still generally true with the following differences.

Firstly, the gain has been reduced. The energy spread reduces the coherence of the interaction and therefore the gain must be lower. This also has the effect that the FEL takes longer to saturate. Note in Fig. 2.8 that the electron distribution now fills the bucket relatively uniformly. This has the effect of washing out the synchrotron oscillations as can be seen in Fig. 2.9a. In the case where the beam had no initial energy spread, the electrons form a relatively tight bunch. When these electrons follow their phase space orbits in the bucket, they produce very distinct oscillations in the radiation field. In the case of an initial energy spread, the oscillations are still there, but they are very much reduced.

We now examine the effect of tapering the wiggler after saturation. We use a taper that starts at 1.4 meters (just before saturation), and reduces the peak magnetic field strength to half its initial value by the end of the wiggler at 4 meters. We will start with the parameters with the finite energy spread in order to illustrate the importance of trapping the electrons in the bucket. The results are illustrated in Figs. 2.10 and 2.11.

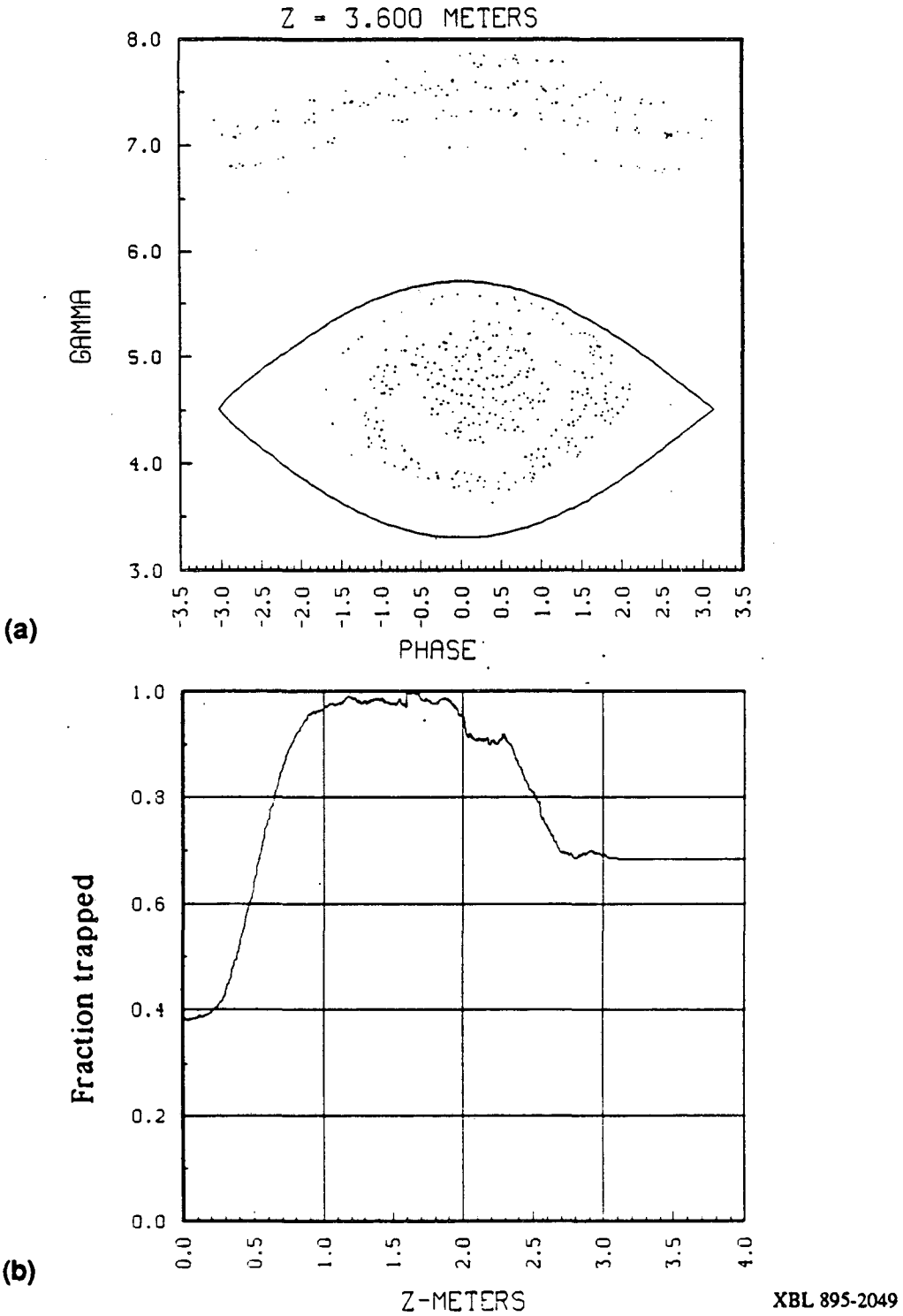

Figure 2.10 (a) shows untrapped and trapped electron populations. (b) shows the fraction of trapped electrons as a function of distance.

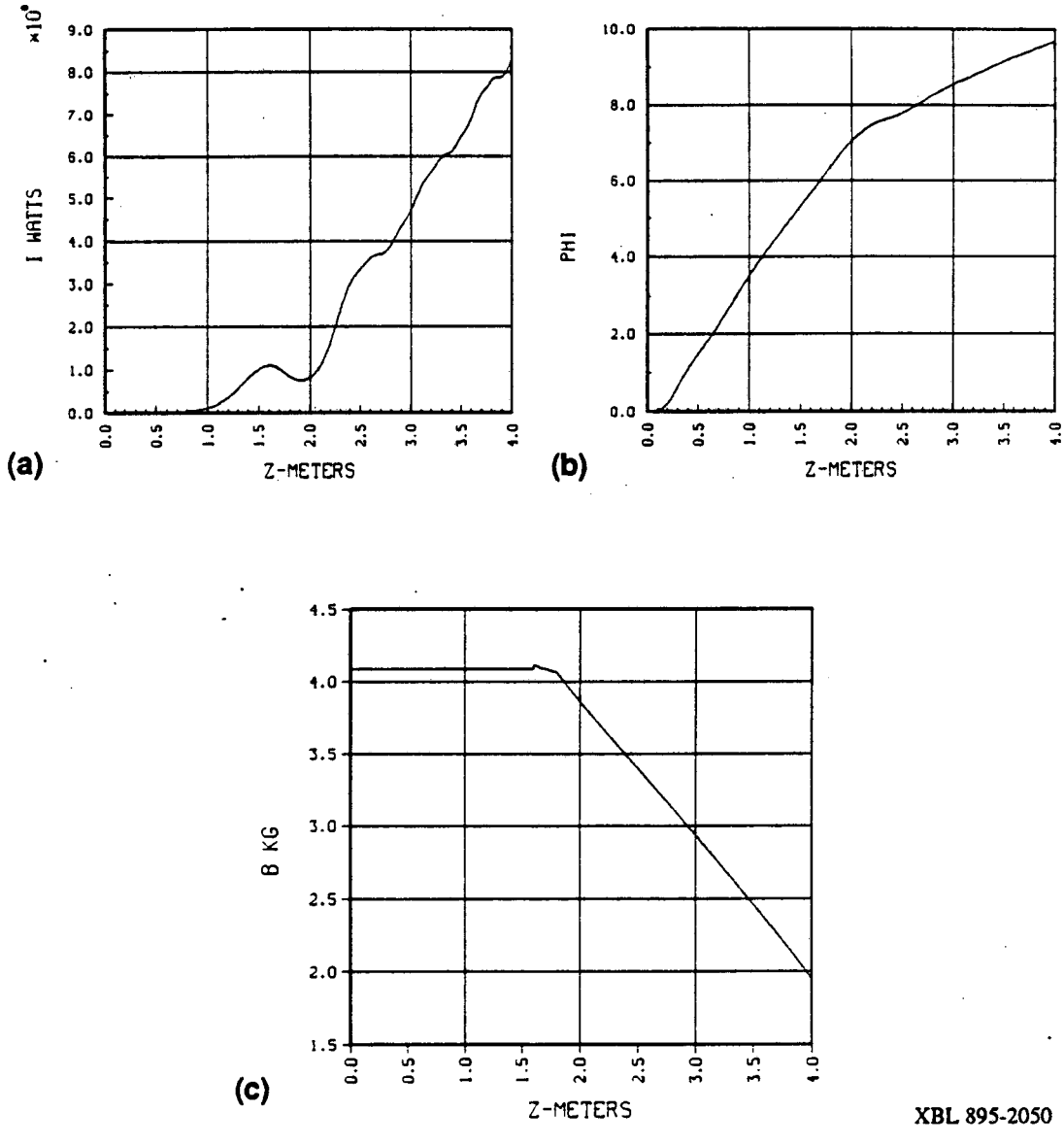

Figure 2.11 Radiation fields for a tapered wiggler. (c) shows the taper of the magnetic field.

In Fig. 2.10a one can see a plot of the phase space near the end of the wiggler. The electrons that were trapped in the bucket were decelerated along with the resonance point. These electrons remain bunched and continue to interact coherently with the radiation field. The electrons that were not trapped were not decelerated, and since the bucket has been moved away from these electrons, they can no longer interact coherently with the radiation. The untrapped electrons smear out and become uniformly distributed in phase. This illustrates the importance of tight bunching for the successful operation of a tapered wiggler FEL.

In Fig. 2.11b, one can see the radiation power as a function of distance. At the end of the wiggler, the FEL has achieved an output power of about 850 MWatts. Compare this to the untapered case where the radiation saturates at about 85 MWatts(fig 2.9a). By doing nothing more than tapering the wiggler field one has achieved a factor of 10 increase in the output power. Similar results have been observed experimentally[20].

The radiation phase in Fig. 2.11c shows a change in slope at the point where tapering begins. This is primarily because of the loss of the untrapped electrons. Since the untrapped electrons no longer interact strongly with the radiation they no longer

contribute to the source term for the radiation. Thus the effective current is less after tapering and the change in the slope of the radiation phase is correspondingly decreased.

2.7 Transverse Effects in FEL's

The physics of an FEL is affected by the fact that the electron beam and the radiation envelope both have a finite cross section. Physical quantities can and usually do vary across this cross section and this can affect FEL performance. For the purposes of the brief discussion of this section we will separate these transverse effects into two general categories. We first discuss those effects due to the finite width of the electron beam. We will then discuss some effects due to the finite width of the radiation envelope.

Perhaps the most important consideration for the electron beam in an actual device is the need for focussing. An electron beam in a vacuum with no focussing will tend to spread out over time. This is because of both space charge and the fact that in any physically realizable beam the electrons will have some small but finite velocity in the transverse direction.

In Fig. 2.12 is an example of a distribution of an electron beam in x-p_x phase space. The standard analysis of beam transport involves modelling the focussing elements as producing linear transformations of the phase space ellipse modelling the beam. The area

of the ellipse divided by π is the standard definition for the beam *emittance*. The larger the emittance is, the more important beam transport is to the physics of an FEL. In principle, since it's the total phase space volume that is a constant by Liouville's theorem, focussing elements can transform phase space area in x-p_x space to z-p_z space or y-p_y space. The particular cross sections of the beam used are chosen mainly for convenience (A good general reference for beam transport is ref. 29).

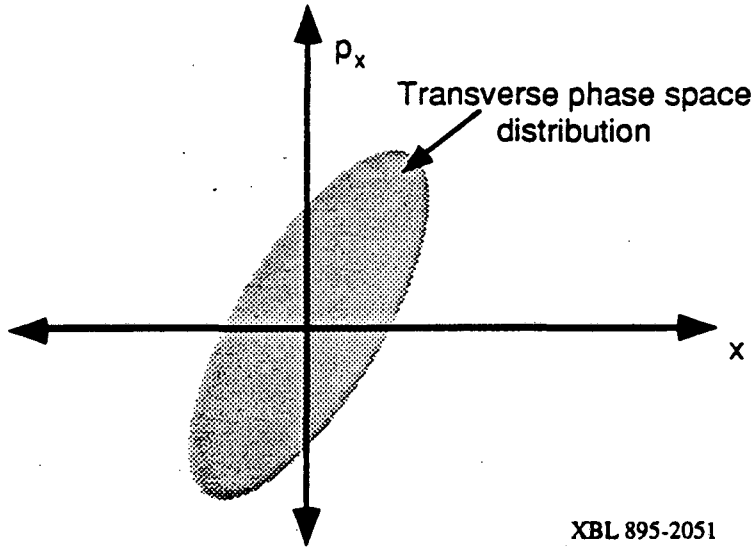

Figure 2.12 Emittance of an electron beam is defined by its area in phase space.

Let us now make some observations concerning beam transport. We need to describe an equilibrium orbit for the beam. This orbit is the path that would be followed by a beam with zero emittance, i.e. an infinitely thin beam with no energy spread. For real

beams with a phase space like Fig. 2.12, there must be a restoring force for those particles in phase space that do not exactly follow the equilibrium orbit, otherwise beams with finite emittances cannot be transported. For small excursion from the equilibrium orbit, the restoring force can be treated as linear. In this case the particles will perform sinusoidal oscillations around the equilibrium orbit. These oscillations are known as *betatron oscillations.*

A real wiggler might have a sinusoidal dependence of the field only along a particular axis. As an example, the so called ideal wiggler field for a linear wiggler is

$$\mathbf{B}_w = |B_w| \left\{ \cosh(k_w y)\cos(k_w z)\hat{y} - \sinh(k_w y)\sin(k_w z)\hat{z} \right\} . \qquad (2.7.1)$$

This is a simple field where the curl and the divergence of the magnetic field are both zero. It is idealized since it can only be realized in a two-dimensional plane. If one sets y=0, then this wiggler field is identical to that used previously for the purely one-dimensional calculations.

Note that the ideal field (2.7.1) increases off axis in the yz plane. This produces focussing in that plane. However, no focussing is provided by this field in the xz plane, so clearly additional focussing is required. For some systems such as the original ELF experiment at Livermore, quadrupole magnets are used to produce the required focussing. However, Ted Scharlemann has noted that if the pole faces of the wiggler magnets are curved in an appropriate manner, such as in Fig. 2.13, then focussing in the xz plane can be achieved without additional focussing elements.

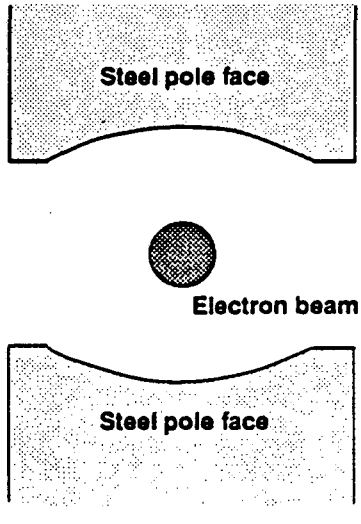

Figure 2.13 "Ted" poles in a wiggler magnet.

The betatron oscillations in an FEL are important for more reasons than just a description of focussing. Back in section 2.3, we defined a resonance energy γ_r by setting $\frac{d\psi}{dz} = 0$. Physically what this corresponds to is setting the parallel velocity of the electron

beam equal to the phase velocity of the ponderomotive potential. If the electrons now also have a finite transverse betatron velocity, then the parallel velocity of electrons with a given energy will be decreased. This will affect the FEL resonance condition. With a finite betatron velocity, an electron with a given energy will have a slower parallel velocity since some of its energy now goes into the betatron oscillation[31].

Different particles with the same energy, γ, can have different betatron oscillation amplitudes. This is because these particles can occupy different parts of the phase space ellipse of Fig. 2.12. This adds an "effective" energy spread to the electron beam. We noted in section 2.4 that a longitudinal energy spread in the electron beam can significantly reduce the FEL gain and saturated amplitude. If a beam has a large emittance, then this too will tend to reduce FEL performance. Thus the production of low emittance beams are vital for high FEL efficiency. Ted Scharlemann has calculated an estimate of the contributions of transverse effects to the apparent energy spread of the electron beam[31]. It is

$$\frac{\delta\gamma_{\parallel}}{\gamma_{\parallel}} = \frac{a_w^2 k_w^2 r_b^2}{4\left(1 + a_w^2\right)} \quad , \tag{2.7.2}$$

where $\gamma_{\parallel}$ is the parallel gamma of the electrons, a_w is the normalized wiggler field amplitude as defined in section 2.2, k_w is the wiggler wave number, and r_b is the electron beam radius. This estimate is valid for a helical wiggler or a linear wiggler with curved pole faces.

Let us now discuss some of the implications when the finite width of the radiation envelope is considered. In a waveguide for instance, there actually isn't a radiation beam "envelope," but the radiation can be described as a sum of transverse modes of the waveguide. These modes vary in intensity over the transverse cross section of the waveguide. Those modes that interact strongly with the electron beam in an FEL have a peak of intensity on axis (assuming the electron beam is sent through the center of the waveguide). This theory is described in detail in the Phd. thesis of Jonathan Wurtele[5].

The propagation of radiation without a waveguide is another matter. If a beam of light is propagating in free space, then diffraction will cause the beam envelope to spread out and the light would eventually become very diffuse. A measure of how fast this happens is the *Rayleigh range* which is given by

$$z_R = \frac{\pi w_0^2}{\lambda} \quad , \tag{2.7.3}$$

where λ is the radiation wavelength, and w_0 is the minimum diameter of the radiation envelope called the *waist*. For very short wavelength FEL's where this Rayleigh range is small compared to the length of the wiggler, one might suppose that the FEL wouldn't work very well since the radiation would diffract away from the electron beam too fast. In fact, in an FEL, the radiation can become "trapped" by the electron beam so that it doesn't diffract away. This phenomenon is call *optical guiding* and is described in detail

elsewhere[32][33][34]. Here we will seek only a general understanding of the phenomenon.

The first type of guiding is called *gain guiding*. This is similar to effects in regular lasers. It occurs when the gain length of the medium is shorter than the Rayleigh range. Physically this corresponds to the radiation being produced faster than it diffracts away so there is a peak of the radiation intensity on axis.

The second type of guiding, and the most interesting from the point of view of FEL physics, is call *refractive guiding*. Even well after saturation, the $\frac{d\phi}{dz}$ equation gives a nonzero value for the slowing of the radiation phase. From the simulations shown in section 2.4, one can see that the value of $\frac{d\phi}{dz}$ is essentially unchanged throughout the operating distance of the FEL. Physically this slowing of the radiation wavefront can be said to correspond to an index of refraction n. For a linear medium, the phase velocity is related to the index of refraction by $v_{phase} = \frac{c}{n}$. If this is the case, then the index of refraction in an FEL can be written

$$n = 1 + \frac{c}{\omega}\frac{d\phi_s}{dz} \quad , \tag{2.7.4}$$

where $\frac{d\phi_s}{dz}$, given by (2.2.18d), is the equation for the slowly varying phase in an FEL. One can see that if this description is accurate, then the index of refraction in the center of the FEL beam will be greater than 1.

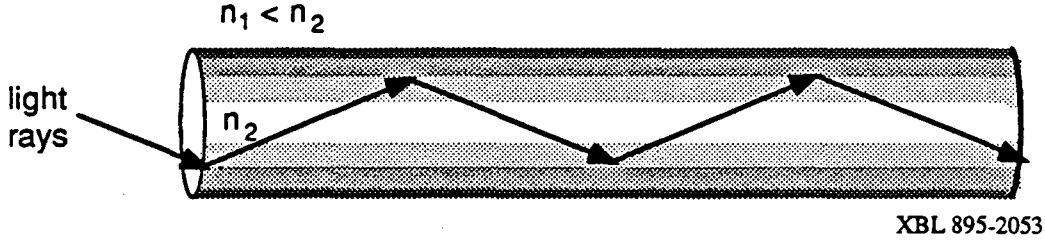

Figure 2.14 Radiation guiding in an optical fiber. Radiation strikes the fiber cladding at less than the angle required for total internal reflection.

To see how this property can lead to guiding, let's examine the analogous case of an optical fiber. In an optical fiber the index of refraction of the fiber, usually some type of glass, is higher than that of the air around it. One can imagine that if the fiber was thin enough, then the light rays traveling in the fiber will always strike the surface of the fiber at less than Brewster's angle, which is the condition for total internal reflection. This is a somewhat oversimplified picture, but it conveys the general physics. In general, in order to guide light, the fiber or dielectric waveguide must have a higher index of refraction on axis than off axis. In his book *Quantum Electronics* [30], Yariv demonstrates guiding for a dielectric medium where the index of refraction falls off quadratically from the axis.

Since the $\frac{d\phi_s}{dz}$ term in the index of refraction is directly proportional to the current density, this in some ways might be a better model since simulations have shown that a quadratic fit to the current density distribution is a good description.

One other note is for those that feel uncomfortable with the notion of a plasma, the electron beam, guiding radiation. Those who work with plasmas know that they have the opposite effect of guiding on radiation, at least as long as only linear susceptibilities are concerned. However, in those situations, one usually deals with a fairly uniform plasma. In an FEL, one has a case where the plasma has density modulations on the same length scale as the radiation wavelength. This is then an entirely different regime than ordinary plasma calculations. Also if one calculates nonlinear susceptibilities, one can create a situation where the index of refraction at the center of the radiation beam is higher than at the edges. This can result from ponderomotive forces or from the relativistic increase in mass of the electrons. While these effects in a uniform plasma are different from the FEL interaction, an FEL is a highly nonlinear optical medium and one should not be surprised that linear optics theory is no longer valid.

2.8 2-D FEL Simulations

Here we will present some results of 2-D numerical simulations of FEL's. The simulations in this section were performed by the FRED code developed by Bill Fawley and Ted Scharlemann at the Lawrence Livermore National Laboratory. This code has been described in great detail elsewhere[35][36][37], so here we give a brief description.

The FRED code follows the electron motion in a single FEL bucket. Included are the effects of transverse motion such as betatron oscillations. The field solver solves the paraxial wave equation(second derivatives in the wave equation are ignored). This field solver is for two dimensions. For the cases here, the second dimension is the radial coordinate.

The cases here illustrate the effect of optical guiding. Figure 2.16 shows an isometric plot of the radiation intensity. It show that even well after saturation, the radiation is trapped by the electron beam. The remainder of the plots demonstrate the importance of guiding to FEL operation. Using the parameters in Table II, two computer runs were performed using the FRED simulation code. In one of the runs, optical

guiding was turned off. A direct comparison of the output in Fig. 2.16 shows that without optical guiding, FEL performance seriously deteriorates(note that the power plot has a log scale). Figs. 2.17 - 2.20 show profiles of radiation power and radiation phase with and without optical guiding. A comparison of the power profiles (Fig. 2.17 and 2.19) demonstrates that without optical guiding, the radiation rapidly diffracts away from the axis of the beam. Also, the beam with optical guiding is closer to a diffraction limited beam as indicated by the fact that the phase profile is closer to a spherical fit (Fig. 2.18 and 2.20).

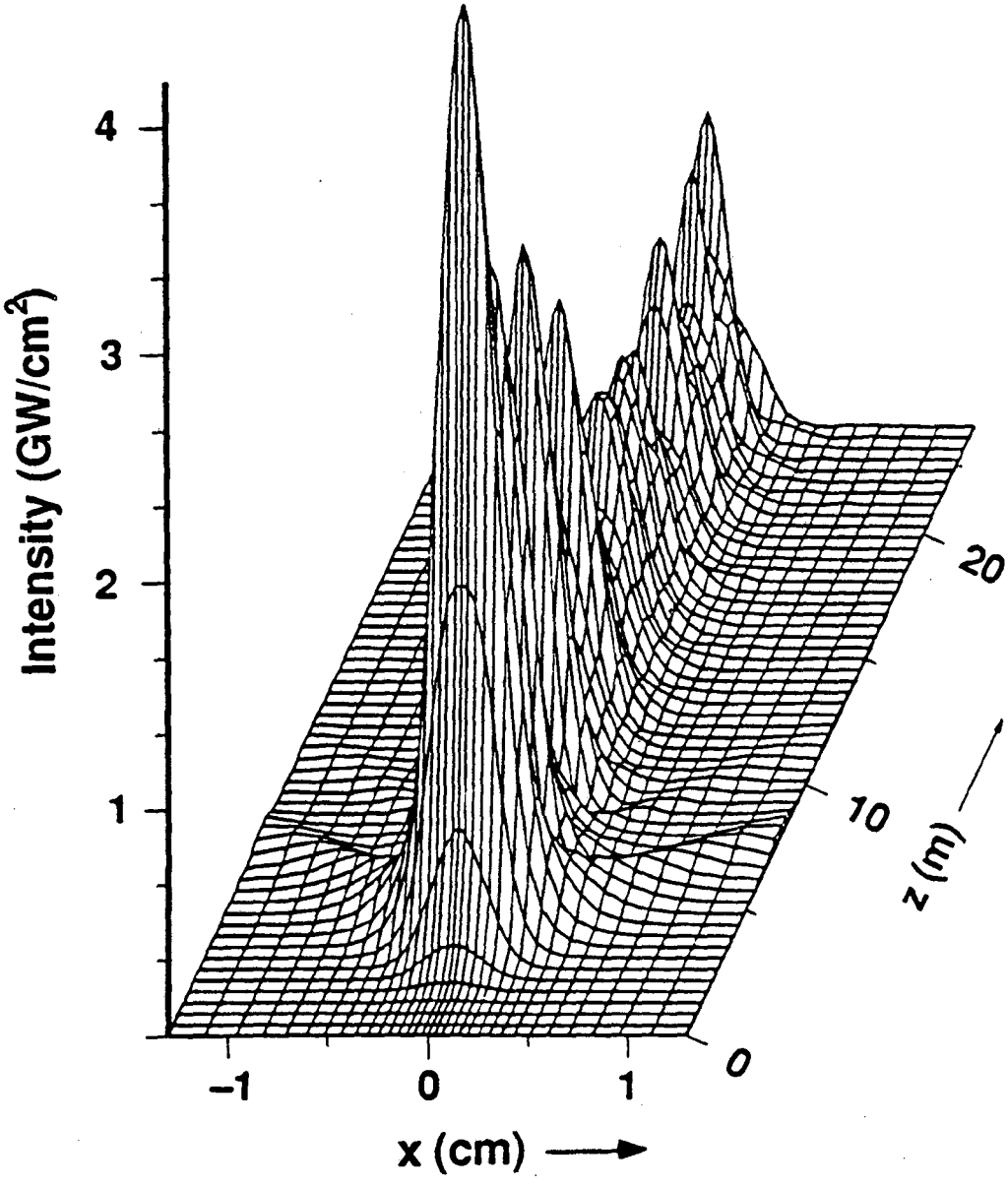

Figure 2.15 (ref. 32) Radiation intensity profile demonstrates that the radiation is trapped long after saturation(reproduced by permission).

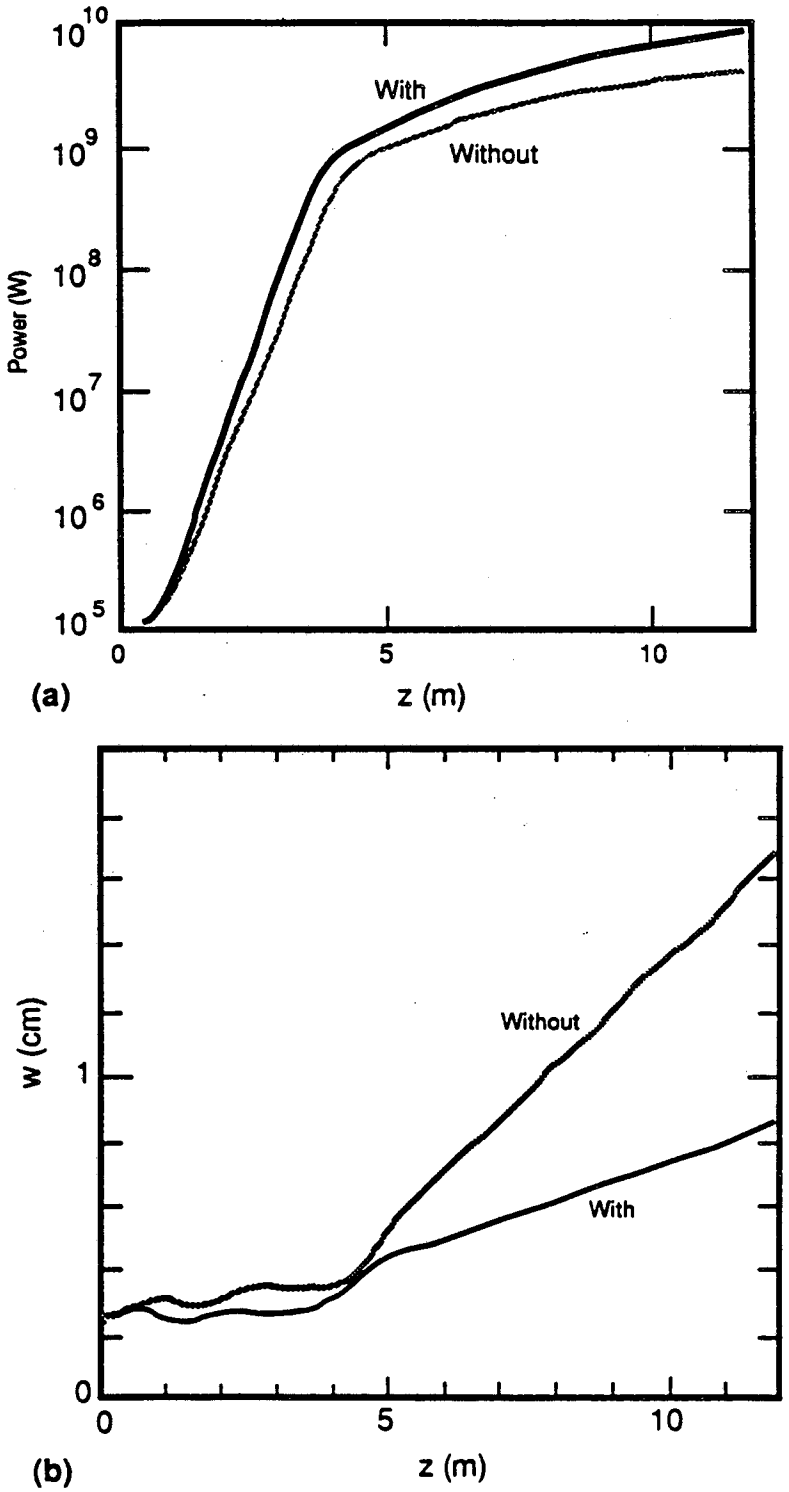

Figure 2.16 (ref. 32) Power(a) and spot size(b) vs. wiggler length for the 21 μm amplifier with and without optical guiding(reproduced by permission).

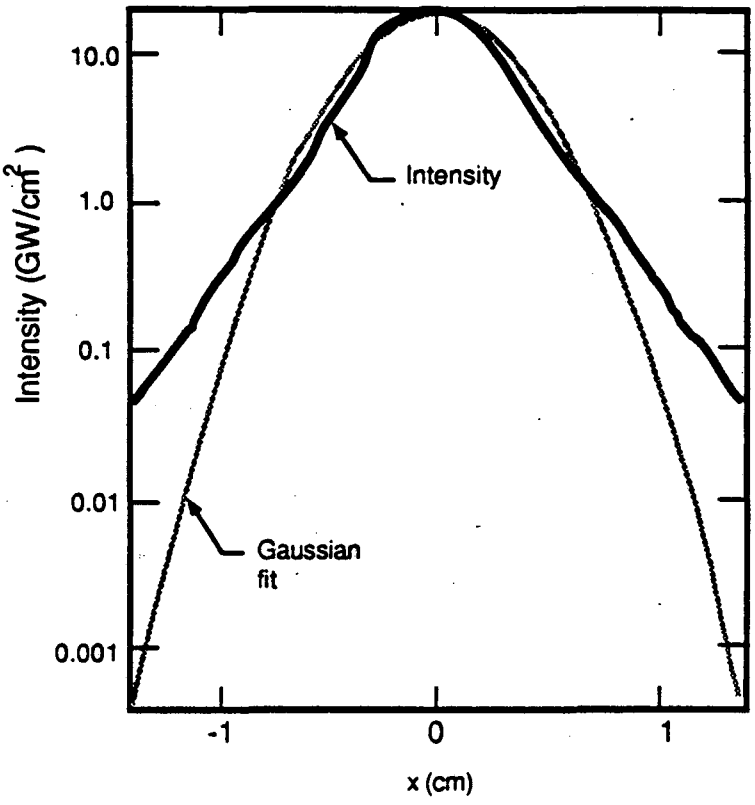

Figure 2.17 (ref. 32) Output intensity profile of the 21 μm amplifier(reproduced by permission).

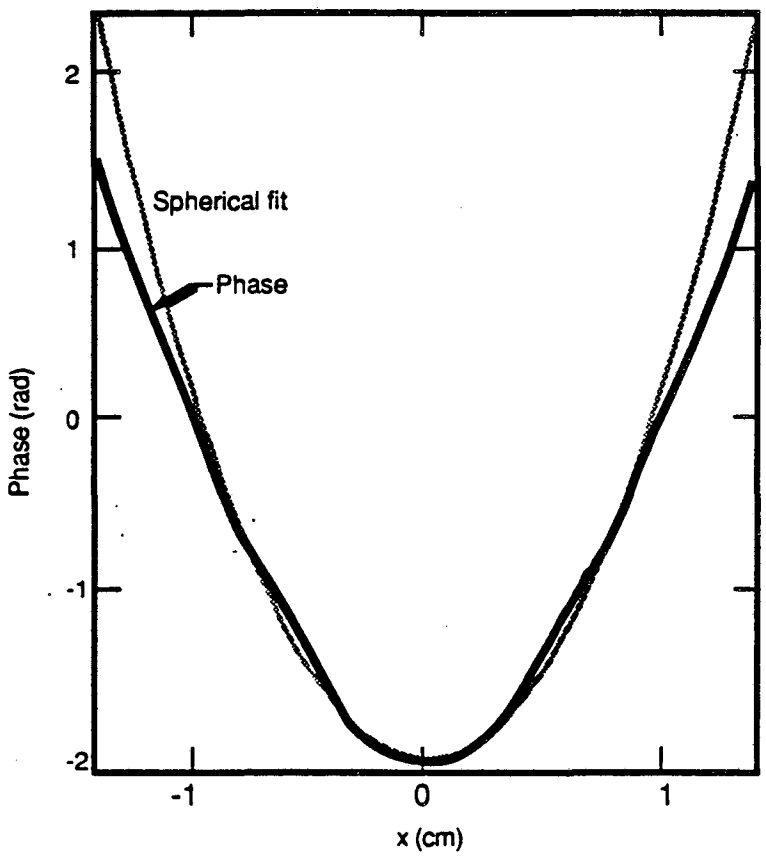

Figure 2.18 (ref. 32) Output phase profile of the 21 μm amplifier(reproduced by permission).

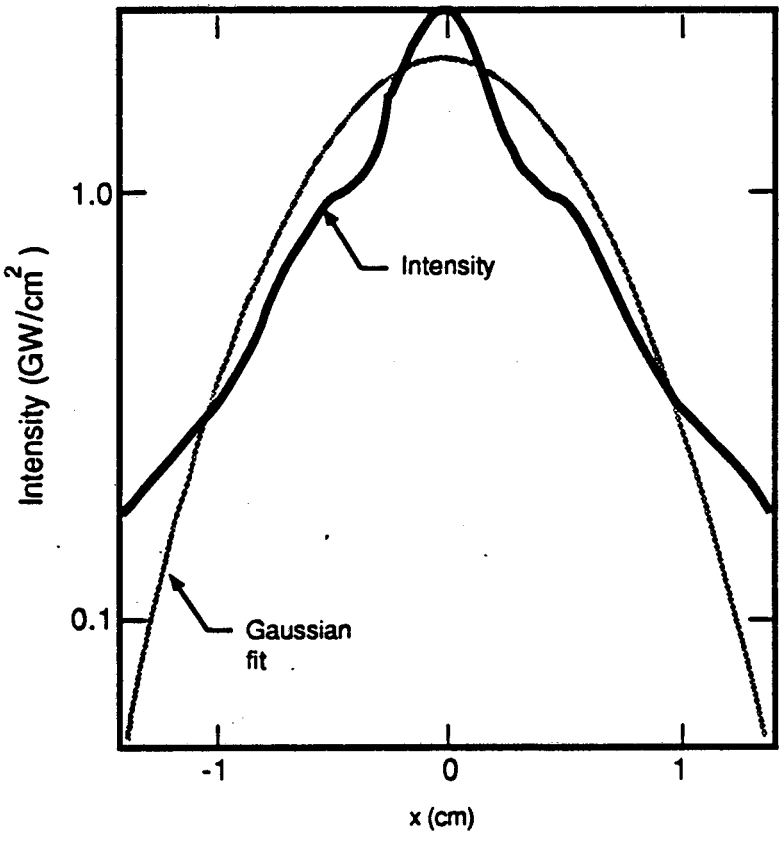

Figure 2.18 (ref. 32) Output intensity profile of the 21 μm amplifier when optical guiding is removed(reproduced by permission).

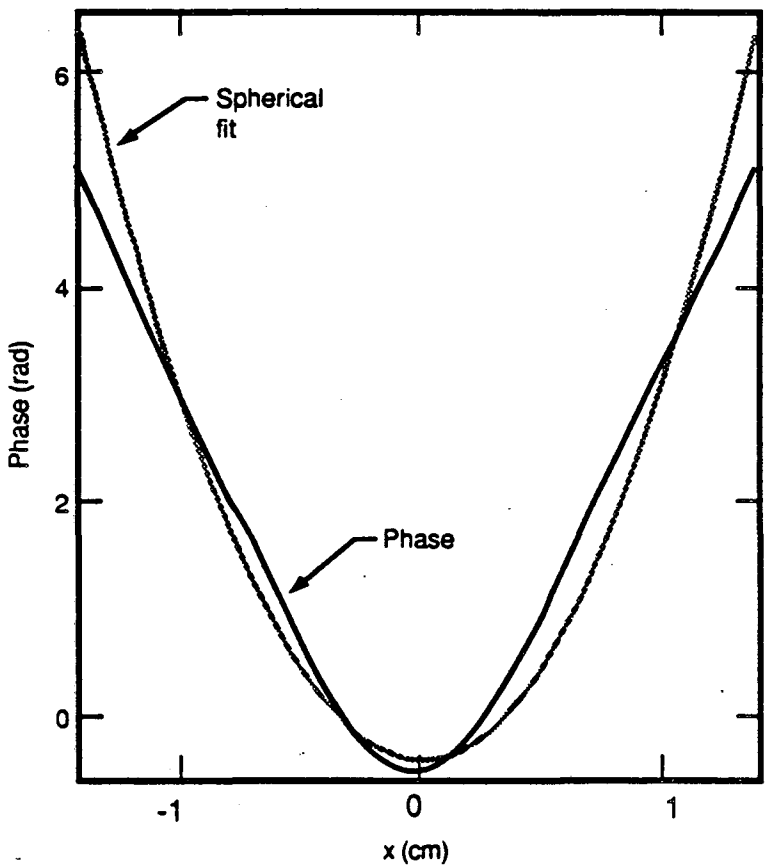

Figure 2.20 (ref. 32) Output phase profile of the 21 mm amplifier when refractive guiding is removed(reproduced by permission).

Table II

Beam energy	38	Mev
Current	1	kA
Emittance (normalized)	0.1	rad-cm
Wavelength	21	μm
Input power	100	kW
Input spot radius	0.25	cm
Wiggler period	5.5	cm
Wiggler length	1200	cm
Initial magnetic field	4.93	KG

Chapter 3

Formalism for Multiple Frequencies in a Waveguide FEL

3.1 FEL's in Dispersive Media

In this chapter we will develop a formalism for dealing with FEL's in dispersive media. This formalism will be capable of describing FEL evolution for an arbitrary number of frequencies. What makes this approach different from previous calculations is the inclusion of all the effects of dispersion on FEL evolution.

In a waveguide, the evolution of the FEL radiation field can be quite complicated due to the effects of dispersion. Calculations of the frequency output of waveguide FEL's can be rather tedious if the field evolution is described by differential equations. A separate set of equations would be needed for each frequency and in addition, each frequency must be associated with a different ponderomotive well, which in a highly dispersive waveguide move at very different speeds. Another complication is that in a waveguide, group velocity and phase velocity are quite different quantities.

In response to these concerns I have derived an integral formulation for the field evolution in a waveguide FEL[22][27]. This formulation is quite general. The only

assumption made is that the field can be decomposed into a relatively small number of transverse modes.

From this integral formulation it is also possible to derive a set of differential equations suitable for integration on a computer, which doesn't mind if a calculation in tedious. The reason that this is desirable is that computer integration packages generally require a set of coupled differential equations as input.

The last section of this chapter demonstrates that the differential equations derived can, under certain approximations, be reduced to a set of differential equations identical to the KMR equations for an FEL in a waveguide.

3.2 Derivation of the Waveguide Green's Function

In this section, a Green's function will be derived for a linear wiggler FEL in a rectangular waveguide. The derivation is easily generalized to include helical wigglers and waveguides of arbitrary geometry. The only requirement is that the radiation field must be such that it can be expanded in transverse modes.

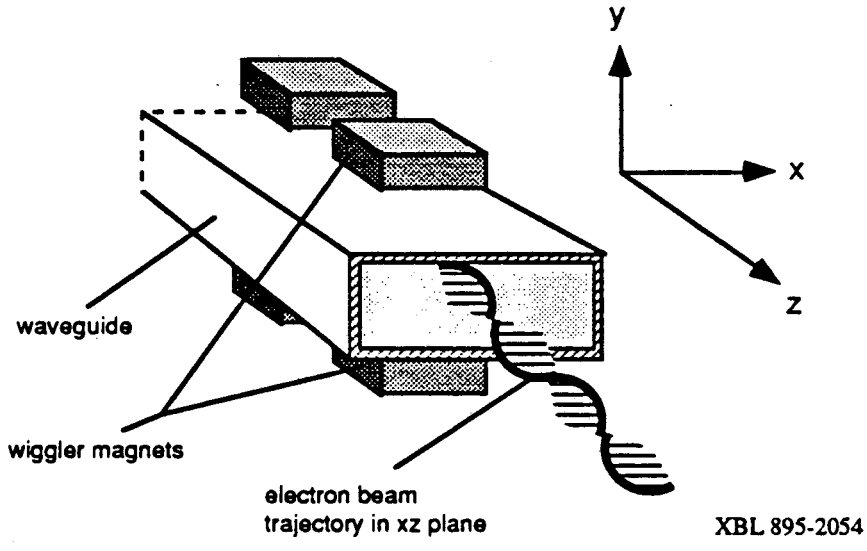

Figure 3.1 Linear Wiggler FEL in a rectangular waveguide.

The geometry of the particular FEL configuration used is shown in Fig. 3.1. Since the wiggler field is in the y direction, the electron trajectories will remain in the xz plane. The radiation field evolution is described by

$$\left[\nabla_t^2 + \frac{\partial^2}{\partial z^2} - \frac{\partial^2}{c^2 \partial t^2}\right] A_x(x,t) = \frac{-4\pi}{c} J_x(x,t) \quad , \tag{3.2.1}$$

where $A_x(x,t)$ is in radiation gauge, and ∇_t^2 is the transverse Laplacian.

At this point it is worth saying a few words about the choice of gauge. For this calculation we use *radiation gauge*, sometimes called *transverse gauge*. In this gauge, the equations for the electric and magnetic potentials are

$$\left[\nabla^2 - \frac{\partial^2}{c^2 \partial t^2}\right] A(x,t) = \frac{-4\pi}{c} J_t(x,t) \quad , \tag{3.2.2a}$$

$$\text{and} \qquad \frac{1}{c} \nabla \frac{\partial \Phi(x,t)}{\partial t} = \frac{4\pi}{c} J_l(x,t) \quad , \tag{3.2.2b}$$

$$\text{where } \nabla \cdot J_t = 0, \tag{3.2.2c}$$

$$\text{and } \nabla \times J_l = 0, \tag{3.2.2d}$$

where J_t is called the transverse current and J_l is called the longitudinal current. It is always possible to separate the current in this manner as indicated by Helmholtz' theorem. This separates out those components of the current that actually radiate[23]. Here we are

primarily interested in creating a 1-D formalism(i.e. deriving equations that depend only on z and t). If we ignore the thickness of the electron beam, then $\mathbf{J}(x,t) \equiv \mathbf{J}(z,t)$. If this is true then J_z does not contribute to the radiation source term even for a TM mode where $E_z \neq 0$.This can be seen from eqs. (3.2.2a) and (3.2.2c). J_z only contributes to the longitudinal current. Thus, to calculate the radiation fields we need only concern ourselves with the transverse component of the current, which is J_x in our example(although the radiation E_z can act on J_z and thus affect the FEL evolution).

We now wish to expand the radiation fields in transverse modes. For the current discussion we set $A_y = 0$, since for the geometry we have chosen $J_{ty} = 0$. It is simple in principle to expand in the most general waveguide modes for an arbitrary geometry, but the algebra can become quite tedious.

We make a particular expansion in transverse modes:

$$A_x(x,t) = \sum_{m,n \neq 0}^{\infty} A_x^{mn}(z,t) \cos\frac{m\pi x}{a} \sin\frac{n\pi y}{b} \quad . \tag{3.2.3}$$

Here the form of A_x is the same for TE and TM modes. For a TM mode, there is also an

A_z component, but from the argument just made over eqns (3.2.2), we need not follow A_z for radiation field evolution. In fact, if we have the transverse components of A at any point, the longitudinal component is uniquely determined. To see this, remember the justification for separating waveguide modes into TE and TM modes. If both E_z and B_z are known, then Maxwell's equations and the boundary conditions determine all the field components. The separation into TE and TM modes allows one to solve a single equation for all the radiation components. For the case here, it is simply more convenient to go in the other direction and calculate the transverse components first[4].

This expansion reduces the wave equation to one space and one time dimension.

$$\left[\gamma_t^2 - \frac{\partial^2}{\partial z^2} + \frac{\partial^2}{c^2 \partial t^2}\right] A_x^{mn}(z,t) = \frac{2}{c} J_x^{mn}(z,t) \quad , \tag{3.2.4}$$

where

$$\gamma_t^2 = \frac{m^2\pi^2}{a^2} + \frac{n^2\pi^2}{b^2} \quad , \tag{3.2.5}$$

$$J_x^{mn}(z,t) = \frac{8\pi}{ab(1+\delta_{m0})} \int_0^a dx \int_0^b dy \cos\frac{m\pi x}{a} \sin\frac{n\pi y}{b} J_x(x,t) \quad . \tag{3.2.6}$$

At this point it is worth noting that if we had started with a different geometry (a circular waveguide for instance), the form of eq. (3.2.6) would be identical. The terms γ_t

and J_x^{mn} contain all the information relating to the transverse geometry. Thus the derivation from this point on is quite general.

We now make the following substitutions:

$$A_x^{mn}(z,t) = \int_{-\infty}^{+\infty} \frac{dk}{\sqrt{2\pi}} \tilde{A}_x^{mn}(k,t)\, e^{ikz} \quad , \tag{3.2.7a}$$

$$J_x^{mn}(z,t) = \int_{-\infty}^{+\infty} \frac{dk}{\sqrt{2\pi}} \tilde{J}_x^{mn}(k,t)\, e^{ikz} \quad . \tag{3.2.7b}$$

This leads to

$$\frac{\partial^2}{\partial t^2} \tilde{A}_x^{mn}(k,t) + c^2 \left(\gamma_t^2 + k^2\right) \tilde{A}_x^{mn}(k,t) = 2c\tilde{J}_x^{mn}(k,t) \quad , \tag{3.2.8}$$

which is the inhomogeneous Helmholtz equation for a dispersive medium in one dimension.

The homogeneous solution to this equation just corresponds to modes propagating in a current-free waveguide[4]. The inhomogeneous solution is where the FEL physics is contained. This equation has the form of a forced harmonic oscillator. The solutions to this type of equation are well known[24]. The initial conditions of the particular solution we are seeking are given by requiring that causality be maintained. We also require that the solution be everywhere continuous and smooth. Specifically, if $\tilde{J}_x^{mn}(k,t) = 0$ for $t < 0$,

then we require[25]

$$\tilde{A}_x^{mn}(k,t=0) = \frac{\partial}{\partial t}\tilde{A}_x^{mn}(k,t=0) = 0 \quad .$$

Given these conditions, the solution of equation (3.2.8) can be written

$$\tilde{A}_x^{mn}(k,t) = 2\int_0^t dt'\, \tilde{J}_x^{mn}(k,t')\,\frac{\sin c\sqrt{\gamma_t^2 + k^2}\,(t-t')}{\sqrt{\gamma_t^2 + k^2}} \quad . \tag{3.2.9}$$

If we now use the inverse transform of (3.2.7b), and substitute (3.2.9) into (3.2.7a), we can write

$$A_x^{mn}(z,t) = \int_0^t dt' \int_{-\infty}^{+\infty} dz'\, J_x^{mn}(z',t')\, G(z-z', t-t') \quad , \tag{3.2.10}$$

where[26]

$$G(z-z',t-t') = \frac{1}{\pi}\int_{-\infty}^{+\infty} dk\, e^{ik(z-z')}\,\frac{\sin\left[c\sqrt{\gamma_t^2 + k^2}\,(t-t')\right]}{\sqrt{\gamma_t^2 + k^2}} \quad , \tag{3.2.11a}$$

$$= J_0\left\{\gamma_t\sqrt{c^2(t-t')^2 - (z-z')^2}\right\}\theta[\,c|t-t'| - |z-z'|\,] \quad , \tag{3.2.11b}$$

where J_0 is the zero order Bessel function, and θ is the step function which is equal to 1 for arguments greater than zero and is equal to zero for arguments less than zero.

3.3 Derivation of Differential Equation Form

The integral formulation derived in the previous section is useful in that it provides a single integral equation for the radiation field evolution of a particular transverse mode. The effects due to waveguide dispersion are automatically included. However, it we wish to perform numerical calculations on a computer, most numerical integration packages require a set of differential equations as input. In this section we reduce the integral equation (3.2.10) to a set of differential equations suitable for following many frequencies in an FEL.

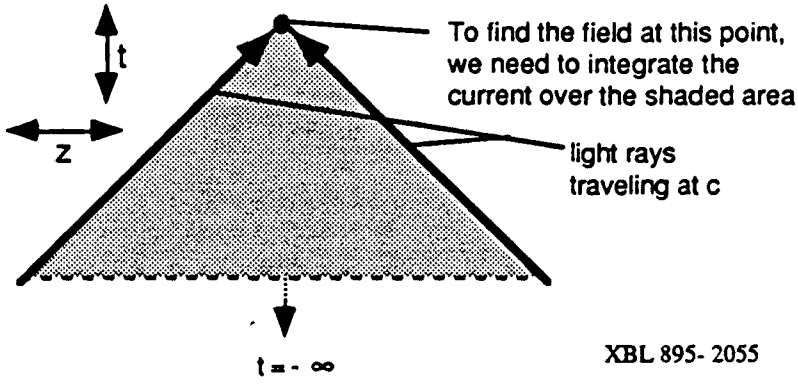

Figure 3.2 Domain of integration for integral equation.

To calculate $A_x^{mn}(z,t)$ at a point (z,t), one needs to integrate over the region indicated in Fig 3.2. To facilitate this integration, we first perform a change of variables as follows.

$$\tau = c\,(t - t') \quad , \qquad \eta = z - z' \quad ,$$

$$d\tau = -c\,dt' \quad , \qquad d\eta = -dz' \quad .$$

After this substitution and an exchange in the order of integration, eq. (3.2.10) becomes

$$A_x^{mn}(z,t) = \frac{1}{c}\int_{-\infty}^{+\infty} d\eta \int_{\eta}^{+\infty} d\tau\, J_x^{mn}(\eta, \tau, z, t)\, J_0\left\{\gamma_t\sqrt{\tau^2 - \eta^2}\right\} \quad . \tag{3.3.1}$$

Since we need a finite number of equations for our computer integration we will expand $J_x^{mn}(z',t')$ as a sum of components at different frequencies. This corresponds to a discrete fourier transform or if the system is periodic it corresponds to a fourier series. This expansion can be written

$$J_x^{mn}(z',t') = \sum_j \left(C_j^{mn}(z')\cos\omega_j t' + B_j^{mn}(z')\sin\omega_j t'\right) \quad . \tag{3.3.2}$$

Transforming to the variables η and τ, and substituting into (3.2.1) gives

$$A_x^{mn}(z,t) = \sum_j \frac{1}{c}\int_0^{\infty} d\eta \int_{\eta}^{\infty} d\tau J_0\left\{\gamma_t\sqrt{\tau^2 - \eta^2}\right\}\left[\alpha_j^{mn}(z',t)\cos\omega_j\frac{\tau}{c} + \beta_j^{mn}(z',t)\sin\omega_j\frac{\tau}{c}\right] \quad , \tag{3.3.3}$$

where

$$\alpha_j^{mn}(z',t) = C_j^{mn}(z') \cos \omega_j t + B_j^{mn}(z') \sin \omega_j t \quad , \tag{3.3.4a}$$

$$\beta_j^{mn}(z',t) = C_j^{mn}(z') \cos \omega_j t - B_j^{mn}(z') \sin \omega_j t \quad . \tag{3.3.4b}$$

If we wish to perform the integration over τ, we have two integrals to do. The integral containing the cosine term will give a nonzero answer only if ω_j is below cutoff in the waveguide. We can ignore this term because in an FEL, only those waves that propagate down the waveguide are of interest. Performing the integration over the sin term gives

$$\int_{\eta}^{\infty} d\tau J_0\left\{\gamma_t\sqrt{\tau^2 - \eta^2}\right\} \sin\frac{\omega_j\tau}{c} = \begin{cases} 0 & \text{for } 0 < \frac{\omega_j}{c} < \gamma_t \\ \frac{\cos k_{sj}\eta}{k_{sj}} & \text{for } \gamma_t < \frac{\omega_j}{c} < \infty \end{cases} \quad , \tag{3.3.5}$$

where $k_{sj} = \sqrt{\frac{\omega_j^2}{c^2} - \gamma_t^2}$. If we now substitute (3.3.5) into (3.3.3) and express the answer in terms of the original variables we obtain

$$A_x^{mn}(z,t) = \frac{1}{c}\sum_j \frac{1}{k_{sj}}\int_{-\infty}^{z} dz' \left[B_j^{mn}(z') \cos\omega_j t' - C_j^{mn}(z') \sin\omega_j t'\right] \cos(k_{sj}(z - z')) \quad . \tag{3.3.6}$$

In a 1-D computer simulation of an FEL , one usually follows the evolution of the radiation as it travels along the wiggler. In a normal FEL only forward traveling waves are interesting. We can then restrict the integration over z' as follows:

$$\int_{-\infty}^{+\infty} dz' \longrightarrow \int_{-\infty}^{z} dz' \ .$$

This is illustrated graphically in Fig. 3.3. The integration only needs to include the left side of the integration region since forward traveling waves emitted in the right side of the integration region can't communicate with the point of interest.

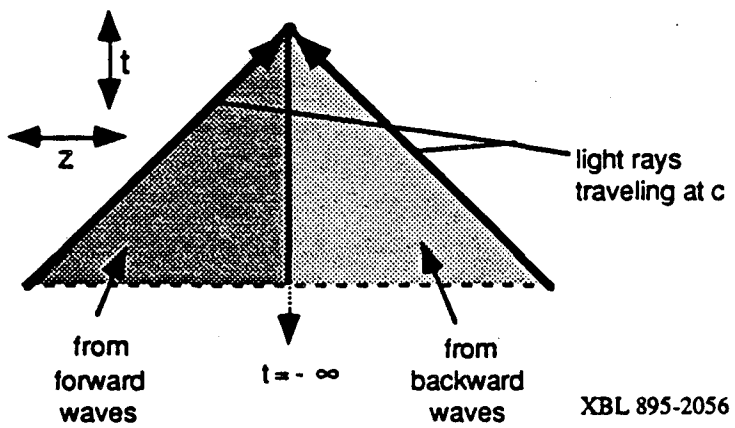

Figure 3.3 Integration region for forward and backward traveling waves.

To derive the differential equation form we integrate (3.3.6) over an infinitesimal distance δ, and calculate the change in A_x^{mn}.

$$\delta A_x^{mn}(z,t) = \frac{1}{c}\sum_j \frac{1}{k_{sj}}\int_z^{z+\delta} dz' \left[B_j^{mn}(z')\cos\omega_j t' - C_j^{mn}(z')\sin\omega_j t'\right]\cos(k_{sj}(z - z'))$$

$$= \frac{1}{c}\sum_j \frac{1}{k_{sj}}\left[B_j^{mn}(z)\cos\omega_j t - C_j^{mn}(z)\sin\omega_j t\right]\delta \qquad (3.3.7)$$

Going back briefly to (3.3.2), we see that J_x^{mn} could have been written

$$J_x^{mn}(z,t) = \sum_j J_{0j}^{mn}(z)\cos\left(\Phi_{Jj}(z) - \omega_j t\right) = \sum_j J_{0j}^{mn}(z)\left[\cos\Phi_{Jj}(z)\cos\omega_j t + \sin\Phi_{Jj}(z)\sin\omega_j t\right] \quad , \quad (3.3.8)$$

where from the previous definition of J_x^{mn}(3.3.2) we have

$$C_j^{mn}(z) = J_{0j}^{mn}(z)\cos\Phi_{Jj}(z) \quad , \qquad (3.3.9a)$$

$$B_j^{mn}(z) = J_{0j}^{mn}(z)\sin\Phi_{Jj}(z) \quad . \qquad (3.3.9b)$$

Here $\Phi_{Jj}(z)$ is not necessarily a linear function. The term J_{0j}^{mn} depends on z only for a linear wiggler. In a linear wiggler it contains a term that goes as $\sin(k_w z + \phi_w)$.

Now we make some definitions for the phases of the various quantities in the calculation. For convenience we temporarily drop the j subscripts. The following holds for all frequency components. We define the radiation phase as

$$\psi_s = k_s z - \omega t + \phi_s(z) \quad , \tag{3.3.10a}$$

$$= \Phi_s(z) - \omega t \quad , \tag{3.3.10b}$$

from $A_x^{mn} = A_{x0}^{mn} \sin \psi_s$. We define the wiggler phase as

$$\Phi_w = k_w z + \phi_w \; . \tag{3.3.11}$$

From these we define the ponderomotive phase as previously defined in section 2.2 as

$$\psi = \psi_s + \Phi_w \quad . \tag{3.3.12}$$

For a strong FEL interaction, the particles must move about the same speed as the ponderomotive well. We can then define a phase factor θ_p such that

$$\Phi_J(z) = \Phi_s(z) + \Phi_w(z) - \theta_p(z) \quad . \tag{3.3.13}$$

The definition of $\theta_p(z)$ is useful only if it varies slowly.

If we use our definitions to rewrite (3.3.7) we can obtain

$$\delta A_x^{mn} = \frac{J_{x0}^{mn}(z)\,\delta}{ck_s}\left[\sin\psi_s \cos\left(\Phi_w - \theta_p\right) + \cos\psi_s \sin\left(\Phi_w - \theta_p\right)\right] \quad . \tag{3.3.14}$$

If we write $\mathcal{A}_x^{mn}$ for the field after the integration, we obtain

$$\mathcal{A}_x^{mn}(z,t) = \left[A_{x0}^{mn} + \frac{J_{x0}^{mn}(z)\cos\left(\Phi_w - \theta_p\right)\delta}{ck_s}\right]\sin\psi_s + \frac{J_{x0}^{mn}(z)\sin\left(\Phi_w - \theta_p\right)\delta}{ck_s}\cos\psi_s \quad . \tag{3.3.15}$$

The new amplitude is

$$\mathcal{A}_{x0}^{mn} = \sqrt{\left[A_{x0}^{mn} + \frac{J_{x0}^{mn}(z)\cos\left(\Phi_w - \theta_p\right)\delta}{ck_s}\right]^2 + \left[\frac{J_{x0}^{mn}(z)\sin\left(\Phi_w - \theta_p\right)\delta}{ck_s}\right]^2} \quad ,$$

$$\cong A_{x0}^{mn}\left[1 + \frac{J_{x0}^{mn}(z)\cos\left(\Phi_w - \theta_p\right)\delta}{A_{x0}^{mn}\,ck_s}\right] \quad , \text{ for } \delta \to 0 \quad . \tag{3.3.16}$$

Thus the equation of evolution for the radiation amplitude becomes

$$\frac{dA_{x0}^{mn}}{dz} = \lim_{\delta \to 0} \frac{\mathcal{A}_{x0}^{mn} - A_{x0}^{mn}}{\delta} = \frac{J_{x0}^{mn}(z)\cos\left(\Phi_w - \theta_p\right)}{ck_s} \quad . \tag{3.3.17}$$

The change in the radiation phase $\phi_s(z)$ after the integration is given by

$$\delta\phi_s = \tan^{-1}\left[\frac{\dfrac{J_{x0}^{mn}(z)\sin\left(\Phi_w - \theta_p\right)}{ck_s}\delta}{A_{x0}^{mn} + \dfrac{J_{x0}^{mn}(z)\cos\left(\Phi_w - \theta_p\right)}{ck_s}\delta}\right] \quad . \tag{3.3.18}$$

From this one obtains the equation of evolution for $\phi_s(z)$,

$$\frac{d\phi_s}{dz} = \frac{J_{x0}^{mn}(z)\sin\left(\Phi_w - \theta_p\right)}{A_{x0}^{mn}ck_s} \quad . \tag{3.3.19}$$

To complete the reduction to a usable differential equation form, we need an explicit form of $J_{x0}{}^{mn}$. Returning to the specific case of a TE mode in a rectangular waveguide, we can evaluate $J_x{}^{mn}(z,t)$ explicitly using (3.2.6). We define

$$J_x(x,t) = I_x(z,t)\, f_J(x,y) \quad , \tag{3.3.20a}$$

$$\text{with} \int_0^a dx \int_0^b dy\, f_J(x,y) = 1 \quad , \tag{3.3.20b}$$

where $I_x(z,t)$ is the electron beam current, and $f_J(x,y)$ is the normalized transverse distribution of the electron beam. We have assumed that the transverse distribution of the electron beam is independent of z.

We can express $I_x(z,t)$ as

$$I_x(z,t) = -\, e\lambda(z,t)\, \overline{v_x(z,t)} \quad , \tag{3.3.21}$$

where $\lambda(z,t)$ is the one dimensional number density of electrons and $\overline{v_x(z,t)}$ is the average electron velocity at a particular z and t. We can write

$$\overline{v_x(z,t)} = \overline{\gamma^{-1}} \frac{e}{m_e c} A_x(z,t) = \overline{\gamma^{-1}} c a_x(z,t) \cong \overline{\gamma^{-1}}\, c a_w \sin\left(k_w z + \phi_w\right) \quad , \tag{3.3.22}$$

where small letter a's represent dimensionless vector potentials, as in section 2.2. These are obtained by multiplying the vector potential by $e/m_e c^2$. In (3.3.22), a_x is the total vector potential, including the radiation fields and the wiggler field, and a_w is the amplitude of the vector potential of just the wiggler field.

If we assume that the transverse distribution of the electron beam is a delta function in the center of the waveguide, then we obtain

$$J_x^{mn}(z,t) = \frac{8\pi ec}{ab} a_w \lambda_{eff} \frac{\cos\frac{m\pi}{2}\sin\frac{n\pi}{2}}{(1+\delta_{m0})} \sin\left(k_w z + \phi_w\right) \quad , \tag{3.3.23}$$

where

$$\lambda_{eff}(z,t) = \sum_{l}^{\#\ particles} \frac{\delta(z - z_l(t))}{\gamma_l} \quad . \tag{3.3.24}$$

One can see that the expansion of J_x^{mn} in (3.3.8) is equivalent to the expansion of λ_{eff} in (3.3.23). With this identification we can write

$$J_{0j}^{mn}(z) = \frac{8\pi ec}{ab} a_w \lambda_{0j} \frac{\cos\frac{m\pi}{2}\sin\frac{n\pi}{2}}{(1+\delta_{m0})} \sin\left(k_w z + \phi_w\right) \quad , \tag{3.3.25}$$

where λ_{0j} is the amplitude of the jth component in the expansion of λ_{eff}.

Now if we normalize the vector potentials by $\frac{e}{m_e c^2}$, and if we use (3.3.25), then the equations of evolution for the radiation fields, (3.3.17) and (3.3.19) can be written

$$\frac{da_{sj}^{mn}}{dz} = \mathcal{J}_j^{mn}\left[\sin\theta_{pj} - \sin\left(\theta_{pj} - 2k_w z\right)\right] \quad , \tag{3.3.26a}$$

$$\frac{d\phi_{sj}^{mn}}{dz} = \frac{\mathcal{J}_j^{mn}}{a_{sj}^{mn}}\left[\cos\theta_{pj} - \cos\left(\theta_{pj} - 2k_w z\right)\right] \quad , \tag{3.3.26b}$$

with

$$\mathcal{J}_j^{mn} = \frac{4\pi e^2}{m_e cab}\, a_w\, \lambda_{0j} \frac{\cos\frac{m\pi}{2}\sin\frac{n\pi}{2}}{(1+\delta_{m0})} \quad . \tag{3.3.26c}$$

3.4 Reduction of Differential Equations to KMR Form.

Only one substitution really needs to be made to reduce the radiation evolution equations to the form of the KMR equations derived in section 2.2. We will drop all j subscripts in this section since the KMR equations follow only a single frequency. For convenience we will also drop all the mn superscripts and follow only a single transverse mode. To start, we view fig 3.4.

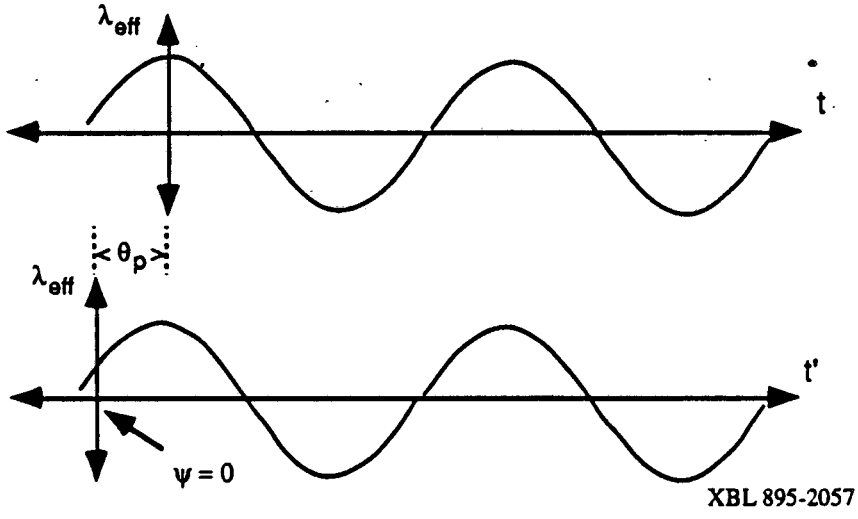

Figure 3.4 Change of coordinates. Primed frame has t′ = 0 when ψ = 0.

In Fig. 3.4, λ_{eff} is plotted. In the top plot, the coordinates are chosen so that only the cosine component of λ_{eff} is nonzero. In this case

$$\lambda_{eff}(z(t)) = \lambda_0(z) \cos \omega t \quad , \tag{3.4.1a}$$

and $$\lambda_0(z) = \frac{\omega}{\pi} \int_0^{\frac{2\pi}{\omega}} dt\, \lambda_{eff}(z(t)) \cos \omega t \quad . \tag{3.4.1b}$$

If we use the t' coordinates instead, then

$$\lambda_{eff}(z(t')) = \lambda_0(z) \cos \left(\omega t' - \theta_p\right) \quad ,$$

$$= \lambda_0(z) \cos \theta_p \cos \omega t' + \lambda_0(z) \sin \theta_p \sin \omega t' \quad . \tag{3.4.2a}$$

So

$$\lambda_0(z) \cos\theta_p = \frac{\omega}{\pi} \int_0^{\frac{2\pi}{\omega}} dt' \lambda_{eff}(z(t')) \cos \omega t' \quad , \tag{3.4.2b}$$

and $$\lambda_0(z) \sin\theta_p = \frac{\omega}{\pi} \int_0^{\frac{2\pi}{\omega}} dt' \lambda_{eff}(z(t')) \sin\omega t' \quad . \tag{3.4.2c}$$

Substituting eq. (3.3.24) and performing the integration gives

$$\lambda_0(z) \cos\theta_p = \frac{\omega}{\pi} \sum_l \frac{\cos \omega t'_l}{v_l \gamma_l} \quad , \tag{3.4.3a}$$

$$\lambda_0(z) \sin\theta_p = \frac{\omega}{\pi} \sum_l \frac{\sin \omega t'_l}{v_l \gamma_l} \quad , \tag{3.4.3b}$$

where v_l is the velocity of the lth electron. Noting that t'=0 corresponds to the point where ψ=0, and noting that the time dependence of ψ goes as ωt, then we can replace ω_l in eqs. (39) with ψ_l, where ψ_l is the ponderomotive phase of the lth electron. Thus

$$\lambda_0(z)\cos\theta_p = \frac{\omega}{\pi} N_{buc} \left\langle \frac{\cos\psi}{v\gamma} \right\rangle \quad , \tag{3.4.4a}$$

$$\lambda_0(z)\sin\theta_p = \frac{\omega}{\pi} N_{buc} \left\langle \frac{\sin\psi}{v\gamma} \right\rangle \quad , \tag{3.4.4b}$$

where N_{buc} is the total number of electrons per period , and $< >$ denotes an average over particles. For reduction to the KMR form of the equations, we set v=c although this is not a good approximation in all cases. Combining eqs. (3.4.4) with eqs. (3.3.26) gives

$$\frac{da_s}{dz} = \frac{8\pi Ie}{m_e c^3 k_s ab} \frac{\cos\frac{m\pi}{2}\sin\frac{n\pi}{2}}{(1+\delta_{m0})} a_w \left\langle \frac{\sin\psi}{\gamma} \right\rangle \quad , \tag{3.4.5a}$$

and $$\frac{d\phi_s}{dz} = \frac{8\pi Ie}{m_e c^3 k_s ab} \frac{\cos\frac{m\pi}{2}\sin\frac{n\pi}{2}}{(1+\delta_{m0})} \frac{a_w}{a_s} \left\langle \frac{\cos\psi}{\gamma} \right\rangle \quad , \tag{3.4.5b}$$

where $I = \dfrac{e\omega N_{buc}}{2\pi}$.

Eqs. (3.4.5) are just the KMR equations for FEL radiation in a waveguide[5][21].

Chapter 4

Effect of Dispersion on Single Frequency FEL's

4.1 Waveguide Corrections to the KMR FEL Theory

In this chapter we will examine some of the effects waveguides have on FEL's that can be described by a modified KMR theory. In his thesis, Jonathan Wurtele has considered those effects that occur because of multiple transverse waveguide modes[5]. Therefore, we will confine ourselves here to effects cause by dispersion on a single transverse mode.

We begin by considering how the particle dynamics of the electrons are changed because of interactions with the waveguide. The particle equations of motion for an FEL in a waveguide are

$$\frac{d\gamma_j}{dz} = -\frac{\omega a_s a_w}{2c\ \gamma_j}\sin\psi_j \quad , \tag{4.1.1a}$$

and $$\frac{d\psi_j}{dz} = k_w + \delta k_s + \frac{d\phi_s}{dz} - \frac{\omega}{2c\gamma_j^2}\left[1 + \frac{a_w^2}{2}\right] \quad . \tag{4.1.1b}$$

The only change from the free space FEL particle equations is the introduction of the term δk_s in the ψ equation. Explicitly $\delta k_s = k_s - {}^{\omega}/_{c}$, which we set to zero for free space propagation in section 2.2. The term δk_s is negative in magnitude and is absolutely necessary for describing an FEL in a waveguide. The magnitude of δk_s compared to k_w is to some extent a measure of the dispersion of the waveguide.

We now examine the FEL resonance condition of (2.3.1). Modified for a waveguide, this becomes

$$\gamma_r^2 = \frac{\omega}{2c\left(k_w + \delta k_s\right)}\left(1 + \frac{a_w^2}{2}\right) \quad . \tag{4.1.2}$$

If we solve this for the magnetic field strength a_w, we get

$$a_w = \sqrt{\frac{4c\left(k_w + \delta k_s\right)\gamma_r^2}{\omega} - 2} \quad . \tag{4.1.3}$$

As the dispersion increases, δk_s becomes more negative and therefore a_w decreases. One consequence of dispersion is that the magnetic field required to maintain resonance is decreased. Physically the larger a_w is, the more the parallel velocity of the electrons are slowed. The resonance condition has to do with the phase of the radiation, so the radiation phase velocity is the important quantity here. In a waveguide the phase velocity of the radiation is increased as the dispersion is increased. Therefore , a_w doesn't need to be as large to match the electron parallel velocity to the radiation phase velocity.

One interesting consequence of (4.1.3) is that it sets a minimum γ_r for an FEL. We must have

$$\gamma_r > \sqrt{\frac{\omega}{2c\left(k_w + \delta k_s\right)}} \quad , \tag{4.1.4}$$

for the FEL resonance to be possible. This sets a limit on the amount of energy that can be

extracted from tapered wiggler FEL's. In a waveguide this constraint can be much more severe. The term $k_w + \delta k_s$ can approach zero(remember δk_s is negative) which means that the lower limit for γ_r can become quite large.

If one carries out the linear analysis of section 2.3 with the FEL equations (4.1.1), one obtains a modified value for the synchrotron wave number k_{synch}(2.3.7) and the bucket height $\delta\gamma_{max}$(2.3.8). These are

$$k_{synch} = \left(k_w + \delta k_s\right)\left[\frac{2a_s a_w}{1 + \frac{a_w^2}{2}}\right]^{\frac{1}{2}} , \qquad (4.1.5)$$

and

$$\delta\gamma_{max} = \left[\frac{\omega a_s a_w}{c\left(k_w + \delta k_s\right)}\right]^{\frac{1}{2}} . \qquad (4.1.6)$$

In the expression for k_{synch}, as the dispersion increases both a_w and the term $(k_w + \delta k_s)$ decrease. Thus one result of dispersion is that synchrotron periods become longer. The expression for the bucket height is less obvious because there are terms in both the numerator and denominator that decrease with dispersion. We can note however from (4.1.3) that a_w goes roughly as $\sqrt{k_w + \delta k_s}$ so that on balance, the bucket height ought to increase as dispersion increases.

Waveguide dispersion also has an effect on FEL gain. Using the results of section 2.5 we can see that approximately, the only particle quantities that affect the gain are a_w and γ_r, which we keep fixed. From section 2.5 we know that in the exponential gain regime the output power goes as e^{gz}, where g is proportional to $[a_w]^{2/3}$. In the linear gain regime, the change in output power goes as a_w^2. Since we have already determined that a_w decreases as the dispersion is increased, then one would expect to find that the gain decreases as the dispersion is increased.

From all the previous analysis, one might conclude that something important if not catastrophic happens when $k_w + \delta k_s = 0$. If this condition occurs, then all our calculated quantities are undefined. Physically, this condition is the same as setting the ponderomotive phase velocity equal to c. Since the electrons can never actually go at the speed of light, the FEL resonance is impossible to achieve. This can only occur in a waveguide since the FEL ponderomotive potential always moves at less than the speed of light in a vacuum. The condition that the ponderomotive velocity should be less than c leads to the following inequality:

$$\omega > \frac{c}{2k_w}\left(k_w^2 + \frac{\omega_{cutoff}^2}{c^2}\right) \quad . \tag{4.1.7}$$

This inequality is more restrictive than just requiring the frequency in the waveguide to be above cutoff. For the ELF experiment at Livermore k_w = 0.641 cm^{-1}, and

$\omega_{cutoff}=3.24\times10^{10}$ rad/sec. The condition (4.1.7) requires that $\omega > 3.69 \times 10^{10}$ rad/sec. If k_w becomes small (the wiggler wavelength becomes large), then this inequality can give a much higher value of ω than the cutoff.

The dispersion in a waveguide can also cause two resonances to exist for a particular set of physical parameters. To see how this can occur, please view Fig. 4.1.

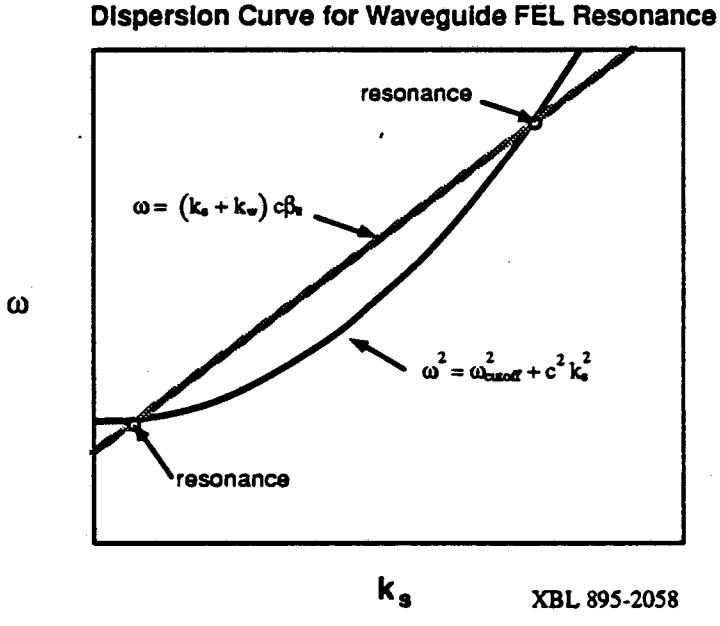

Figure 4.1 Black denotes the waveguide dispersion curve and grey denotes the FEL dispersion relation.

Here we have plotted the waveguide dispersion curve and the FEL dispersion curve. The FEL dispersion curve consists of setting the ponderomotive phase velocity equal to $\beta_{\parallel}$

which is the parallel velocity of the electrons divided by c. Note that for most parameters these curves will intersect in 2 points. In principle it is possible to have only a single intersection, but this would mean that $k_w c\beta_{||} > \omega_{cutoff}$ which is difficult to realize in practice. The points of intersection can be calculated. They turn out to be

$$\frac{\omega}{c} = \frac{\frac{k_w}{\beta_{||}} \pm \sqrt{k_w^2 - \frac{\omega_{cutoff}^2}{c^2}\left(\frac{1}{\beta_{||}^2} - 1\right)}}{\left(\frac{1}{\beta_{||}^2} - 1\right)} \quad . \tag{4.1.8}$$

For the parameters of the ELF experiment at Livermore the resonances occur at 34.6 GHz and 6.5 GHz[38]. Using a computer simulation, to be described in great detail in the next chapter, the output spectrum of the ELF experiment was calculated for an initial input of white noise. The results are plotted in Fig. 4.2.

Note that since the scale is a log scale, the lower resonance has a significantly lower gain. The lower resonance is also much narrower. These peaks can be amplified simultaneously only in the linear growth regime. The resonances each have a different bunch length, so as the interaction of the radiation with the beam becomes nonlinear, each resonance will interfere with the amplification of the other. If an FEL is started from noise, one would expect to measure only the upper resonance because of its higher gain.

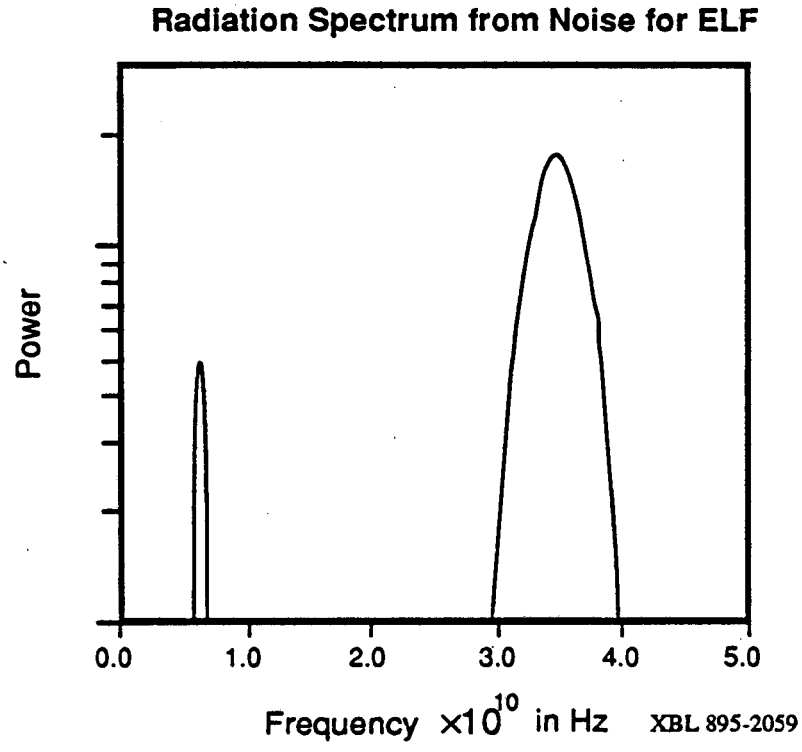

Figure 4.2 Radiation spectrum amplified from white noise. The fact that there are two peaks is due to waveguide dispersion. The frequency at each peak has the same phase velocity.

4.2 Efficiency Enhancement in Waveguide FEL's

In section 2.6 a simulation was run of a tapered wiggler FEL modeled on the ELF experiment at Livermore. It was demonstrated that the efficiency of a tapered FEL is limited by the percent of the current trapped in the bucket (ponderomotive well). For the parameters in that simulation, one can see that the trapping efficiency was on the order of 68%(see Fig. 2.10). This leaves considerable room for improvement. In this section, we will describe a scheme for improving this trapping efficiency by altering the waveguide in the middle of the FEL.

In the last section we saw that the waveguide can have a significant effect on the FEL gain and bucket height (eq. 4.1.6). To see how these properties can be used, let's consider the desirable characteristics of a tapered FEL.

In preparing for the taper it is desirable to have a tightly bunched electron beam. Now as a general rule, nonlinearities tend to cause the electron distribution to fill the entire bucket during bunching. Therefore, during bunching, it is better to have a small bucket. This implies that a bunching section should have as small an amount of

dispersion as possible. Since small dispersion also implies higher gain, a less dispersive bunching section has more than one feature to recommend it. This is subject to practical considerations such as the gap in the wiggler magnets and the maximum attainable field in the wiggler magnets.

When tapering is started, it is desirable to have the largest bucket possible and the electron beam bunched as tightly as possible in the center of the bucket. If the beam is not tightly bunched, then a taper will not succeed in decelerating most of the electrons. The large bucket implies that a large amount of dispersion would be beneficial in this region.

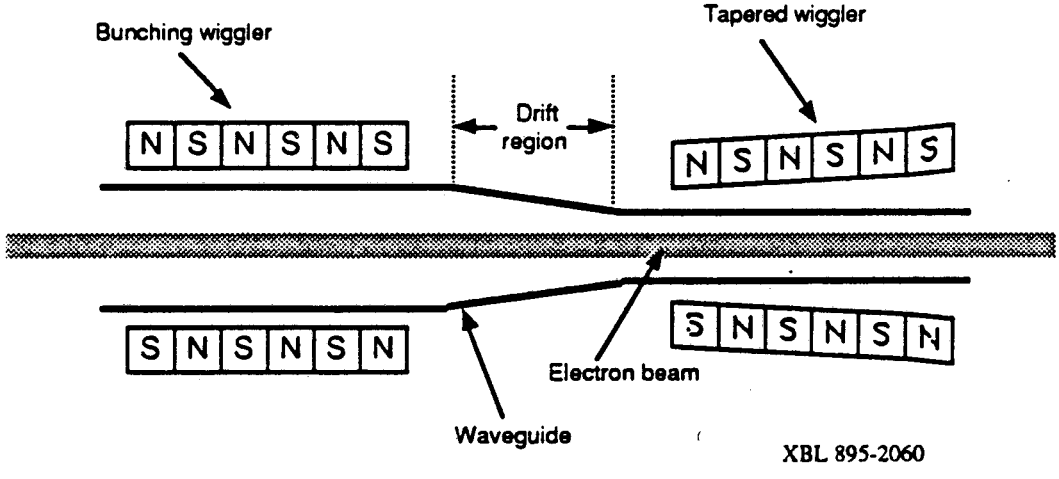

Figure 4.3 Configuration for enhancing the extraction efficiency of a waveguide FEL.

One possible scheme to maximize FEL efficiency is shown in Fig. 4.3. The FEL is split into two parts. First we have a bunching wiggler section. The waveguide size and wiggler parameters are chosen so as to maximize the gain and to minimize the bucket height. The second wiggler section is tapered and its parameters and the waveguide are chosen so as to maximize the bucket height. The drift region is used to match between the two sections. In this drift region the waveguide is tapered and any necessary magnets are added to match between the two wigglers.

Before showing a numerical example, we will derive the matching conditions for the radiation and the electron beam across the drift region in a rectangular waveguide. For the radiation, the change in phase across the drift region can be written

$$\Delta\phi_{drift} = \int_0^L dz\, k_s(z) = \int_0^L dz \sqrt{\left(\frac{\omega}{c}\right)^2 - \pi^2\left[\left(\frac{m}{a(z)}\right)^2 + \left(\frac{n}{b(z)}\right)^2\right]} \quad , \qquad (4.2.1)$$

where m and n are the transverse mode numbers, a and b are the width and height of the waveguide, and L is the length of the drift region. If we have an electron bunch entering the waveguide at t = 0, then the change in radiation phase relative to the electron bunch at the exit of the drift region is given by

$$\Delta\phi_{rel} = \Delta\phi_{drift} - \omega t_b = \Delta\phi_{drift} - \frac{\omega L}{c}\sqrt{1 - \gamma^{-2}} \quad , \qquad (4.2.2)$$

where t_b is the time required for the electron bunch to traverse the drift region. The condition for matching then becomes $\Delta\phi_{rel} = 2\pi n$, where n is any integer. Most of the parameters are already determined by design considerations for the two wiggler sections. However, the length of the drift region, L, can always be adjusted to satisfy the matching condition.

For a 1-D FEL simulation, the matching condition is all we require. In a real FEL there are further considerations necessary in the drift region. The waveguide taper must be designed to avoid unwanted mode conversion. Also in a real FEL, the wiggler end fields from both wiggler sections will intrude into the drift region. Additional focussing elements may be necessary, making the relation (4.2.2) overly simplistic. While the actual implementation of the scheme described in this section might be more complicated than a 1-D analysis would suggest, there seem to be no major impediments.

In addition to allowing one to alter the bucket height, the scheme of Fig. 4.3 allows one to introduce a phase shift before entering the tapered wiggler. This follows from (4.2.2) where we need not set $\Delta\phi_{rel} = 2\pi n$. When tapering is initiated, particles tend to be lost from the tail end of the bunch. If we introduce a phase shift so that the electron

bunch is slightly advanced relative to the FEL bucket, then this tendency can be minimized.

One potential problem with this scheme is that we noted in the last section that for a particular set of physical parameters there was a limit to how low the resonance energy can get in a waveguide(4.1.4). If the waveguide is fairly dispersive then this value could be rather high. Whether this is a problem or not will depend on the particular application. The dispersion lowers the necessary wiggler field strength to achieve resonance with the electrons. If the dispersion is too high then resonance might not be achievable at the desired energies with any finite wiggler field. However, magnets at lower field strengths are generally cheaper to manufacture. This might produce a tradeoff between the amount of energy extraction and costs. At any rate, the highest bucket height possible is desirable at the entrance of the tapered wiggler. If the minimum resonance energy is reached further down the wiggler it should be possible to taper the waveguide to ease this restriction, since by the time it becomes a problem the radiation field should be large enough to provide a rather large bucket.

A simulation has been performed to demonstrate the scheme of Fig. 4.3. The results are shown in Figs. 4.4 - 4.7. The design is not optimal for the scheme, but is modeled on the ELF experiment at Livermore and uses the parameters from Table III. The two simulations are identical up to 1.6 meters where the untapered FEL reaches saturation. In both cases the second wiggler section is 2.4 meters in length. The first simulation is just that of ELF for the particular taper used with no drift region. The taper was chosen so as to lower the energy to $\gamma_r = 4.3$ at the end of the wiggler. This value was chosen so as to avoid any problem with minimum resonance energies. This first simulation is shown in the (a) frames of the plots. The second simulation used a drift region that reduced the height of the waveguide from 2.9cm to 2.0cm. It also introduced a phase shift of the electrons of 0.7 radians relative to the ponderomotive well. This simulation is shown in the (b) frames of the plots. The distances in the plots show the distance from the start of the second wiggler.

Table III

Beam Energy	4.14 Mev
Beam Energy in γ	8.1
Beam Current	800 amperes
Wiggler wavelength	9.8 cm
Radiation frequency	34.6 GHz
Waveguide width	9.8 cm
Waveguide height	2.9 cm
Input radiation power	60 KWatts / TE^{01} mode
Wiggler Peak Field	4.67 KGauss

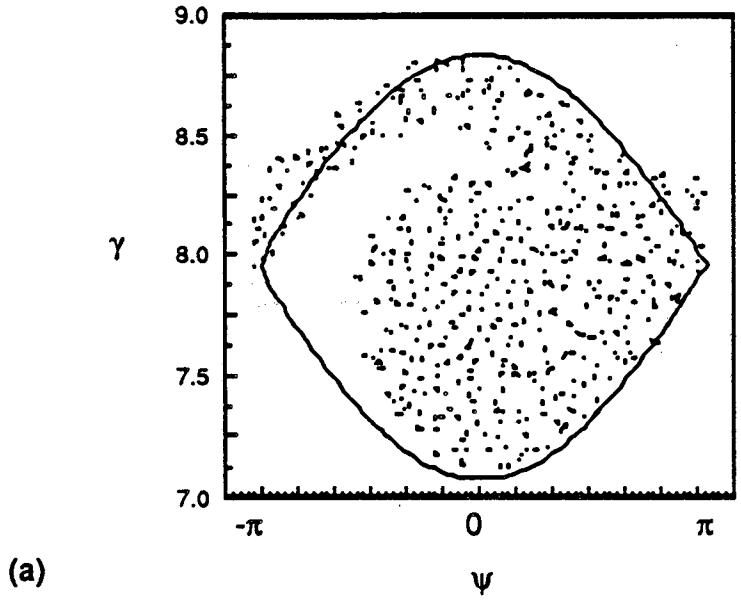

(a)

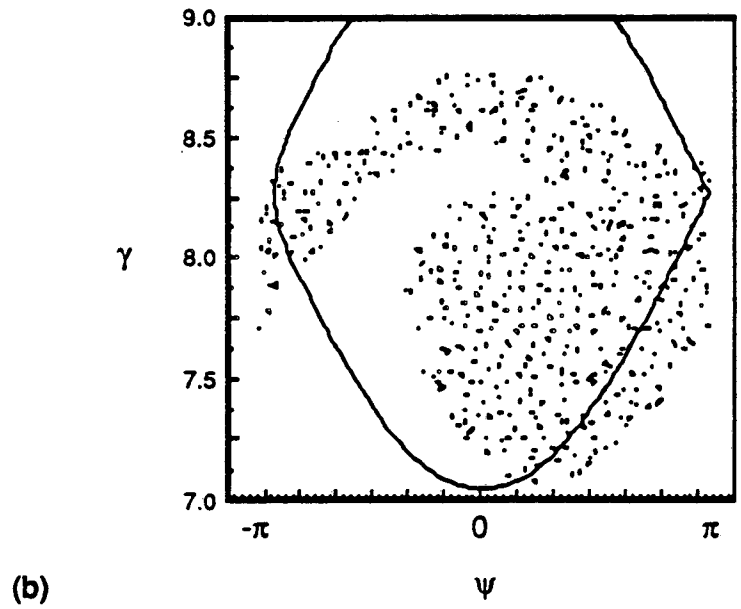

(b)

XBL 895-2061

Figure 4.4 The smaller waveguide in (b) has a larger bucket area allowing increased trapping of electrons. Electrons closest to the separatrix are likely to be lost.

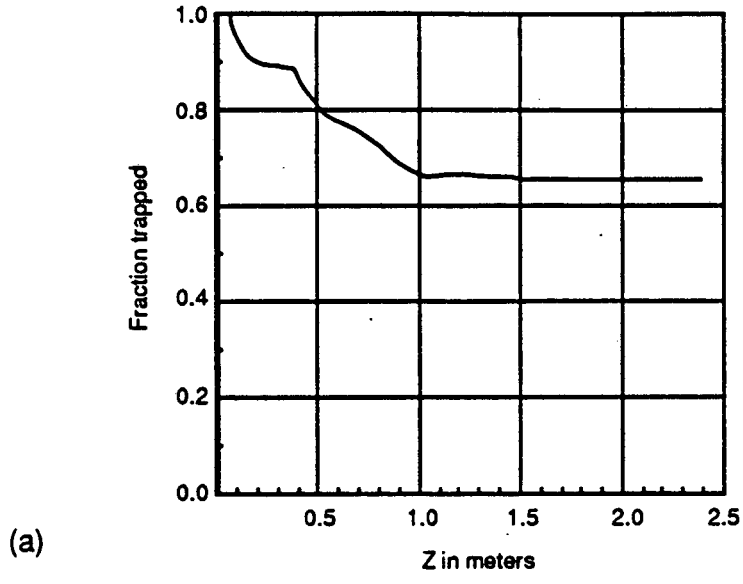

(a)

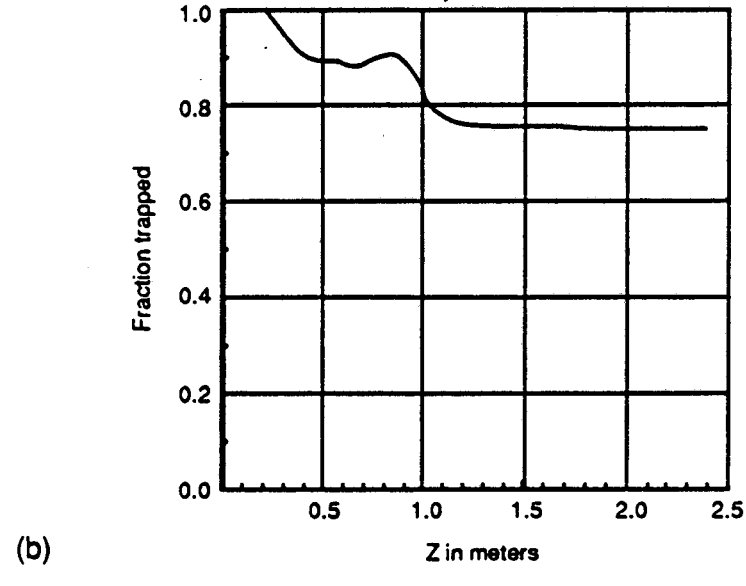

(b)

XBL 895-2062

Figure 4.5 Trapping fraction is greater when the smaller waveguide is used. The distances are from the entrance to the tapered wiggler.

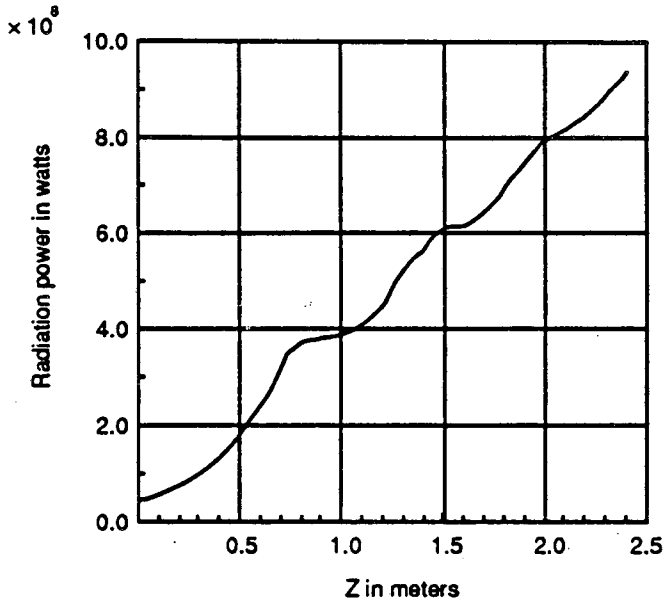

(a)

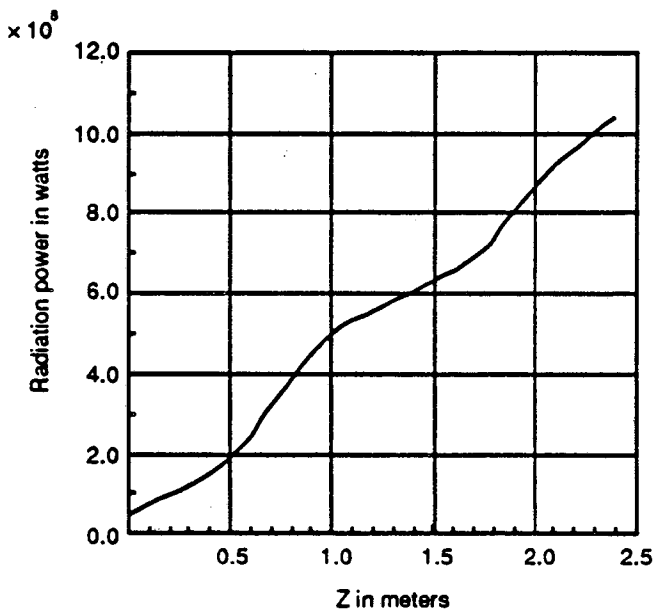

(b)

XBL 895-2063

Figure 4.6 The smaller waveguide in (b) produces more power.

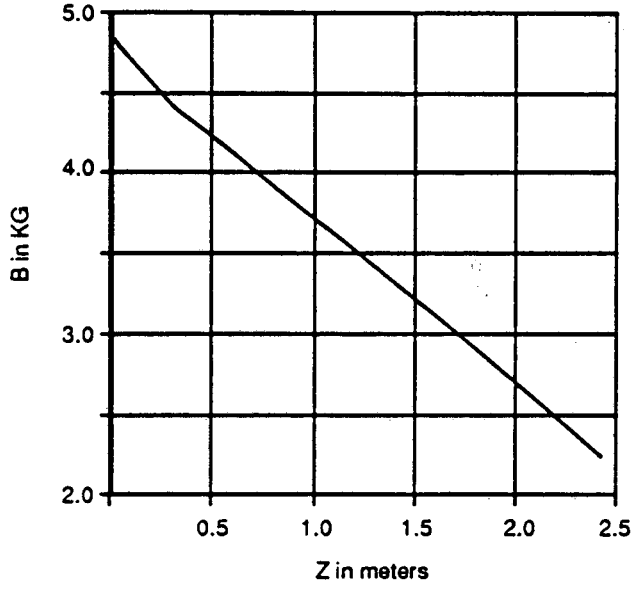

(a)

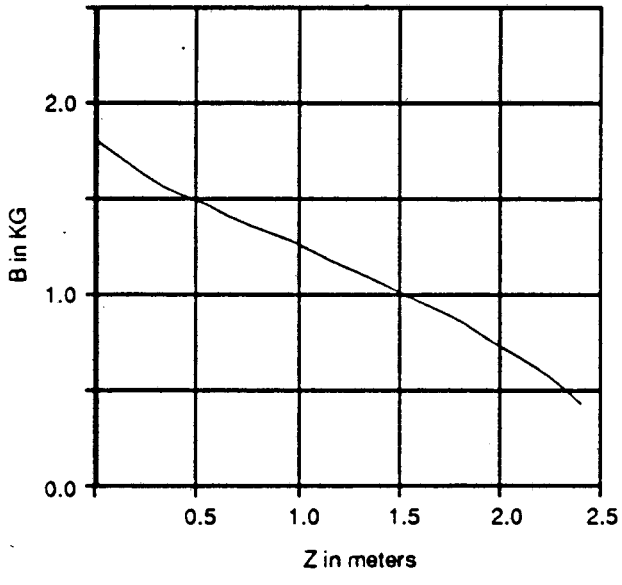

(b)

XBL 895-2064

Figure 4.7 Comparison of the tapers for the different waveguide sizes.

The first thing to notice is the size of the bucket heights for each simulation at the beginning of the second taper. This is shown in Fig. 4.4. The separatrices drawn in the figures are just to estimate the actual bucket since in reality an FEL is a highly nonlinear device. One can see that for the more dispersive waveguide, the bucket is significantly larger. This can be seen in Fig. 4.5 to lead to a higher degree of trapping and therefore in Fig. 4.6 to a larger amount of radiated power. In Fig. 4.7 we can see that the wiggler fields required in the (b) simulation are less than half of what was required in the (a) simulation.

For the ELF-like parameters used in these simulations, the trapping efficiency improvement is from about 65% to 75%. This is significant but not tremendous. FEL's like ELF arenot designed to be efficient and reliable power sources but are meant to be a flexible experimental apparatus. In the future as FEL power sources become routine, designers will need every trick available to make the FEL more efficient and inexpensive.

Chapter 5

Sidebands in Waveguide FEL's

5.1 General Description of the FEL Sideband Instability

In this chapter, the FEL sideband instability will be studied in great depth. An analysis based on formalism from nonlinear optics will be developed and the results will be compared with computer simulations. Of primary interest are the structure of the sideband spectrum and those conditions that can lead to suppression of the sideband instability.

Before discussing the details of sideband research we will introduce the subject with a heuristic model of FEL sidebands. An FEL that is saturated introduces an additional frequency to the electron motion. Bunching and subsequent trapping of electrons in an FEL can be described by electron interaction with a ponderomotive potential. In an FEL this potential is formed by a beat wave between the wiggler field and the radiation field. This beat wave forms a train of potential wells that travel at a uniform velocity. If the initial electron velocity is close enough to the velocity of the potential wells then there will be a strong interaction and the particles will bunch as they give up energy to the radiation field. When the radiation field saturates, there will be some electrons with insufficient energy to escape from the potential wells. These

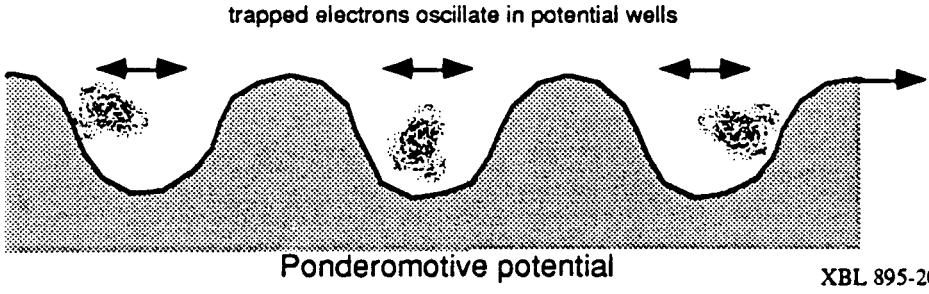

Figure 5.1 Electrons trapped in the ponderomotive potential undergo small oscillations at the synchrotron frequency. These oscillations modulate the original electron current and therefore can interact strongly with radiation frequencies that have appropriate matching conditions.

electrons are said to be trapped. For deeply trapped electrons, the ponderomotive potential appears the same as a pendulum potential. These electrons oscillate in the well at what is known in the FEL literature as the synchrotron frequency. This is analogous to the bounce frequency used in plasma physics.

Synchrotron oscillations are only apparent in the regime of a saturated FEL. When the radiation is growing rapidly, the ponderomotive potential steepens and therefore the synchrotron frequency changes too rapidly to be well defined. The synchrotron oscillations modulate the electron beam so as to produce additional current components at the radiation fundamental plus and minus the synchrotron frequency. These current components can produce an instability that grows exponentially. This is a parametric amplification process and it is important since it can lead to degradation of

the FEL output spectrum and it can cause the electrons to be detrapped from the original ponderomotive well.

Figs. 5.2 and 5.3 show some computer simulations to illustrate the nature of the synchrotron oscillations.

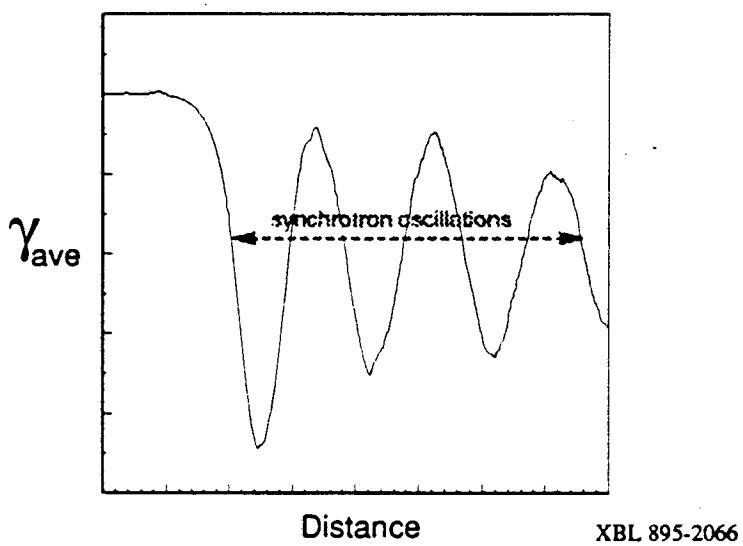

Figure 5.2 Typical evolution for the average energy of the electrons in an FEL. This simulation was chosen for the pronounced synchrotron oscillations after saturation.

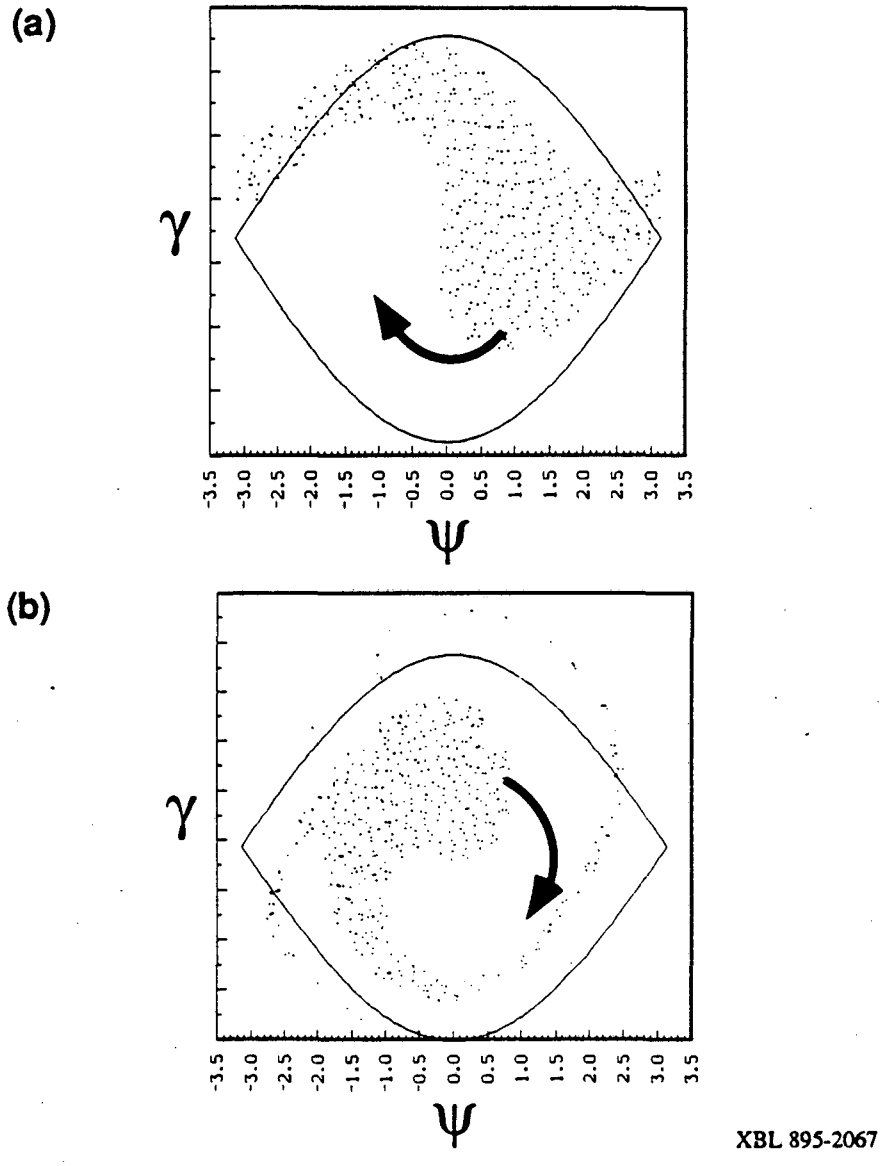

Figure 5.3 Simulations of the bunching and subsequent oscillation of the electrons in an FEL. The oscillation is represented in phase space as an orbit around the FEL resonance. The separatrices are calculated according to a linearized FEL analysis and are plotted to give an idea of the region in which electrons are trapped.

5.2 Description of Previous FEL Sideband Research

In this section we briefly review previous sideband research. FEL sidebands have been the subject of many studies because of the potential impact on FEL performance. Research has mostly concentrated on FEL's in an oscillator configuration, though sidebands can also occur in high-gain amplifiers. In either case the physical mechanism is the same.

One of the first papers on FEL sidebands was written by Norman Kroll and Marshall Rosenbluth[42]. It is an impressive work, since it predicted many properties of sidebands that were subsequently confirmed.

Kroll and Rosenbluth begin by writing a set of two frequency equations for the particle evolution in terms of γ and ψ, with one frequency being the FEL fundamental and the other being the FEL sideband. Assuming that the amplitude of the sideband is much smaller than that of the fundamental, one can derive a pendulum equation(as in eq. (2.3.3)) where there is a perturbative forcing term due to the sideband frequency. The phase of the particles is expressed in terms of ψ and ψ_R, with ψ_R being the phase defined by the wiggler field and the sideband wave.

The gains of the fundamental and the sideband are written

$$g_s = \frac{\omega_p^2 \, a_w}{2\omega_s c \, a_s} \int_0^L \overline{\left(\sin \psi/\gamma\right)} dz \quad , \tag{5.2.1a}$$

and $$g_R = \frac{\omega_p^2 \, a_w}{2\omega_R c \, a_R} \int_0^L \overline{\left(\sin \psi_R/\gamma\right)} dz \quad , \tag{5.2.1b}$$

where these are integrals over the equations for the field amplitudes of the fundamental and the sideband. The R represents sideband quantities and the bar over the integrand indicates an average over particles. The equations are the same in all respects to (2.2.16) except for slightly different normalizations. The authors do not state so explicitly, but the averages are equivalent to picking out the respective Fourier components of the fundamental and the sideband.

Next, the authors calculate the quantity $G = g_R/g_s$, which is the relative gain of the sideband and the fundamental. Since the sideband is being treated as a small perturbation in the pendulum equation, the particle orbits can be integrated to first order in the sideband amplitude. Assuming perfect bunching, i.e. all the particles enter the wiggler exactly on a single point, the orbits are inserted into the expressions (5.2.1) and integrated. The result is

$$G = \frac{\Omega L}{4\sin 2\psi_r}\frac{\omega_R}{\omega_s}\left[\frac{\sin^2\left((\Omega_R - \Omega)L/2\right)}{\left[(\Omega_R - \Omega)L/2\right]^2} - \frac{\sin^2\left((\Omega_R + \Omega)L/2\right)}{\left[(\Omega_R + \Omega)L/2\right]^2}\right] , \qquad (5.2.2)$$

where Ω is equivalent to k_{synch} in (2.3.7), L is the length of the wiggler, ψ_r is the resonant ponderomotive phase, and $\Omega_R = \frac{\omega_s - \omega_R}{\omega_s} k_w$. The result they achieve is somewhat worrisome because of the $\sin\psi_r$ in the denominator. Since ψ_r is nonzero only in tapered wigglers this would imply that something qualitatively different happens in an untapered wiggler, which is not actually true. However, their result allows them to draw some of the following conclusions.

This expression shows a resonance at $\Omega_R = \pm \Omega$. These resonances correspond to the lower and upper sidebands. The relative gain for the upper and lower sidebands are opposite in sign. This means that in a situation when the lower sideband is amplified, the upper sideband should be damped. From this result, they make the assertion that sideband generation is a process similar to stimulated Raman scattering where the lower sideband is the Stokes wave and the upper sideband is the anti-Stokes wave. This is a correct assertion, but they make no further use of the analogy.

In the latter part of their paper, Kroll and Rosenbluth perform a kinetic analysis for FEL sidebands. They conclude that for most reasonable particle distributions where the

particle density is higher in the center of the FEL bucket, it is the lower sideband that will be driven by the instability. If the particle distribution increases in amplitude away from the center of the bucket, then the upper sideband should be unstable.

Another useful study of the FEL sideband instability was made by Colson[43]. He examines three regimes: the short pulse oscillator, the long pulse oscillator, and the high gain amplifier. To generalize his results he expresses the equations of evolution in terms of dimensionless parameters and uses a numerical simulation to draw conclusions.

In short pulse oscillators it is important to match the light pulse and the electron pulse for each pass of the oscillator. Due to "laser lethargy" effects, however, the gain is preferentially deposited at the tail of the light pulse. Therefore the optimum gain would be achieved by making the resonator a little bit shorter than matching conditions would indicate. Colson finds that when this "desynchronism" is set to maximize the gain of the fundamental, then the sideband instability can grow. This causes sharp spikes in the radiation pulse and produces a broad optical power spectrum. If the desynchronism is large enough to reduce the gain of the fundamental, then the sideband instability can be suppressed. Thus one way to suppress sidebands is to alter the slippage between the electron pulse and the optical pulse for each pass through the oscillator.

For an FEL, there is a characteristic slippage length. This is determined by the relative velocities of the electrons and the radiation pulse. If both pulses started at the same point at the beginning of the wiggler, they would be separated by this slippage length at the end of the wiggler. For modeling long pulse oscillators, where one can have electron pulses that are many slippage distances long, Colson introduces a useful numerical concept. It is somewhat redundant to follow the entire electron beam in a simulation since sections in different parts of the beam will exhibit the same behavior. The initial noise might be somewhat different, but in an oscillator this is not very important. Colson uses only a small slice of the electron beam with periodic boundary conditions. These "wrapped window" simulations are able to capture the sideband behavior with a great savings in computer time. The size of the window is essentially a limit on the number of modes that can be examined.

Some properties of FEL sidebands are observed in both the short and long pulse regimes. Increasing the current or increasing the Q of the resonator also increases the sideband instability. Using a tapered wiggler decreases the production of sidebands. Colson attributes this to the fact that tapering decreases the depth of the ponderomotive wells and a smaller number of electrons are trapped in the FEL bucket.

Colson also produces a few conclusions for sidebands in FEL amplifiers. He finds a current threshold for the sideband instability. Also, in an amplifier, the initial noise is quite important as opposed to an oscillator where it is not. The lower the input noise level in an amplifier, the lower the sideband power should be.

Another interesting contribution to the FEL sideband literature has been made by Davidson and Wurtele. They develop their own formalism that allows them to examine sideband stability with a dispersion analysis[44]. Using this formalism they are able to study the effect of untrapped electrons on the sideband instability[45]. This is important since in any real FEL, the trapping of electrons is imperfect. Some electrons are always untrapped. Their analysis suggests that if the fraction of untrapped electrons remains less than about 0.2, then the sideband instability is relatively unchanged. When the fraction of untrapped electrons becomes greater than 0.2, then there can be substantial modification of the sideband spectrum. Generally, the untrapped electrons seem to produce power on the opposite side of the fundamental from the normal sideband instability, i.e. if the lower sideband is usually unstable then the untrapped population will add to the upper sideband spectrum.

Another contribution to the FEL sideband literature was made by Riyopoulos and Tang[47]. Their general approach to the sideband problem is similar in nature to that of Kroll and Rosenbluth[46]. Using kinetic theory, they examine the effect of sidebands on electron trapping. When the sideband power passes a certain threshold, then the electron orbits no longer quite close on themselves and the system becomes stochastic. Riyopoulos and Tang estimate the diffusion rate of these electrons and compare this to numerical simulations. The theory and the simulation seem to match quite well. The detrapping of electrons due to stochastic diffusion can limit FEL performance, though only in tapered wiggler FEL's will the performance degradation be severe.

The analyses mentioned here have all used 1-D equations to predict the behavior of FEL sidebands. Sharp and Yu have performed an analysis that predicts the effects of finite beam size on sideband generation[48][49]. They use a 2-D Vlasov equation to describe particle motion in a helical wiggler FEL. While the effects of a 2-D geometry are included, the effects of betatron motion on sidebands are ignored. They find that 2-D effects can be ignored when the following conditions are satisfied: the slowly varying radiation phase is close to the value predicted by 1-D theory, the sideband mode is largely confined to a region where the electron beam density variation is small, and the wall radius of the beam pipe enclosing the system is more than twice that of the electron beam radius. They also

derive an analytic expression that is an inequality which estimates when 2-D effects are negligible.

Finite radius electron beams seem to decrease the growth of the sideband instability. Sharp and Yu have numerically observed as much as a 40% drop in sideband growth over the 1-D case. Another effect is that the peaks for the sideband gain are further from the fundamental than in the 1-D case.

5.3 Previous Work on FEL Sidebands in Waveguides

As work progressed on the Two-Beam Accelerator project, where electron bunches undergo many synchrotron oscillations in the device, people became interested in the physics of sidebands in waveguides. It was suggested by myself that if the group velocity of the radiation was equal to the electron velocity, then no information could travel along the beam and therefore no longitudinal instabilities would be able to develop.

The physics of the regime where the radiation group velocity and the electron velocity are equal is not well described by FEL equations that use the usual paraxial or eikonal approximation. Since the eikonal approximation neglects second derivatives, the radiation dispersion is completely absent from the evolution equations. Another problem involves the estimate of the sideband location. The usual way to estimate sideband location is to say that the sidebands will be separated from the fundamental by an amount equal to the synchrotron wavelength[50]. Explicitly

$$\left[\left(k_s \pm \Delta k\right) + k_w\right] z - \left(\omega_s \pm \Delta\omega\right) t \cong k_{synch}\, z \quad , \tag{5.3.1}$$

where Δk and $\Delta\omega$ are the shifts of the sideband from the fundamental. If $v_{||}$ is the parallel electron velocity then $z \cong v_{||}t$. If we use the resonance condition $\omega_s = (k_s + k_w)v_{||}$, and use

$\Delta\omega \approx \frac{d\omega}{dk}\Delta k = v_{group}\Delta k$, then one can express $\Delta\omega$ as

$$\Delta\omega \cong \frac{k_{synch}c}{1 - v_{\parallel}/v_{group}} \quad . \tag{5.3.2}$$

This would indicate that as the electron velocity approached the radiation group velocity, the sidebands separate further from the fundamental. This sideband shift has been experimentally observed by the Columbia FEL research group[52]. This relation works well when the dispersion is relatively small, but it breaks down as $v_{\parallel} \rightarrow v_{group}$. This is not surprising since we expanded in small Δk. As the sideband frequency gets further from fundamental this assumption breaks down.

To examine the effect of dispersion on sideband gain, Yu et al. perform an analysis where the second derivatives of the radiation field quantities are kept[51]. The radiation equations used were

$$\left(\frac{\partial a}{\partial z} + \frac{a}{v_g}\frac{\partial a}{\partial t}\right) + \boxed{\frac{1}{2k_s}\left(\frac{\partial^2\phi}{\partial z^2} - \frac{1}{c^2}\frac{\partial^2\phi}{\partial t^2}\right)} = \eta\left\langle \sin\left(\psi + \phi\right)\right\rangle \quad , \tag{5.3.3a}$$

$$a\left(\frac{\partial\phi}{\partial z} + \frac{1}{v_g}\frac{\partial\phi}{\partial t}\right) - \boxed{\frac{1}{2k_s}\left(\frac{\partial^2 a}{\partial z^2} - \frac{1}{c^2}\frac{\partial^2 a}{\partial t^2}\right)} = \eta\left\langle \cos\left(\psi + \phi\right)\right\rangle \quad , \tag{5.3.3b}$$

where the new terms have been boxed and the following terms and normalizations are used:

$$v_g = \frac{k_s c^2}{\omega_s} \quad , \quad \eta = \frac{4\pi e}{mc^2}\frac{J}{v_{\parallel}}\frac{(k_w + \delta k)\,a_w^2}{\gamma_r^3} \quad , \quad v_{\parallel} = \frac{\omega_s}{k_w + k_s} \quad , \quad a = \frac{a_s\, a_w\, \omega_s^2\left(1 + a_w^2\right)}{c^2\,\gamma_r^4} \quad ,$$

$$\gamma_r = \sqrt{\frac{\omega_s\left(1 + a_w^2\right)}{2c\left(k_w + \delta k\right)}} \quad , \text{ and } \quad \delta k = k_s - \frac{\omega_s}{c} \quad . \tag{5.3.4}$$

Other than these definitions, the terms are the same as the notation of Kroll, Morton and Rosenbluth(Chapter 2). Some cross terms have been dropped, but the equations (5.3.3) produce the identical dispersion relation as when all terms are kept.

Using the new radiation equations, a dispersion analysis was carried out to determine sideband stability and location. Some results are plotted in Figs. 5.4 and 5.5. To read these plots we have to define

$$\delta = 1 - \left(v_{\parallel}/v_g\right) \quad , \tag{5.3.5}$$

$$\text{and} \quad \bar{\phi}'_o = \frac{4\pi e}{mc^2}\frac{J}{v_{\parallel}}\frac{k_w a_w^2}{\gamma_r^3}\frac{1}{k_{synch}^3} \quad , \tag{5.3.6}$$

where δ is a measure of the dispersion and $\bar{\phi}'_o$ is a factor that can be thought of as a normalized current density. Fig. 5.4 shows that adding dispersion to the radiation equations produces quite different results in a waveguide than the usual paraxial wave equation. Fig. 5.5 shows regions of stability and instability for FEL sidebands depending only on the parameters $\bar{\phi}'_o$ and δ. Achieving $v_g = v_{\parallel}$ is not necessary to stabilize the sidebands. The analysis performed indicates that one need only come relatively close to this condition to stabilize the sidebands.

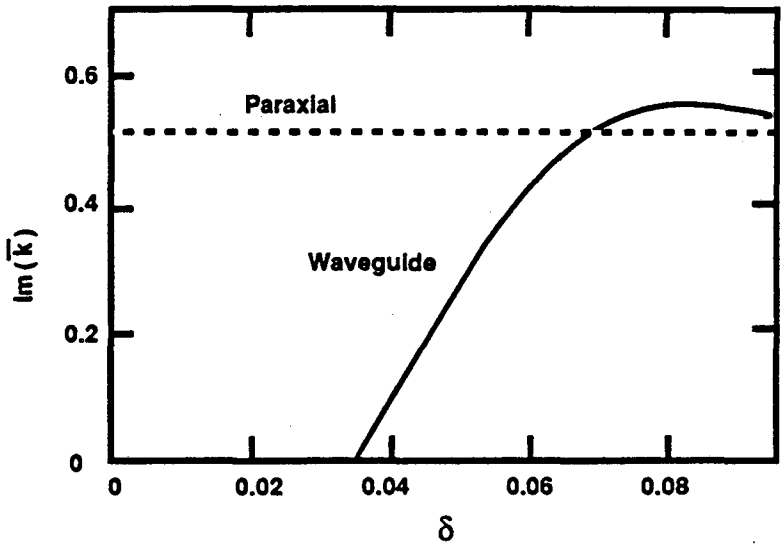

Figure 5.4(ref.52) Growth rate of the sideband instability as a function of δ for $v_g = 0.9886c$, $k/k_{synch} = 79.5$, and $\bar{\phi}'_o = 1.09$. Note that the instability disappears well before $\delta = 0$.

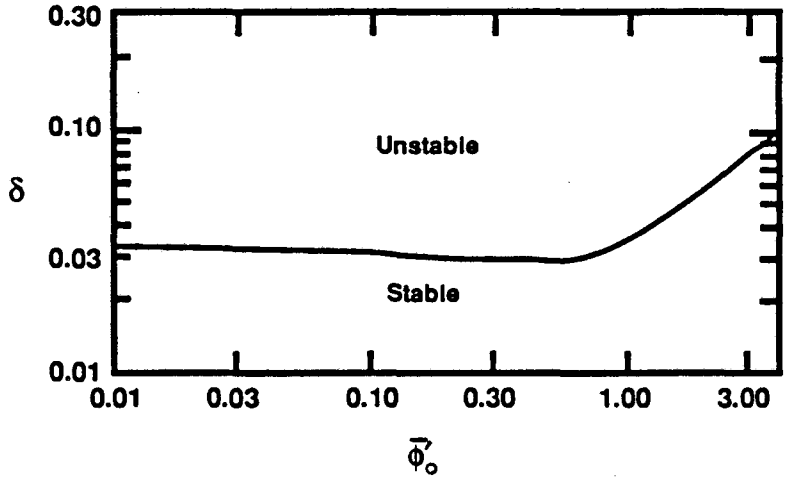

Figure 5.5(ref. 52) Regions of stability and instability for the sidebands as a function of δ and $\bar{\phi}'_o$.

While this theory provides some useful insight into the effects of dispersion on FEL sidebands, it is somewhat limited. There are some implicit assumptions of slowly varying amplitude and phase in the source terms of eqs. (5.3.3). The dispersion analysis of these equations also always give sidebands that are symmetric around the fundamental which is not always accurate. The analysis also makes it hard to produce a simple physical picture of sideband processes. A more detailed analysis is necessary and is the subject of the rest of this chapter.

5.4 Multiple Frequency Waveguide Simulation

The computer simulation described in this section was written to examine sideband generation in a highly dispersive waveguide. Instead of using a single electromagnetic wave equation with the slowly varying amplitude and phase approximation, this code calculates an amplitude and phase at each frequency it follows. In effect, instead of following a range of frequencies, the code follows many discrete frequencies. The radiation field at each frequency is moved at the correct phase velocity so that dispersion is properly included.

The radiation equations that are integrated are those shown in (3.3.26). The particle equations are just the Lorentz force equation reformulated in suitable variables. The equations are integrated with z as the independent variable so that each frequency is well defined. For convenience we rewrite the equations here. They are

$$\frac{da_{sj}^{mn}}{dz} = \mathcal{J}_j^{mn}\left[\sin\theta_{pj}^{mn} - \sin\left(\theta_{pj}^{mn} - 2k_w z\right)\right] \quad , \tag{5.4.1a}$$

$$\frac{d\phi_{sj}^{mn}}{dz} = \frac{\mathcal{J}_j^{mn}}{a_{sj}^{mn}}\left[\cos\theta_{pj}^{mn} - \cos\left(\theta_{pj}^{mn} - 2k_w z\right)\right] \quad , \tag{5.4.1b}$$

with

$$\mathcal{J}_j^{mn} = \frac{4\pi e^2}{m_e cab} a_w \lambda_{0j}^{mn} \frac{\cos\frac{m\pi}{2}\sin\frac{n\pi}{2}}{(1+\delta_{m0})} \quad . \tag{5.4.1c}$$

These are the radiation equations for each ω_j and are just those given in (3.3.26). The particle equations are

$$\frac{d\gamma_i}{dz} = \frac{a_w(z)}{\gamma_i c}\left.\frac{\partial a_x(z,t)}{\partial t}\right|_{t=t_i} , \tag{5.4.2a}$$

and

$$\frac{dt_i}{dz} = \frac{1}{c\sqrt{1 - \frac{1 + a_w^2(z)}{\gamma_i^2}}} , \tag{5.4.2b}$$

where a_w is the normalized wiggler vector potential and a_x is the normalized vector potential of the radiation field. The fields are written in this fashion to include all of the Fourier components. Explicitly we can write

$$a_x(z,t) = \sum_{m,n}\sum_{j} a_{sj}^{mn}\sin\left(k_j^{mn}z - \omega_j t + \phi_{sj}^{mn}\right) , \tag{5.4.3}$$

where we have summed over all waveguide modes and radiation frequencies.

Just as all the radiation components must be summed in the particle equations, the particle orbits must be summed so as to produce the source term for the radiation equations. The two factors that must be calculated from the particle equations are λ_{0j} and θ_{pj}. They can be calculated from eqs. (3.4.4) which we rewrite

$$\lambda_{0j}^{mn}(z)\cos\theta_{pj}^{mn} = \frac{\omega}{\pi}N_{buc}\left\langle\frac{\cos\psi_j^{mn}}{v_z\gamma}\right\rangle , \tag{5.4.4a}$$

$$\lambda_{0j}^{mn}(z)\sin\theta_{pj}^{mn} = \frac{\omega}{\pi}N_{buc}\left\langle\frac{\sin\psi_j^{mn}}{v_z\gamma}\right\rangle , \tag{5.4.4b}$$

where ψ_j^{mn} is the ponderomotive phase corresponding to the frequency ω_j, and v_z is just the inverse of the right side of (5.4.2b).

Since the equations contain the term v_z, they will show oscillations at $2k_w z$ for a linear wiggler. It is desirable to average these equations for the purpose of calculating FEL resonance and for a simpler comparison to theory. This can be performed in the same manner as the averaging done in section 2.4. Resonance can be calculated from the ponderomotive phase equation (2.4.8b) which gives

$$0 = \left(k_w + k_s + \frac{d\phi_s}{dz} \right) - \frac{\omega}{c} K_1 \quad , \tag{5.4.5}$$

with

$$K_1 = 1 + \frac{1 + \frac{1}{2} a_w^2}{2 \gamma_r^2} + \frac{3\left(1 + a_w^2 + \frac{3}{8} a_w^4 \right)}{8 \gamma_r^4} + \frac{15\left(1 + \frac{9}{8} a_w^2 + \frac{3}{2} a_w^4 + \frac{5}{16} a_w^6 \right)}{48 \gamma_r^6} + \ldots \quad . \tag{5.4.6}$$

Numerically, this can be solved to an arbitrary accuracy, however in general one only keeps a small number of terms. Because of the number of terms necessary for reasonable accuracy, and because of the Bessel functions that must be calculated, the averaged equations actually take more computer time to integrate than the unaveraged equations. The averaged equations are useful primarily as a check that the equations are consistent. Also since the form of the averaged linear wiggler equations is the same as the form of the equations for a helical wiggler, then results for one type of wiggler can be carried over to the other type with the inclusion of the proper Bessel function terms.

In order to illustrate the differences between results from the averaged and unaveraged equations, a simulation was performed where the FEL fundamental and its first two harmonics were allowed to interact with the electrons. In one simulation, the exact unaveraged equations were integrated, and in the other simulation the averaged equations using the first four terms in the expansion of v_z^{-1} were integrated.

The simulation parameters are shown in Table IV. The relativistic energy factor γ is small enough that the ratio a_w/γ is not negligible. In fact, for the parameters used, this ratio is just over 0.3. This means that at least several terms in the expansion of v_z^{-1} are necessary to achieve numerical accuracy.

The average value of γ is plotted in Fig. 5.6. The first feature to notice is the oscillations in the unaveraged simulation. These oscillations have a period of half the

Table IV Simulation parameters

Relativistic energy γ	7.2	
Wiggler peak field	3.80	kG
Wiggler wavelength	9.8	cm
Radiation frequency	34.6	GHz
Beam current	800	amps
Waveguide size	9.8 x 2.9	cm
Initial radiation power(TE^{01})	60	kW

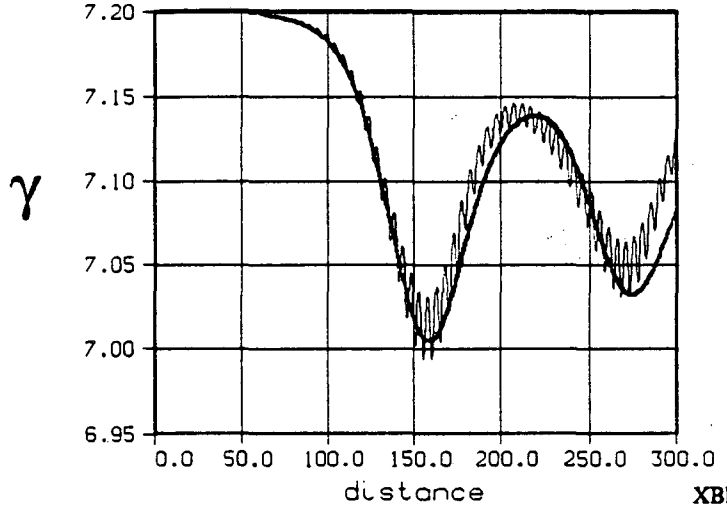

Figure 5.6 A plot of the relativistic energy factor γ verses distance. The solid black line represents the unaveraged equations. The thick gray line represents the averaged equations.

wiggler wavelength. These are directly due to the modulation of the transverse electron velocity in a linear wiggler. The averaged equations produce a curve that is close to that produced by the unaveraged equations. The fact that these curves are not exactly aligned means that more terms in the expansion of v_z^{-1} are necessary for that additional numerical accuracy. Given the highly nonlinear nature of the FEL equations, the agreement in Fig. 5.6 is actually quite good.

There are other concerns in averaging besides strict numerical accuracy. The averaging can obscure what is actually occurring. Figure 5.7 shows the 2nd harmonic radiation from the FEL simulation. Here the curve for the averaged equations follows

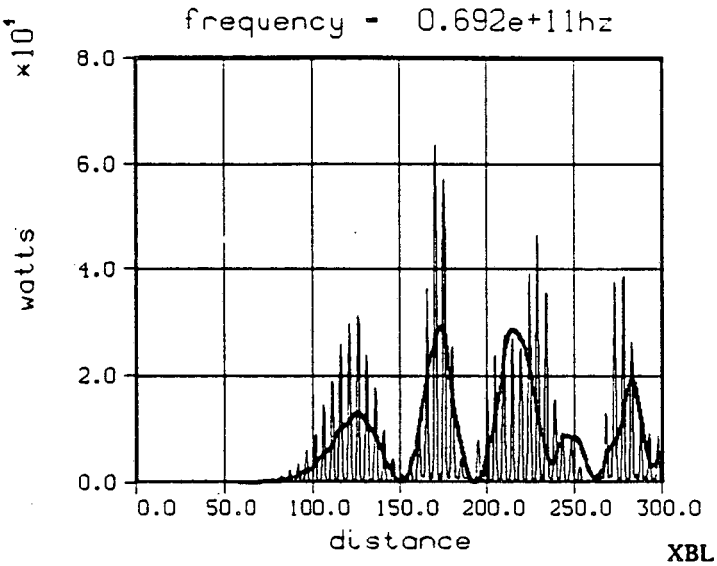

Figure 5.7 Plot of radiation power vs. distance for 2nd harmonic radiation. The black curve represents the unaveraged equations. The thick gray curve represents the averaged equations.

about where it should. However, the unaveraged curve shows additional physics. Just from looking at the curve from the averaged equations one might interpret this to show that the 2nd harmonic is amplified depending on the relative phases of its ponderomotive well and the ponderomotive well of the fundamental. While this relation might give the strength of the interaction, the fact is that any radiation emitted at the 2nd harmonic is reabsorbed by the electron beam by the time the electron beam undergoes a quarter of a wiggler oscillation. Thus we would not expect to measure any 2nd harmonic from FEL interaction. Any power at the second harmonic would be incoherent radiation produced by end fields in the wiggler. This is a different prediction than if we used only the averaged simulation.

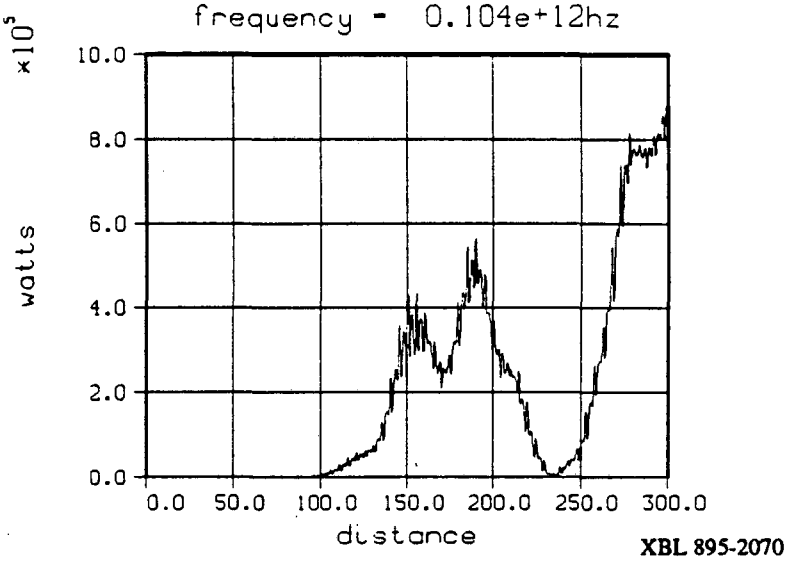

Figure 5.8 Plot of 3rd harmonic vs. distance for the unaveraged equations.

Another pitfall of averaging that we must look out for is averaging out something by accident. In Fig. 5.8 the 3rd harmonic for the unaveraged equations is plotted. The equivalent plot for the averaged equations is not shown since the values for the averaged equations are 3 orders of magnitude smaller. This enhancement of the 3rd harmonic in the unaveraged equations is due to the fact that the $2k_w z$ oscillation in v_z interacts with the $k_w z$ oscillation of the wiggler field to produce a $3k_w z$ oscillation in the radiation source term. This enhances the production of incoherent radiation at 3 times the fundamental frequency.

For some of the simulations to be performed, we will be interested in the amplification of radiation from noise. There are two possible sources of noise in a 1-D simulation. These are in the electron distribution and in ambient radiation.

The noise from the electron beam results from the fact that a realistic electron distribution will not fill phase space completely uniformly. Due to this, there will initially be a small but finite value of the Fourier component of the current at each frequency. These frequency components will lead to incoherent emission of radiation that can then be amplified by the FEL process.

There are several possible origins for incoherent radiation that can be amplified by the FEL process. Already mentioned are the nonunformities of the electron beam. There is also the incoherent radiation emitted by the electron beam from interaction with the wiggler magnetic field. Also present is shot noise from the accelerator used to produce the electron beam. The shot noise can be estimated by writing down a circuit equation for the accelerator.

Realistic estimates of the noise present in an FEL amplifier can be important in some FEL designs and this subject has been treated in detail elsewhere[53]. For the purpose of the study to be performed here, the actual levels of noise are not so important as long as we can get a reasonable measure of the FEL *gain* at the frequencies of interest. To this end we provide our 1-D simulation with the simplest reasonable way of including noise in the calculation.

Since we don't wish to include noise in the electron distribution, we must make sure that no unwanted frequencies are introduced by the initial particle loading. It is necessary to use what is known as a *quiet load*. The simplest method of loading the particles is to place them on a rectangular grid. This is adequate as long as one wishes to examine frequencies that have periods far from the particle spacing. The periodicity of the grid can be broken by offsetting the particle positions. This must be done subject to the constraint that no Fourier components be added to the distribution. In the simplest form of particle offsetting, particles must then be moved in pairs.

We will include noise only in the initial radiation spectrum and not in the initial particle distribution. Since inhomogeneities in the electron distribution result in

incoherent radiation, this is not unreasonable. In any case, any tractable computer simulation based on the equations used here would have too few particles to accurately model the noise in the distribution. In addition, the equations (5.4.1) make it necessary to have *some* initial radiation at all frequencies. This is because of the radiation amplitude in the denominator of (5.4.1b).

Since we are primarily interested only in the gain, we will assume that the initial radiation spectrum consists of white noise, i.e. the radiation power spectrum is the same at all frequencies. The particle distribution will be initialized so that all Fourier components of the current are initially zero. The radiation has an input for the power in the noise such that the initial power is spread over all frequencies to be followed in the simulation.

In Fig. 5.9, the spectra from several simulations are plotted. In these simulations, the total power in the noise spectrum was respectively 0.5, 5.0, and 50.0 watts. One can see from the log scale that each peak is 10 times the previous one. This would seem to confirm that the gain was the same in each simulation. The spectrum has a roughly parabolic shape which is what one would expect from the discussion of section 2.5.

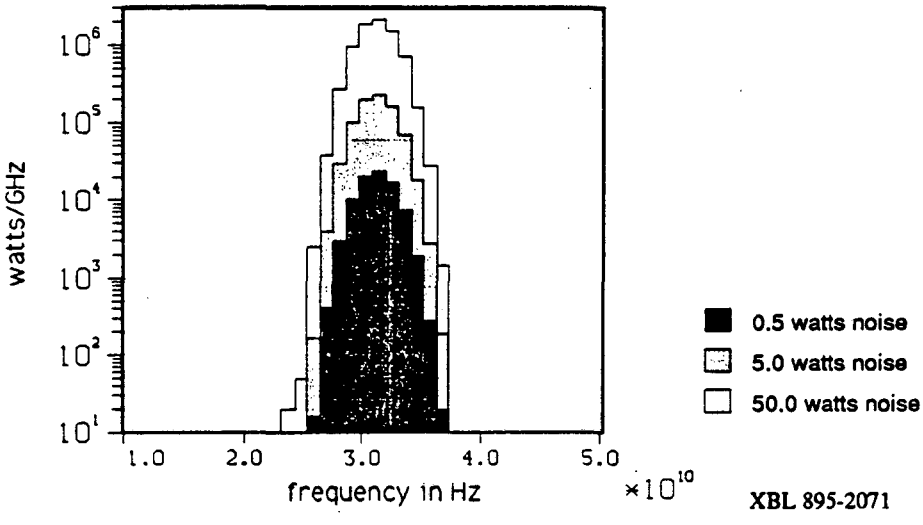

Figure 5.9 Spectra at 2 meters for various amounts of ambient electromagnetic noise.

5.5 Physics from FEL Sideband Simulations

In this section we will examine some sideband simulations to illustrate some physics from full many-particle-per-bucket simulations. We will also compare some of these results with a single particle per bucket simulation to study the validity of a single particle per bucket model.

The simulations that follow use the parameters of Table V for inputs. One simulation will be in an untapered wiggler. The second simulation will use a tapered wiggler that starts its taper at 1.4 meters and reduces the wiggler field to 55% of it's original value by the end of the wiggler. A spectrum of random noise in the radiation was used as input. It was assumed to be shot noise with a power of about 150 mW per GHz. This was about 5 watts total noise input for the frequencies followed.

Table V

Beam Energy	3.68	Mev
Beam Energy in γ	7.2	
Energy spread in γ	$\pm$ 0.5	
Beam Current	800	amperes
Wiggler wavelength	9.8	cm
Radiation frequency	34.6	GHz
Waveguide width	9.8	cm
Waveguide height	2.9	cm
Input radiation power	60	KWatts / TE^{01} mode
Wiggler Peak Field	3.80	KGauss
Particles/bucket	272	

(a)

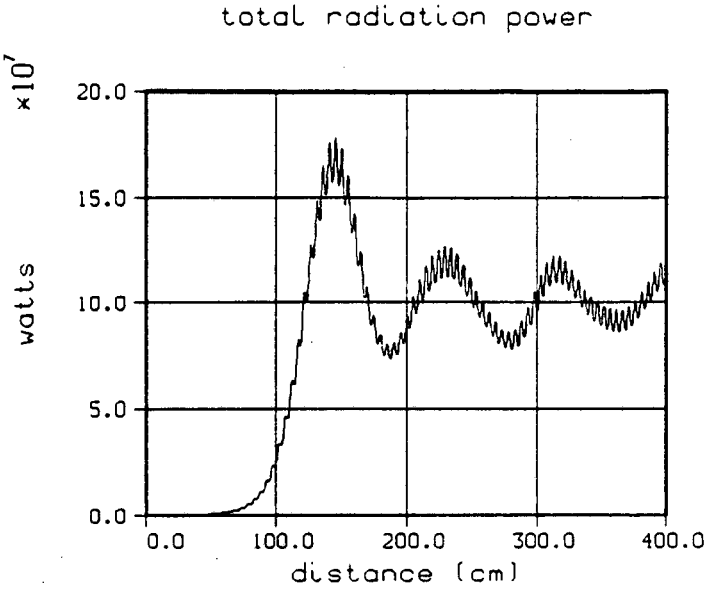

(b)

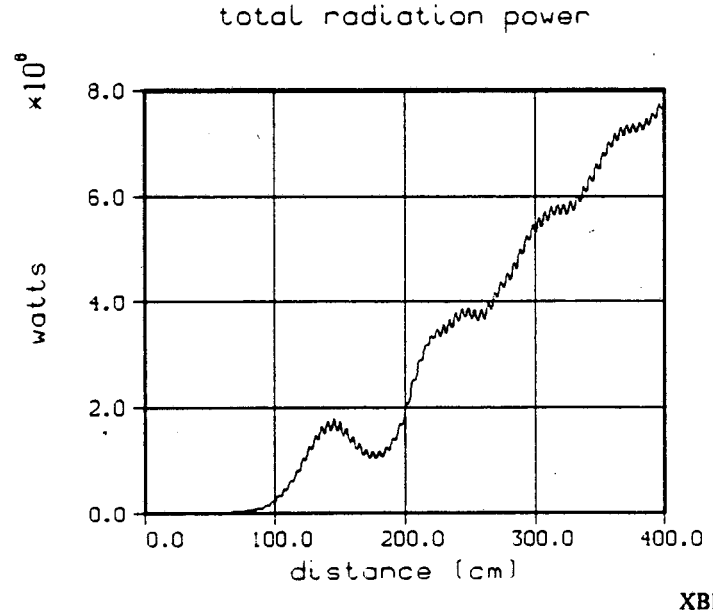

XBL 895-2072

Figure 5.10 Total radiation power vs. distance for (a) an untapered wiggler, and (b) a tapered wiggler.

(a)

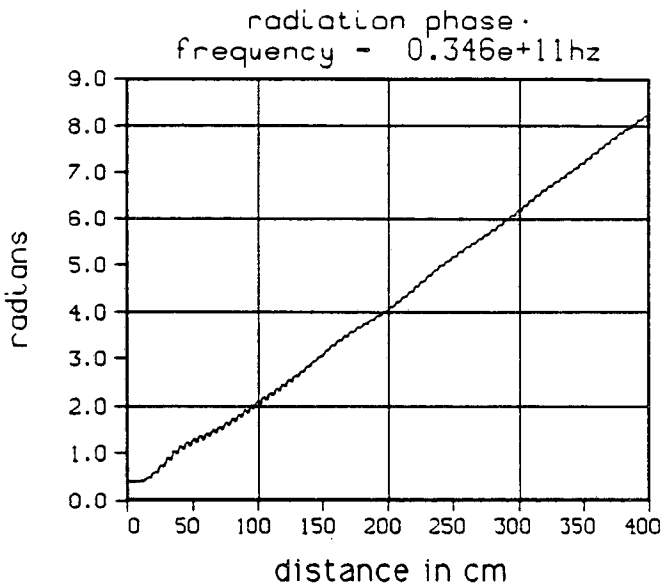

(b)

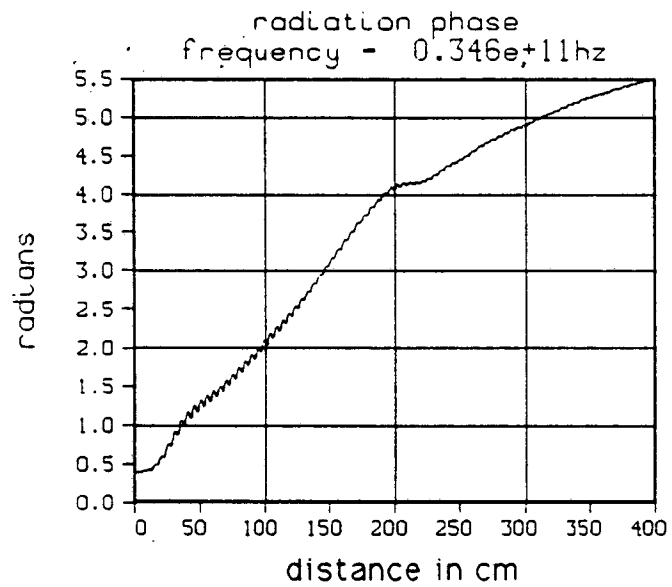

XBL 895-2073

Figure 5.11 Plot of the slow radiation phase of the fundamental FEL frequency for (a) an untapered wiggler, and (b) a tapered wiggler. The fact that the curve for the tapered wiggler changes slope soon after the tapering begins shows that particles are being detrapped from the ponderomotive well.

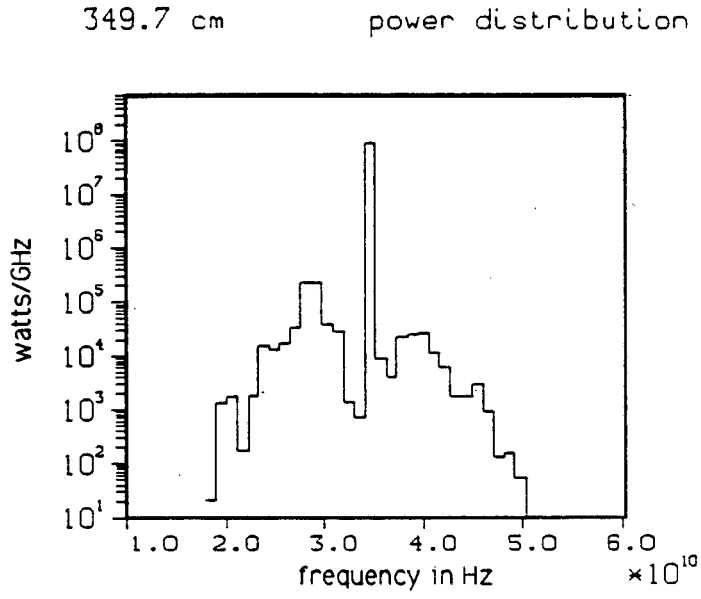

(a)

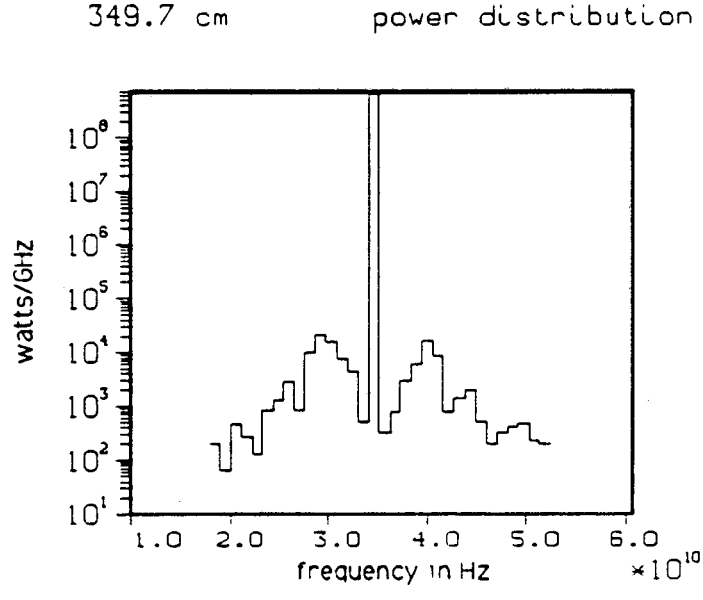

(b)

XBL 895-2074

Figure 5.12 Spectrum at 3.5 meters for (a) an untapered wiggler and (b) a tapered wiggler. The power in the sidebands in the tapered wiggler is less in magnitude than the untapered case. The sideband power is also relatively smaller, since the fundamental power is much greater in the tapered wiggler.

Fig 5.10 shows the total radiation power produced. In each simulation, the sideband power is always several orders of magnitude less than the fundamental, so this power is essentially the power in the fundamental frequency. Since this is an unaveraged 1-D simulation, the power exhibits small oscillations on the length scale of $2k_w z$. The tapered wiggler FEL produces almost an order of magnitude more power than the untapered wiggler.

Fig. 5.11 shows the slowly varying radiation phase of the fundamental frequency. Even though the simulation is unaveraged, the plot for the untapered wiggler is almost a straight line. In the plot for the tapered wiggler, the curve changes slope soon after the tapering is initiated. This is because electrons are being detrapped from the FEL bucket. As the electrons are lost, the interaction with the radiation is weaker and the slope of the curve decreases.

Fig. 5.12 shows the radiation power spectrum at 3.5 meters for both cases. The power in the sidebands for the tapered wiggler is significantly less than the power in the sidebands in the untapered case. This has several causes. First of all there was significant electron detrapping in the tapered case. By 3.5 meters only about a half of the original

electrons are still in the bucket undergoing synchrotron oscillations. Not only can substantial detrapping occur in tapered wiggler FEL's, but the bucket itself is smaller(narrower) when the wiggler is tapered. Also in a tapered wiggler FEL, the synchrotron wave number can change substantially. If the power during the tapering changes by say a factor of 10, then the synchrotron wavenumber which goes as the fourth root of the power will change by 1.8. The sideband instability depends on the coherence of the synchrotron oscillation. If this oscillation varies over distance, then sideband growth will be inhibited.

In order to demonstrate that sufficient accuracy was obtained by the computer simulation, two more untapered runs were performed. The number of particles that were used varied in each simulation. If a sufficient number of particles are used, then the results will not depend greatly on the initial conditions. Fig. 5.13 shows a comparison of the spectrum of these runs. It can be seen that the 528 and 272 particle/bucket runs give essentially the same results. The 528 particle/bucket run give slightly better resolution near the fundamental. The 144 particle/bucket run starts to show some erratic behavior since there weren't enough particles to achieve good resolution, however, the major features of the spectrum are shown reasonably clearly.

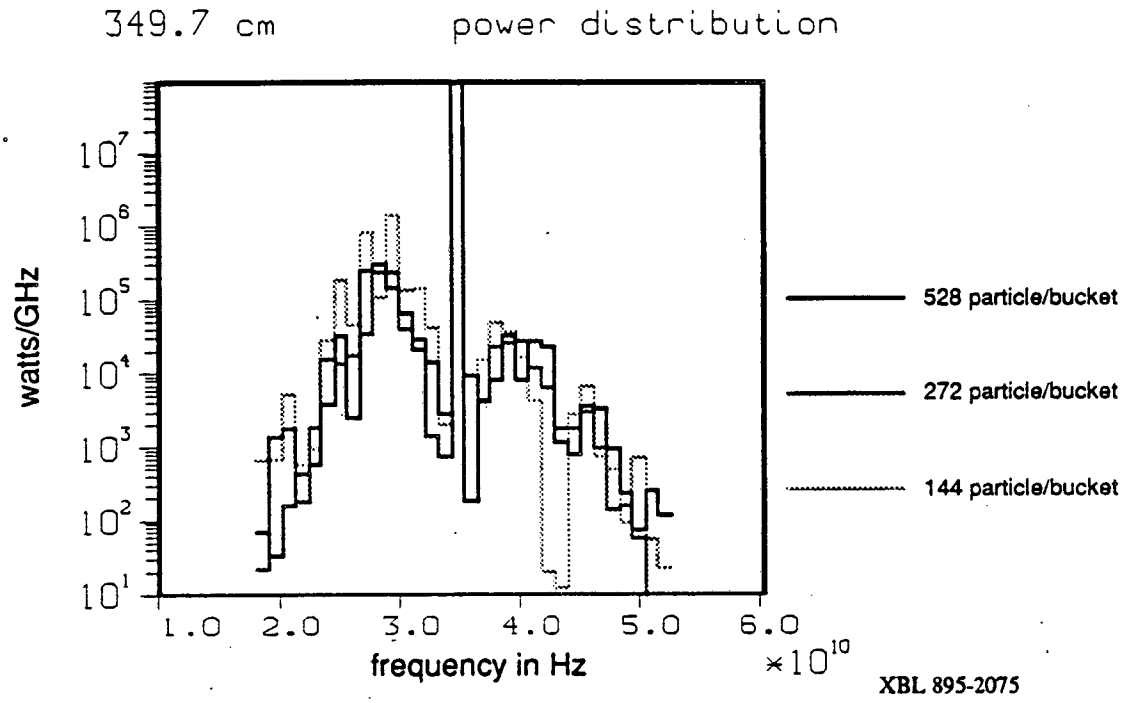

Figure 5.13 Comparison of simulations with different number of particles. The results don't depend too much on the number of particles as long as a certain threshold number are used.

The simulations shown exhibit complicated behavior. In order to reach an understanding of the physics involved, we wish to study a simpler system that can reproduce the general behavior of the full system. To do this, a version of the FEL simulation can be run that has only a single particle per bucket. This simulation can only study saturated FEL's since the single particle represents a bunch of electrons and the electrons are tightly bunched only after saturation. The equilibrium of the single particle per bucket simulation can be chosen so that the particle starts at the exact center of the

bucket, or at any other position. If the particle is not centered in the bucket, the equilibrium will display synchrotron oscillations at some chosen amplitude.

In order to understand how the single-particle-per-bucket simulation relates to the full simulation, we have to understand its limitations. First of all, its accuracy is limited to the situation where the fundamental is the dominant frequency. If any other frequency has a power on the order of the fundamental, then the FEL bucket is no longer well defined. Therefore, to study saturation effects in sidebands one must use a more complete simulation.

Another limitation is that in a realistic simulation, the bunching of the electrons is imperfect. One way this shows up is in the evolution of the slowly varying radiation phase. The single-particle-per-bucket simulation gives the maximum slope possible for that particular current, since in the many-particle-per-bucket simulation the term that drives the slow radiation phase has an average over the particles. Fig. 5.14 shows the evolution of the radiation phase in the case where the parameters are chosen to be the same as that of the untapered simulation shown earlier at saturation(Fig. 5.11a). Note that the slope is larger. This will produce a shift in the output spectrum from the many-particle-per-bucket simulation.

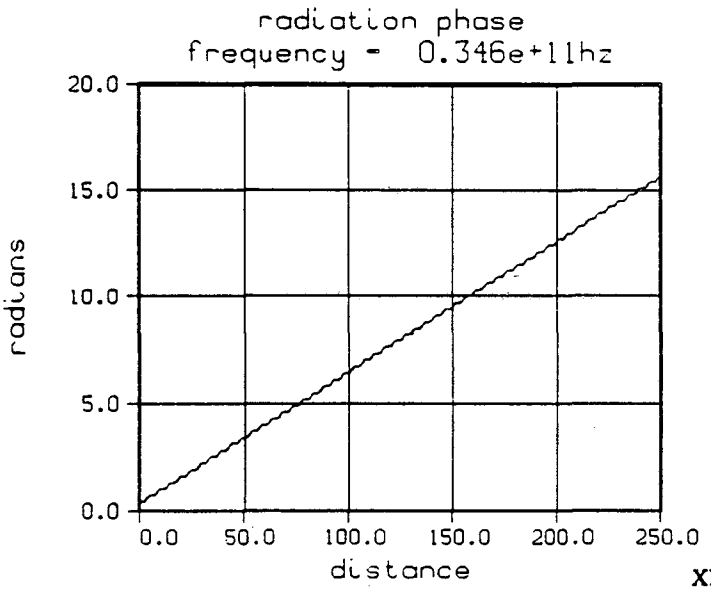

Figure 5.14 In the single-particle-per-bucket simulation, the bunching is at a maximum. Note that the slope here is larger than that of the equivalent many-particle-per-bucket simulation of Fig. 5.11a.

Also in the many-particle-per-bucket simulation, the electron distribution will be spread around the bucket. This means that different parts of the distribution will have different synchrotron wave numbers. Remember that in a pendulum, the larger the amplitude of the oscillation, the more nonlinear terms contribute and the slower the frequency gets. The many particle simulations in this section were chosen purposely to have a large energy spread so that the electron distribution fills the entire bucket. This shows clearly that large synchrotron amplitudes are not necessary to drive the sideband instability. What matters is the shape and depth of the ponderomotive well that confines the electrons.

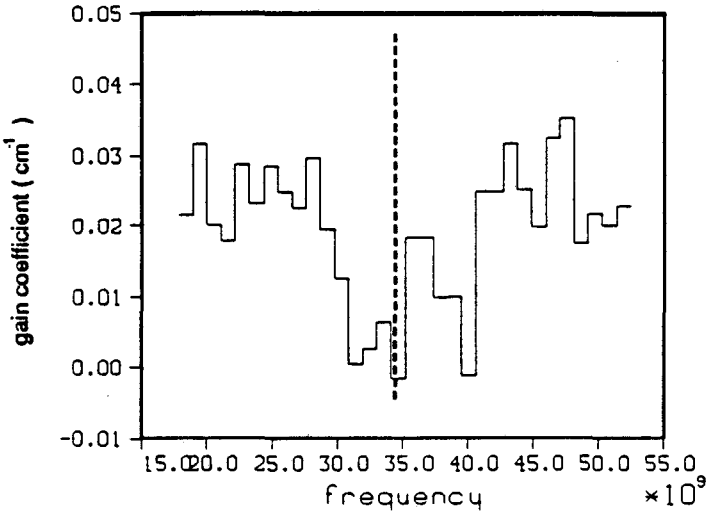

XBL 895-2077

Figure 5.15 Exponential gain coefficients calculated for the untapered many-particle-per-bucket simulation. Only the part of the plot to the left of the dashed line were a good fit to an exponential.

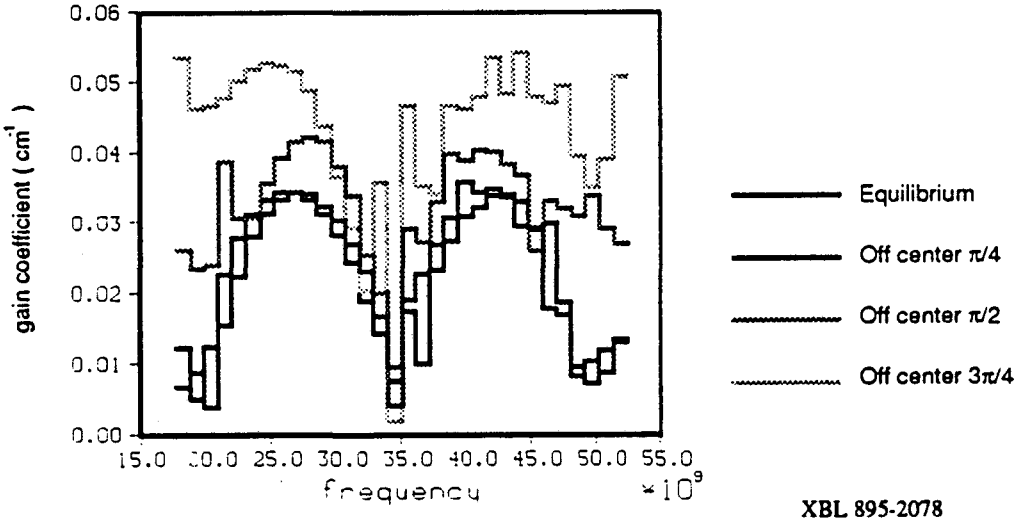

XBL 895-2078

Figure 5.16 Exponential gain coefficents calculated from the single-particle-per-bucket simulation. The different curves are for different synchrotron oscillation amplitudes. The particles are started at different phases relative to the center of the bucket. As the amplitude increases, so does the gain. As the electron approaches the edge of the bucket, its synchrotron period changes and therefore the peaks move relative to the fundamental.

To see how the two types of simulations compare, exponential gain coefficients were calculated for both. An exponential curve was fitted to the radiation amplitude at each frequency. One must always check that the result is believable, since a curve that was far from an exponential would give a spurious result. A gain curve was calculated for the many-particle-per-bucket simulation in the regime after saturation. The result is plotted in Fig. 5.15. Only the lower sideband curve was a good fit to an exponential, so we will use only that part of the curve as the basis for comparison.

In Fig. 5.16 there are gain curves for the single-particle-per-bucket simulation. All the curves here are a reasonable fit to an exponential. Each curve represents a particle with a different initial synchrotron oscillation amplitude. One can see that as the particle starts further from the center of the bucket , the spectrum of the lower sideband becomes wider and the peak moves further from the fundamental.

The spectrum for the particles that are far from the bucket center looks very much like the spectrum of the many-particles-per-bucket simulation. The gain is smaller in the many-particle-per-bucket simulation, but this is to be expected since the many competing frequencies would inhibit sideband gain. It would seem that a single-particle-per-bucket simulation would be a legitimate way to gain insight into FEL sideband physics.

5.6 FEL Sidebands as Stimulated Scattering

In this section, it is demonstrated that sideband generation in FEL's is a process completely analogous to stimulated scattering. The upper and lower sidebands correspond respectively to the anti-Stokes and Stokes waves in a stimulated scattering process. For a more detailed discussion of stimulated scattering processes see refs. [54] and [55].

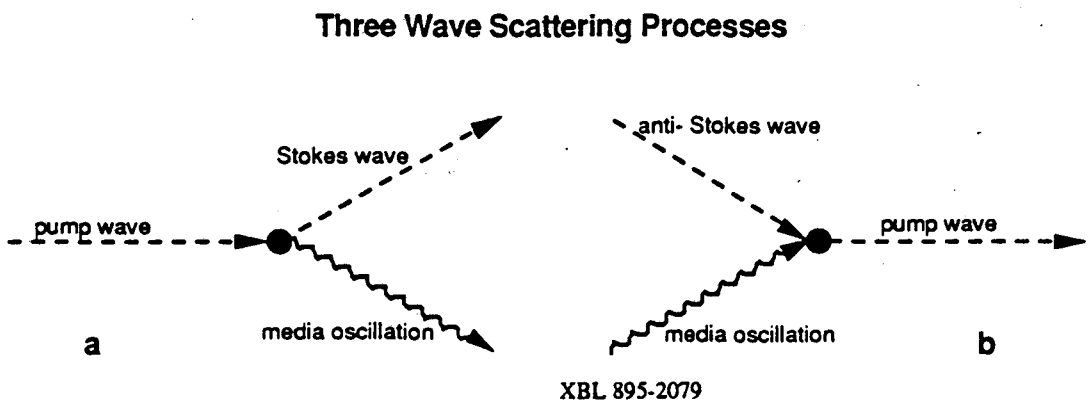

Figure 5.17 Three-wave scattering processes. (a) is the Stokes scattering case where an initial pump wave scatters into a Stokes wave and an oscillation in the scattering medium. (b) is the anti-Stokes case where an anti-Stokes wave and an oscillation in the scattering medium combine to create the pump wave.

To start let's describe the types of stimulated scattering processes we will be examining. Fig. 5.17 shows the possible three-wave scattering processes. By media oscillation, we mean any oscillation or wave that can interact with the radiation. These could be molecular vibrations in a gas, phonons in a crystal, plasma oscillations, sound

waves or quantum levels in an atom. The case of Stokes scattering is always possible in such a medium. However, for anti-Stokes scattering, there must be some energy already present in the media oscillation, or in other words the medium must have a finite temperature or a nonthermal excitation. These processes must conserve energy and momentum. This means that in most systems the Stokes wave is a backscattered wave.

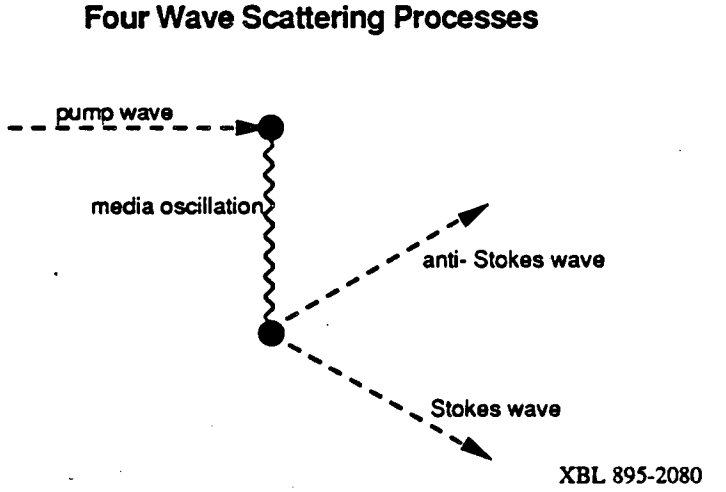

Figure 5.18 Four-wave scattering process. The pump wave scatters into a Stokes and anti-Stokes wave through a "virtual" media oscillation.

Another scattering process important to our discussion is a four-wave process. Here the pump wave scatters into a Stokes and an anti-Stokes wave. The media oscillation is a vital part of this process, but on balance no energy or momentum are transferred to the medium. It is then possible to create an anti-Stokes wave in a "cold" medium in a four-wave process.

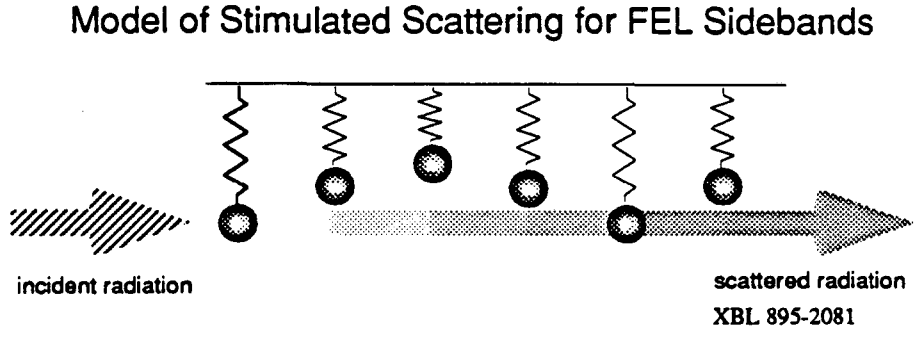

Figure 5.19 Electron bunches in the ponderomotive well performing synchrotron oscillations can be modeled as charged harmonic oscillators. The radiation scatters into lower sidebands(Stokes wave) and upper sidebands(anti-Stokes wave).

In an FEL, sidebands are seen only when the electron beam is tightly bunched and the fields at the fundamental frequency are rather large. For the purposes of modeling sideband growth we will assume that the electron bunch can be represented by a single macroparticle with equivalent mass and charge. Our system then begins to look like Fig. 5.19 where the electrons oscillate in a harmonic oscillator potential that is driven by the FEL radiation. The radiation is scattered by this interaction into upper and lower sidebands. In a three-wave interaction, the lower sideband(Stokes wave) can grow when there is no initial synchrotron oscillation in the electrons. If there is some synchrotron oscillation initially, then scattering to the upper sideband(anti-Stokes wave) is allowed and the sideband will grow at the expense of the synchrotron oscillation. For the case where there is no initial synchrotron oscillation, the upper sideband can only grow in a four-wave process.

To demonstrate that sideband generation in FEL's is just stimulated scattering, computer simulations were performed with a single macroparticle per FEL bucket to model the electron bunch. The simulation parameters are almost identical to those in Table I, except that the input power is 200 Mwatts.

The plots in Fig. 5.20 are simulations where there was no initial synchrotron oscillation. These plots demonstrate just what one expects for stimulated scattering in a cold medium for a three-wave process. In Fig. 5.19a only the lower half of the spectrum is allowed to grow in the simulation. Since we expect this to be the Stokes wave, there

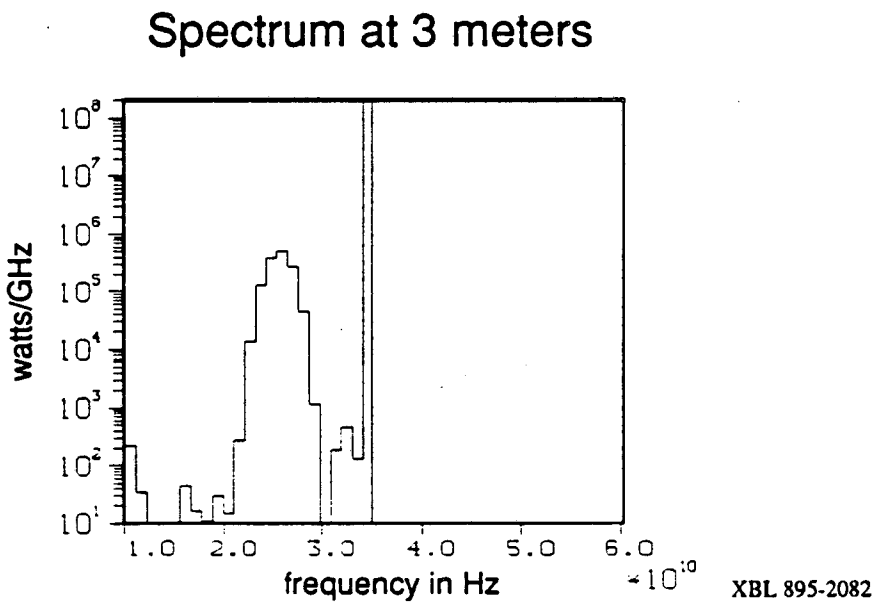

Figure 5.20a When only the lower sideband is allowed to grow, there is substantial gain. This is consistant with Stokes scattering in a three-wave process.

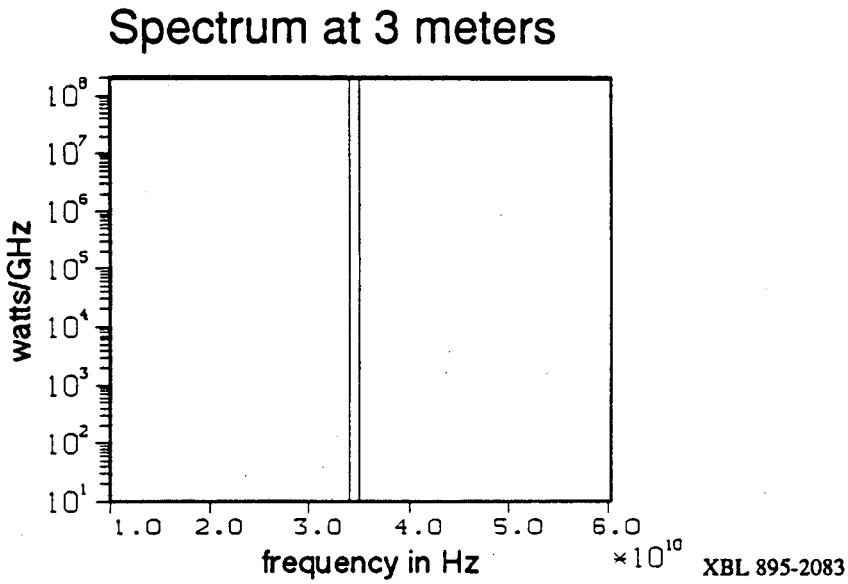

Figure 5.20b When only the upper sideband is allowed to grow, there is no gain at all. This is consistant with anti-Stokes scattering in a three-wave process.

should be plenty of sideband growth, which is what one observes. In Fig. 5.20b only the upper half of the spectrum is allowed to grow. We would expect that there would be no growth for these initial conditions and that is in fact what one observes.

In the case where there is an initial synchrotron oscillation, the upper sideband can grow. In Figs. 5.21 and 5.22, the simulation is started with a large synchrotron oscillation, but otherwise the inputs are the same as for the simulations in Fig. 5.20. One can see that there is growth in the upper sideband spectrum. As the upper sideband grows, the synchrotron oscillation is damped out. This is also consistent with our picture of stimulated scattering.

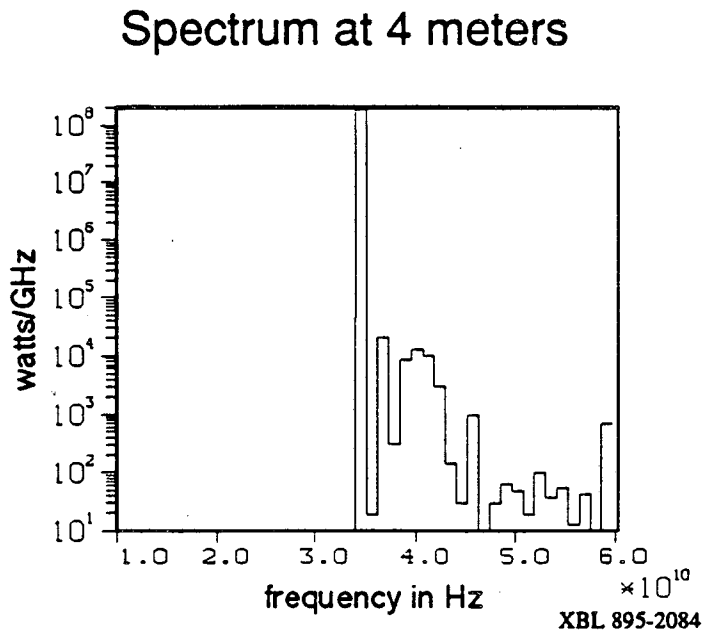

Figure 5.21 When there is some initial synchtrotron oscillation, the upper sideband can grow in a three-wave process.

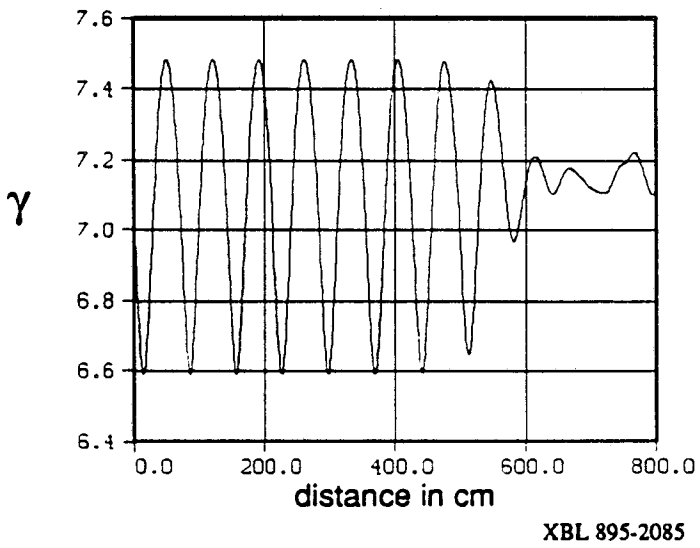

Figure 5.22 In a three-wave process, the upper sideband (anti-Stokes wave) must grow at the expense of the synchtrotron oscillation.

If we now allow both upper and lower sidebands, i.e. four-wave processes are now possible, then it is possible to get upper sideband growth when there is no initial synchrotron oscillation. Fig. 5.23 contains a simulation that illustrates that this is in fact what occurs.

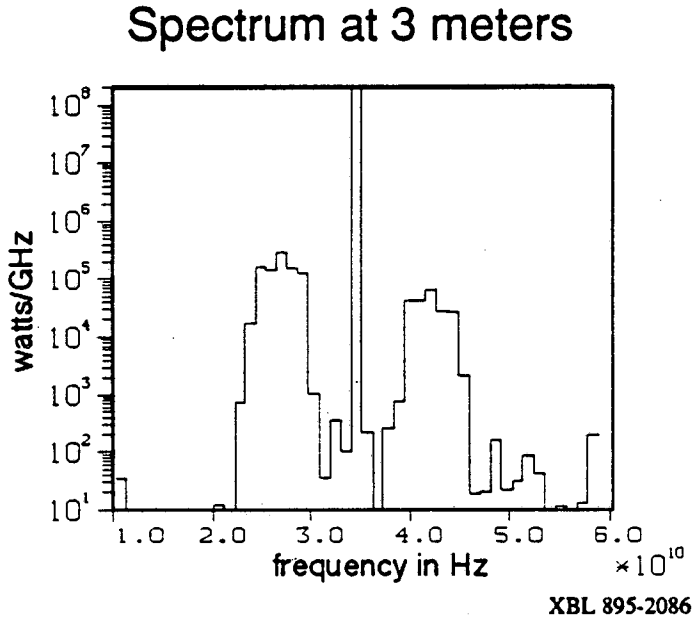

Figure 5.23 In a four-wave process, both upper and lower sidebands can grow when there is no initial synchrotron oscillation.

It can be seen that FEL sidebands exhibit all the expected behavior of a stimulated scattering process. Thus the formal methods for calculating gain that are used in nonlinear optics should be directly applicable to FEL sidebands. In section 5.7, a set of coupled wave equations are derived and expressions for sideband gain are calculated and compared to the single-particle-per-bucket computer simulation.

5.7 FEL Sideband Dispersion Analysis

In this section we will derive the dispersion relation for sideband gain in an FEL. The methodology that will be used closely parallels that of parametric amplification in nonlinear optics. Here our nonlinear medium is the bunched electron beam. We will derive a wave equation for each radiation frequency. The different frequencies will couple to each other through the electron beam whose motion will be described by a modified pendulum equation. The advantage to this type of analysis is that the equations for free space and for a waveguide are identical. The physics of sidebands in a waveguide can be understood by examining the phase matching conditions determined by the set of equations.

From chapter 3 we can write a 1-D wave equation for each radiation mode in a waveguide. Rewriting eqs. (3.2.4),(3.2.5), and (3.2.6) gives

$$\left[\frac{\partial^2}{\partial z^2} - \frac{\partial^2}{c^2\partial t^2} - \gamma_t^{mn2}\right] A_x^{mn}(z,t) = -\frac{2}{c} J_x^{mn}(z,t) \quad , \tag{5.7.1}$$

where

$$\gamma_t^{mn2} = \frac{m^2\pi^2}{a^2} + \frac{n^2\pi^2}{b^2} \quad , \tag{5.7.2}$$

$$J_x^{mn}(z,t) = \frac{8\pi}{ab(1+\delta_{m0})} \int_0^a dx \int_0^b dy \cos\frac{m\pi x}{a} \sin\frac{n\pi y}{b} J_x(x,t) \quad . \tag{5.7.3}$$

If we wished to do a plane wave analysis in free space we would just set $\gamma_t^{mn} = 0$, and set $J_x^{mn}(z,t)=2\pi J_x(z,t)$. The form of the wave equation is therefore the same. Since we are primarily interested in FEL's in waveguides we will keep all the waveguide notation. For convenience we will drop the waveguide superscripts m and n since the analysis is valid for a single waveguide mode.

We can now write A_x and J_x as a Fourier series to obtain

$$\left[\frac{\partial^2}{\partial z^2} + \left(\frac{\omega_n^2}{c^2} - \gamma_t^2\right)\right] a_{\omega n}(z) = -\frac{2e}{m_e c^3} J_{\omega n}(z) \quad , \tag{5.7.4}$$

where we have normalized the vector potential by $e/m_e c^2$, and where n is a subscript that labels a particular frequency. Explicitly $J_{\omega n}$ is

$$J_{\omega n}(z) = \frac{\omega_0}{2\pi} \int_0^{2\pi/\omega_0} dt\, J_x(z,t)\, e^{-i\omega_n t} \quad , \tag{5.7.5}$$

where we have defined a periodic interval with angular frequency ω_0. If we follow a section of beam with N_{buc} FEL buckets and if ω_s represents the fundamental FEL frequency, then $\omega_0 = N_{buc}\omega_s$. This period does not enter the final answer and so in principle can be as large as necessary to achieve any arbitrary frequency resolution. The periodic boundary conditions are used to make the calculation as close to the computer

simulation as possible, but the same answers can be achieved with a continuous Fourier transform. We can write the current density as

$$J_x(z,t) = \frac{e}{a_B}\sum_{\ell} \delta(z - z_\ell(t))v_{x\ell}(z) \quad , \tag{5.7.6}$$

where ℓ is the index for each particle and a_B is either the beam cross sectional area in free space, or a filling factor in a waveguide that is given by

$$\frac{1}{a_B} = \frac{4}{ab}\frac{\cos\frac{m\pi}{2}\sin\frac{n\pi}{2}}{\left(1+\delta_{m0}\right)} \quad , \tag{5.7.7}$$

where once more a and b are respectively the x and y dimensions of the waveguide and m and n represent the waveguide modes. We can now write $J_{\omega n}$ explicitly as

$$J_{\omega n}(z,t) = -\omega_0 \frac{e}{a_B}\sum_{\ell} \frac{v_{x\ell}(z)}{v_{z\ell}(z)} e^{-i\,\omega_n t_\ell(z)} \quad , \tag{5.7.8}$$

Since we are assuming that the particle motion is determined to zeroth order by the ponderomotive well formed by the wiggler field and the fundamental radiation frequency, it will be convenient to change variables. From chapter 2 we know that we can write the ponderomotive phase as $\psi = (k_w + k_s)z - \omega_s t + \phi_s(z)$, where k_w is the wiggler wave number, k_s is the radiation wave number for a vacuum filled waveguide, and ϕ_s is the slowly varying phase from the radiation interaction with the electron beam. We can solve for t in terms of ψ, but to be consistent with the many bucket model we cannot restrict ψ to be between $-\pi$ and π. We will write $\psi = 2\pi p_\ell + \psi'$, where p_ℓ is an integer giving the

bucket index and ψ' is between $-\pi$ and π. The expression for $J_{\omega n}$ can now be written

$$J_{\omega n}(z,\psi) = - \omega_0 \frac{e}{a_B} e^{-i(\omega_n/\omega_s)\left[(k_w + k_s) z + \phi_s(z)\right]} \sum_{\ell} \frac{v_{x\ell}(z)}{v_{z\ell}(z)} e^{i(\omega_n/\omega_s)\psi'_\ell} e^{-i(\omega_n/\omega_s)2\pi p_\ell} \quad , \quad (5.7.9)$$

where once more ℓ is a particle index. From eq. (2.2.8) we know we can write

$$v_{x\ell}(z) = \frac{c a_{w0}(z)}{\gamma_\ell} \sin k_w z \quad , \quad (5.7.10)$$

where a_{w0} is the amplitude of the dimensionless wiggler vector potential. We will also reexpress $v_{z\ell}$ as $c\beta_{z\ell}$. At this point we will also assume that γ_ℓ and $\beta_{z\ell}$ are essentially the same for all the particles. This is very nearly true and it will allow us to express the current entirely in terms of ψ_ℓ' and z. So dropping the ℓ's on γ and β_z we obtain

$$J_{\omega n}(z,\psi) \cong - \omega_0 \frac{e}{a_B} \frac{a_{w0}}{\gamma\beta_z} \sin(k_w z)\, e^{-i(\omega_n/\omega_s)\left[(k_w + k_s) z + \phi_s(z)\right]} \sum_{\ell} e^{i(\omega_n/\omega_s)\psi'_\ell} e^{-i(\omega_n/\omega_s)2\pi p_\ell} \quad . \quad (5.7.11)$$

Since we are deriving equations for a linear wiggler, we expect from section 2.4 to have terms in the current that vary from each other by factors that go as a sine or cosine of $2k_w z$. To average (5.7.11) over this length scale, we will first write the $\sin k_w z$ term in complex form. Then in analogy with the averaging procedure of section 2.4 we will write

$$\psi'_\ell = \psi_{0\ell} + \psi_2 \sin(2k_w z) \quad , \quad (5.7.12)$$

and

$$\frac{1}{\beta_z} \cong K_1 - K_2 \cos 2k_w z \quad , \quad (5.7.13)$$

where

$$K_1 = 1 + \frac{1 + \frac{1}{2}a_w^2}{2\gamma^2} + \frac{3\left(1 + a_w^2 + \frac{3}{8}a_w^4\right)}{8\gamma^4} + \frac{15\left(1 + \frac{9}{8}a_w^2 + \frac{3}{2}a_w^4 + \frac{5}{16}a_w^6\right)}{48\gamma^6} + \ldots \quad , \qquad (5.7.14a)$$

and

$$K_2 = \frac{a_w^2}{4\gamma^2} + \frac{3\left(a_w^2 + \frac{1}{2}a_w^4\right)}{8\gamma^4} + \frac{15\left(\frac{3}{2}a_w^2 + \frac{3}{2}a_w^4 + \frac{15}{32}a_w^6\right)}{48\gamma^6} + \ldots \quad . \qquad (5.7.14b)$$

The factors of (5.7.11) that we wish to average can then be written

$$F_{ave}^n = \left\langle (K_1 - K_2 \cos 2k_w z)\left(1 - e^{-i2k_w z}\right) e^{-i(\omega_n/\omega_s)\psi_2 \sin 2k_w z} \right\rangle_{\text{avg over } z} \quad . \qquad (5.7.15)$$

If we express the exponentials in terms of sines and cosines, we can use the identities

$$\sin(r \sin\theta) = 2 \sum_{n=0}^{+\infty} J_{2n+1}(r) \sin((2n+1)\theta) \quad , \qquad (5.7.16a)$$

$$\cos(r \sin\theta) = J_0(r) + 2 \sum_{n=0}^{+\infty} J_{2n}(r) \cos(2n\theta) \quad , \qquad (5.7.16b)$$

where the J's represent Bessel functions. We will keep only leading terms so the average becomes

$$F_{ave}^n = K_1\left(J_0\left[\frac{\omega_n K_2}{2ck_w}\right] - J_1\left[\frac{\omega_n K_2}{2ck_w}\right]\right) + \frac{K_2}{2} J_0\left[\frac{\omega_n K_2}{2ck_w}\right] \quad . \qquad (5.7.17)$$

The Fourier component of the current $J_{\omega n}$ can now be written

$$J_{\omega n}(z,\psi) \equiv -\omega_0 \frac{e}{a_B} \frac{a_{w0}}{\gamma} F_{ave}^n \frac{e^{ik_w z}}{2i} e^{-i(\omega_n/\omega_s)\left[(k_w + k_s) z + \phi_s(z)\right]} \sum_{\ell} e^{i(\omega_n/\omega_s)\psi_{0\ell}} e^{-i(\omega_n/\omega_s)2\pi p_\ell} \quad . \qquad (5.7.18)$$

We need to make one more approximation before the radiation equation is in a suitable form for the subsequent analysis. Since the particles are considered to be deeply trapped in the bucket we will assume that $\psi_{0\ell} << 1$. We can now expand the exponential containing $\psi_{0\ell}$. The first term of the expansion is 1 and since $\sum_{\ell} e^{-i(\omega_n/\omega_s)2\pi p_\ell} = 0$, this term can be ignored. It can be seen that the sum adds to zero by remembering that ω_s and ω_n are frequencies defined in a Fourier series of the current. As long as $\omega_s \neq \omega_n$, this sum vanishes. The next term in the expansion will just pull out the argument of the exponential. We can then write

$$J_{\omega n}(z,\psi) \cong -\frac{\omega_0}{2}\frac{e}{a_B}\frac{\omega_n}{\omega_s}\frac{a_{w0}}{\gamma} F^n_{ave} e^{ik_w z}\, e^{-i(\omega_n/\omega_s)\left[(k_w+k_s)z+\phi_s(z)\right]} \sum_{\ell} \psi_{0\ell} e^{-i(\omega_n/\omega_s)2\pi p_\ell} \quad ,(5.7.19)$$

We now wish to derive an equation of motion for ψ in terms of the radiation fields. If we start with a more general form for the radiation field vector potential

$$a_x(z,t) = a_{s0}\sin\left(k_s z - \omega_s t + \phi_s\right) + \sum_{n\neq s} a_{n0}\sin\left(k_n z - \omega_n t + \phi_n(z)\right) \quad , \qquad (5.7.20)$$

then in a derivation following section 2.2, the particle equations of motion can be written

$$\frac{d\gamma}{dz} = -\frac{\omega_s a_s a_w}{2c\ \gamma}\left[\sin\psi + \sum_{n\neq s}\frac{\omega_n a_n}{\omega_s a_s}\sin\psi_n\right] \quad , \qquad (5.7.21a)$$

and $$\frac{d\psi}{dz} = k_w + k_s - \frac{\omega_s}{c} + \frac{d\phi_s}{dz} - \frac{\omega_s}{2c\gamma^2}\left[1+\frac{a_w^2}{2}\right] \quad . \qquad (5.7.21b)$$

The factor ψ_n is the ponderomotive phase determined by the nth radiation component. We

wish to rewrite this in terms of the ponderomotive well of the fundamental since by assumption, the field at the fundamental is much larger than at any other frequency. ψ_n can be written as

$$\psi_n = (k_w + k_n)\, z - \omega_n t \quad , \tag{5.7.22a}$$

$$= (k_w + k_n)\, z - \frac{\omega_n}{\omega_s}\left[(k_w + k_s)\, z + \frac{d\phi_s}{dz}\right] + \frac{\omega_n}{\omega_s}\psi \quad . \tag{5.7.22b}$$

By taking the derivative of (5.7.21b) and substituting in (5.7.21a) we can derive a modified pendulum equation. This becomes

$$\frac{d^2\psi}{dz^2} + k_\sigma^2 \sin\psi = -k_\sigma^2 \sum_{n\neq s} \frac{\omega_n a_{0n}}{\omega_s a_{0s}} \sin\left(\theta_n(z) - \frac{\omega_n}{\omega_s}\psi\right) \quad , \tag{5.7.23}$$

where $\theta_n(z) = (k_w + k_n)\, z - \frac{\omega_n}{\omega_s}\left[(k_w + k_s)\, z + \phi_s(z)\right]$, and k_σ is the synchrotron wave number and is given by

$$k_\sigma^2 = \frac{\omega_s^2\, a_{w0}\, a_{s0}\left(1 + a_{w0}^2\right)}{2c^2\,\gamma^4} \quad . \tag{5.7.24}$$

If we had used the low γ equations of section 2.4 to start, the form of (5.7.23) would be identical. The synchrotron wave number k_σ, however, would have a different form. Since we are assuming that $a_n << a_s$, then we can treat the right side of (5.7.23) as a perturbation.

To use this equation we have to relate it to the radiation equation. Using (5.7.20) and the fact that $a_{\omega n}$ is a Fourier coefficient for the radiation field we have

$$a_x(z,t) = \sum_{n=0}^{\infty} a_{n0}\sin\left(k_n z - \omega_n t + \phi_n(z)\right) = \sum_{n=-\infty}^{\infty} a_{\omega n}\, e^{i\omega_n t} \quad , \tag{5.7.25}$$

where we now identify $a_{\omega n} = \frac{i}{2} a_{0n}\, e^{-i\left(k_n z + \phi_n(z)\right)}$. If we write $\psi = 2\pi p_\ell + \psi'$, and assume that $\psi' << 1$ in order to expand the exponentials, and if everything is written in complex form, then we have

$$\frac{d^2\psi'_\ell}{dz^2} + k_\sigma^2 \sin\psi'_\ell = k_\sigma^2 \sum_{n\neq s} \frac{\omega_n a_{\omega n}}{\omega_s a_{0s}}\, e^{-ik_n z}$$
$$\times\left\{\left[e^{i\left(\theta_n(z) + (\omega_n/\omega_s)2\pi p_\ell\right)} - \text{C.C.}\right] + \left[e^{i\left(\theta_n(z) + (\omega_n/\omega_s)2\pi p_\ell\right)} + \text{C.C.}\right]\frac{\omega_n}{\omega_s}\psi'_\ell\right\}. \tag{5.7.26}$$

Here we have ignored the factor ϕ_n compared to $k_n z$. This is also equivalent to absorbing the exponential of ϕ_n into the factor $a_{\omega n}$. This equation plus the radiation equation

$$\frac{\partial^2 a_{\omega n}}{\partial z^2} + \left(\frac{\omega_n^2}{c^2} - \gamma_t^2\right) a_{\omega n} =$$
$$-\omega_0 \frac{e}{a_B}\frac{\omega_n}{\omega_s}\frac{a_{w0}}{\gamma} F_{ave}^n e^{ik_w z}\, e^{-i\left(\omega_n/\omega_s\right)\left[\left(k_w + k_s\right)z + \phi_n(z)\right]} \sum_\ell \psi'_\ell e^{-i\left(\omega_n/\omega_s\right)2\pi p_\ell} \quad , \tag{5.7.27}$$

provide the basis for all subsequent calculations. The total derivative in the ψ' equation can be written as a partial derivative since the ponderomotive phase is comoving with the electrons which we have assumed are deeply trapped in the ponderomotive well. Thus the system is identical to that of coupled harmonic oscillators.

To see which frequencies will couple with each other we need to change the form of eqs. (5.7.26) and (5.7.27). We will separate out a fast phase that we will write out explicitly, and a slow phase which will be calculated in the subsequent dispersion analysis. We will write the fast phases as $a_{\omega n} = \tilde{a}_{0n}\, e^{-ik_n z}$, and $\psi'_\ell = \tilde{\psi}_{0\ell} e^{ik_\sigma z} + \tilde{\psi}^*_{0\ell} e^{-ik_\sigma z}$, where the * denotes complex conjugate. The trick is now to match combinations of the fast phases to see which terms have strong interactions. Rewriting the particle equation gives

$$\left[\frac{\partial^2\tilde{\psi}_{0\ell}}{\partial z^2} + 2ik_\sigma\frac{\partial\tilde{\psi}_{0\ell}}{\partial z}\right]e^{ik_\sigma z} + \left[\frac{\partial^2\tilde{\psi}^*_{0\ell}}{\partial z^2} - 2ik_\sigma\frac{\partial\tilde{\psi}^*_{0\ell}}{\partial z}\right]e^{-ik_\sigma z} = \frac{k_\sigma^2}{\omega_s a_{s0}}$$
$$\times\left\{\omega_n\tilde{a}_{0n}\left[e^{i(k_n z + \theta_n(z) + (\omega_n/\omega_s)2\pi p_\ell)} - \text{C.C.}\right] + \right.$$
$$\left. i\frac{\omega_n^2}{\omega_s}\tilde{a}_{0n}\left[e^{i(k_n z + \theta_n(z) + (\omega_n/\omega_s)2\pi p_\ell)} + \text{C.C.}\right]\left(\tilde{\psi}_{0\ell}e^{ik_\sigma z} + \tilde{\psi}^*_{0\ell}e^{-ik_\sigma z}\right)\right\}. \quad (5.7.28)$$

Remembering the definition of θ_n, we now define the following phase factors

$$\Delta k_u = k_w + k_n - \frac{\omega_n}{\omega_s}\left[(k_w + k_s) + \frac{d\phi_s}{dz}\right] + k_\sigma \ , \quad (5.7.29a)$$

$$\Delta k_L = k_w + k_n - \frac{\omega_n}{\omega_s}\left[(k_w + k_s) + \frac{d\phi_s}{dz}\right] - k_\sigma \ , \quad (5.7.29b)$$

$$\Delta k_{2u} = k_w + k_n - \frac{\omega_n}{\omega_s}\left[(k_w + k_s) + \frac{d\phi_s}{dz}\right] + 2k_\sigma \ , \quad (5.7.29c)$$

$$\Delta k_{2L} = k_w + k_n - \frac{\omega_n}{\omega_s}\left[(k_w + k_s) + \frac{d\phi_s}{dz}\right] - 2k_\sigma \ . \quad (5.7.29d)$$

$\Delta k_u = 0$ defines a frequency ω_u and similarly the zeros of the other phases define different frequencies. A set of coupled equations can be derived by setting each phase in (5.7.29) equal to zero and matching nonoscillating terms. The particle equations can be written as

$$\frac{\partial^2\tilde{\psi}_{0\ell}}{\partial z^2} + 2ik_\sigma\frac{\partial\tilde{\psi}_{0\ell}}{\partial z} = k_\sigma^2\left\{\frac{\omega_L\tilde{a}_{0L}}{\omega_s a_{s0}}e^{i\Delta k_L z}e^{i(\omega_L/\omega_s)2\pi p_\ell} - \frac{\omega_u\tilde{a}_{0u}}{\omega_s a_{s0}}e^{-i\Delta k_u z}e^{-i(\omega_u/\omega_s)2\pi p_\ell}\right.$$
$$\left. + i\tilde{\psi}^*_{0\ell}\left[\frac{\omega_{2L}\tilde{a}_{20L}}{\omega_s a_{s0}}e^{i\Delta k_{2L}z}e^{i(\omega_{2L}/\omega_s)2\pi p_\ell} + \frac{\omega_{2u}\tilde{a}_{20u}}{\omega_s a_{s0}}e^{-i\Delta k_{2u}z}e^{-i(\omega_{2u}/\omega_s)2\pi p_\ell}\right]\right\}, \quad (5.7.30a)$$

$$\frac{\partial^2\tilde{\psi}^*_{0\ell}}{\partial z^2} - 2ik_\sigma\frac{\partial\tilde{\psi}^*_{0\ell}}{\partial z} = k_\sigma^2\left\{\frac{\omega_u\tilde{a}_{0u}}{\omega_s a_{s0}}e^{i\Delta k_u z}e^{i(\omega_u/\omega_s)2\pi p_\ell} - \frac{\omega_L\tilde{a}_{0L}}{\omega_s a_{s0}}e^{-i\Delta k_L z}e^{-i(\omega_L/\omega_s)2\pi p_\ell}\right.$$
$$\left. + i\tilde{\psi}_{0\ell}\left[\frac{\omega_{2u}\tilde{a}_{20u}}{\omega_s a_{s0}}e^{i\Delta k_{2u}z}e^{i(\omega_{2u}/\omega_s)2\pi p_\ell} + \frac{\omega_{2L}\tilde{a}_{20L}}{\omega_s a_{s0}}e^{-i\Delta k_{2L}z}e^{-i(\omega_{2L}/\omega_s)2\pi p_\ell}\right]\right\}. \quad (5.7.30b)$$

Similar manipulations on the radiation equation will produce

$$\frac{\partial^2\tilde{a}_{0u}}{\partial z^2} - 2ik_u\frac{\partial\tilde{a}_{0u}}{\partial z} = \frac{e^2}{m_e c^3}\frac{a_{w0}}{a_B\gamma}F^u_{ave}\frac{\omega_u}{N_{buc}}\sum_\ell\tilde{\psi}_{0\ell}e^{i\Delta k_u z}e^{i(\omega_u/\omega_s)2\pi p_\ell}, \quad (5.7.31a)$$

$$\frac{\partial^2\tilde{a}_{0L}}{\partial z^2} - 2ik_L\frac{\partial\tilde{a}_{0L}}{\partial z} = \frac{e^2}{m_e c^3}\frac{a_{w0}}{a_B\gamma}F^L_{ave}\frac{\omega_u}{N_{buc}}\sum_\ell\tilde{\psi}^*_{0\ell}e^{i\Delta k_L z}e^{i(\omega_L/\omega_s)2\pi p_\ell}, \quad (5.7.31b)$$

where we have used $\omega_0 = N_{buc}\omega_s$.

The coupled equations (5.7.30) and (5.7.31) provide a basis for the study of FEL sidebands. For now we will ignore the 2u and 2L terms in (5.7.30) and the radiation equations we could derive for them. This will leave us with a system of four waves described by a_{s0}, the fundamental, $\tilde{\psi}_{0\ell}$, the synchrotron oscillation, and $\tilde{a}_{0u}$ and $\tilde{a}_{0L}$, respectively the upper and lower sidebands. We can make this identification of the upper and lower sidebands by examining the phase conditions (5.7.29). For free space these conditions imply

$$\Delta k_u = 0 \implies \omega_u = \omega_s\left(1 + \frac{k_\sigma}{k_w}\right), \quad (5.7.32a)$$

$$\text{and} \quad \Delta k_L = 0 \implies \omega_L = \omega_s\left(1 - \frac{k_\sigma}{k_w}\right) . \tag{5.7.32b}$$

These turn out to be identical to the sideband location predicted in previous analyses. However, if we use the waveguide dispersion relation in the phase matching condition, we get more complicated formulas. Explicitly

$$\Delta k_u = 0 \implies \omega_u = \frac{(k_w + k_\sigma)v_p}{\left[1 - \frac{v_p^2}{c^2}\right]} \left\{ 1 \pm \sqrt{\frac{v_p^2}{c^2} - \frac{\gamma_t^2}{(k_w + k_\sigma)^2}\left[1 - \frac{v_p^2}{c^2}\right]} \right\} \quad ,(5.7.33a)$$

and

$$\Delta k_L = 0 \implies \omega_L = \frac{(k_w - k_\sigma)v_p}{\left[1 - \frac{v_p^2}{c^2}\right]} \left\{ 1 \pm \sqrt{\frac{v_p^2}{c^2} - \frac{\gamma_t^2}{(k_w - k_\sigma)^2}\left[1 - \frac{v_p^2}{c^2}\right]} \right\} \quad , (5.7.33b)$$

where v_p is the phase velocity of the ponderomotive well defined by the fundamental frequency and the wiggler field. Explicitly

$$v_p = \frac{\omega_s}{\left(k_w + k_s + \frac{d\phi_s}{dz}\right)} . \tag{5.7.34}$$

Note that there is a $\pm$ in the expression for the frequency of the sidebands. In a waveguide there can be two frequencies that have the same phase velocity. Therefore there can be two lower sidebands and two "upper" sidebands. Upper is in quotes since one of the solutions for $\Delta k_u = 0$ lies below the fundamental frequency. There will not necessarily be amplification at all of these frequencies, but in the next section it will be shown that at least in the lower sideband spectrum, two peaks can be produced.

To avoid confusion with the terminology of upper and lower sidebands we will refer to the waves defined by $\Delta k_L = 0$ as the upper and lower Stokes waves, and the waves defined by $\Delta k_u = 0$ as the upper and lower anti-Stokes waves. Since the lower anti-Stokes wave actually lies below the fundamental, it is somewhat misleading to call it an "upper" sideband.

If phase matching is impossible, there may be circumstances where Δk is small enough to produce amplification. Phase matching is impossible if the relation inside the square root in (5.7.33a) or (5.7.33b) is negative. In that case we expect gain to be a maximum where Δk is at a minimum. The maximum gain, if there is any, is therefore at

$$\omega_n = \frac{c\gamma_t}{\sqrt{1 - \frac{v_p^2}{c^2}}} \quad , \tag{5.7.35}$$

where v_p is as defined in (5.7.34). Note that k_σ does not come into this relation. The gain in these circumstances will be small at best.

5.8 Three-Wave Analysis

In our three-wave analysis we will assume that the FEL fundamental, or pump wave, is not depleted at all during the interaction. Thus we can take a_{s0} and $\frac{d\phi_s}{dz}$ as constants. Therefore only two equations are required. For Stokes wave gain we need the equations with $\tilde{a}_{0L}$(5.7.31b), and $\tilde{\psi}^*_{0\ell}$(5.7.30b). We will substitute $\tilde{a}_{0L} = \bar{a}_{0L}\, e^{\rho_1 z}$, and $\tilde{\psi}^*_{0\ell} = \overline{\psi}^*_{0\ell}\, e^{\rho_2 z}$, where the ρ's are complex. The resulting equations are

$$\left(\rho_1^2 - 2ik_L\rho_1\right)\bar{a}_{0L}e^{\rho_1 z} = \frac{e^2}{m_e c^3}\frac{a_{w0}}{a_B\gamma}F^L_{ave}\frac{\omega_L}{N_{buc}}\sum_\ell \overline{\psi}^*_{0\ell}\, e^{\rho_2 z}e^{i\Delta k_L z}e^{i(\omega_L/\omega_s)2\pi p_\ell} \quad , \qquad (5.8.1a)$$

$$\text{and} \quad \left(\rho_2^2 - 2ik_\sigma\rho_2\right)\overline{\psi}^*_{0\ell}e^{\rho_2 z} = -\,k_\sigma^2\frac{\omega_L}{\omega_s a_{s0}}\bar{a}_{0L}\, e^{\rho_1 z}e^{-i\Delta k_L z}e^{-i(\omega_L/\omega_s)2\pi p_\ell} \quad . \qquad (5.8.1b)$$

The equations (5.8.1) imply that $\rho_1 = \rho_2 + i\Delta k_L$. Eliminating the coefficients $\bar{a}_{0L}$, and $\overline{\psi}^*_{0\ell}$ will produce an equation for ρ_1. The terms that go as $e^{\pm i(\omega_L/\omega_s)2\pi p_\ell}$ will cancel leaving a factor of $\sum_\ell 1$. This is a sum over all particles and may be replaced by $N_{buc}n_{bunch}$, where N_{buc} is the number of buckets and n_{bunch} is the number of particles per bucket. We can also write n_{bunch} as $n_{bunch} = \frac{I}{e}\frac{2\pi}{\omega_s}$. The fourth order equation for ρ_1 then becomes

$$\rho_1^4 - 2i(k_L + \Delta k_L + k_\sigma)\rho_1^3 -$$

$$\left(\Delta k_L^2 + 2k_\sigma\Delta k_L + 4k_L\Delta k_L + 4k_Lk_\sigma\right)\rho_1^2 + 2ik_L\left(\Delta k_L^2 + 2k_\sigma\Delta k_L\right)\rho_1 + F = 0 \quad , \qquad (5.8.2)$$

where in free space

$$F = \frac{2\pi e}{m_e c^3} \frac{a_{w0}}{a_{s0}} \frac{k_\sigma^2}{\gamma} F_{ave}^L \frac{\omega_L^2}{\omega_s^2} J_{tot} \quad , \tag{5.8.3}$$

J_{tot} being the electron beam current density. In a waveguide

$$F = \frac{8\pi Ie}{abm_e c^3} \frac{\cos\frac{m\pi}{2} \sin\frac{n\pi}{2}}{(1+\delta_{m0})} \frac{a_{w0}}{a_{s0}} \frac{k_\sigma^2}{\gamma} F_{ave}^L \frac{\omega_L^2}{\omega_s^2} \quad , \tag{5.8.4}$$

where I is the total beam current, m and n are waveguide indices, and a and b are waveguide dimensions.

Using the same procedure, a dispersion relation can be derived for the anti-Stokes wave. The result is

$$\rho_1^4 - 2i(k_L + \Delta k_L - k_\sigma)\rho_1^3 -$$

$$(\Delta k_L^2 - 2k_\sigma \Delta k_L + 4k_L \Delta k_L - 4k_L k_\sigma)\rho_1^2 + 2ik_L(\Delta k_L^2 - 2k_\sigma \Delta k_L)\rho_1 + F = 0 \quad , \tag{5.8.5}$$

where the term F_{ave}^L in F has been replaced by F_{ave}^u, and ω_L has been replaced by ω_u.

Note that the choice of ρ_1 a real root means exponential growth or damping. Since the complex factor i only appears for odd powers of ρ_1, the dispersion equation can be written with all real coefficients by writing $\rho_1 = i\rho'_1$. This implies that real roots of ρ_1 come in pairs of positive and negative roots. We will now compare roots calculated numerically from the dispersion relations (5.8.2) and (5.8.5), with roots calculated from a single particle per bucket computer simulation.

TABLE VI

			Waveguide		
			x dimension	y dimension	Wiggler peak field
Beam energy in γ	7.2		4.74 cm	6.00 cm	4.00 kG
Radiation frequency	34.6	GHz	9.80 cm	2.90 cm	3.80 kG
Wiggler wavelength	9.8	cm	11.37 cm	2.50 cm	3.70 kG
Beam current	800	amps	14.21 cm	2.00 cm	3.46 kG
Input radiation power	200	MW			
Waveguide mode	TE^{01}				

Table VI shows the input parameters to the simulations. Each simulation started with a particle in the center of each FEL bucket. Four waveguide cases were used with varying amounts of dispersion. All were chosen so that the total waveguide cross sectional area was the same in each case. In order to get a comparison for only a three-wave process it is desirable to suppress all four-wave interactions. This is achieved by only allowing one half of the spectrum in the simulation. Either the upper or lower sideband spectrum is allowed to grow.

For the anti-Stokes wave, both simulation and dispersion analysis show no sideband gain. Only the Stokes wave shows gain and therefore the plots in this section are only for the lower sideband.

The simulation calculates a gain coefficient by fitting an exponential curve to the radiation fields at each frequency followed. Thus a curve that was far from an

exponential would give spurious results. This had to be checked in each case. The factors a_{wo},k_s and ϕ_s used in the dispersion analysis are those calculated by the simulation.

Figs. 5.24 show a comparison of the simulation results and the dispersion analysis in the case where the slowly varying phase ϕ_s of the fundamental was ignored. There is relatively good agreement for the larger waveguide heights, although there is a frequency shift. As the waveguide height decreases and therefore as the dispersion increases, there is less accurate agreement. This is partly because of the fact that as the dispersion increases the results are increasingly sensitive to the inputs. The largest cause of the discrepancies, however, is that we need to include the slow radiation phase of the fundamental in the dispersion analysis. When this is done, the agreement between simulation and theory is quite good.

Fig. 5.25 shows the real part of the gain for each frequency. Fig. 5.26 shows the imaginary part of the gain or the slow radiation phase for each frequency. In the dispersion calculation, the imaginary part of the gain was plotted only when the real part was nonzero. This was to make certain that the correct root was chosen.

(a)

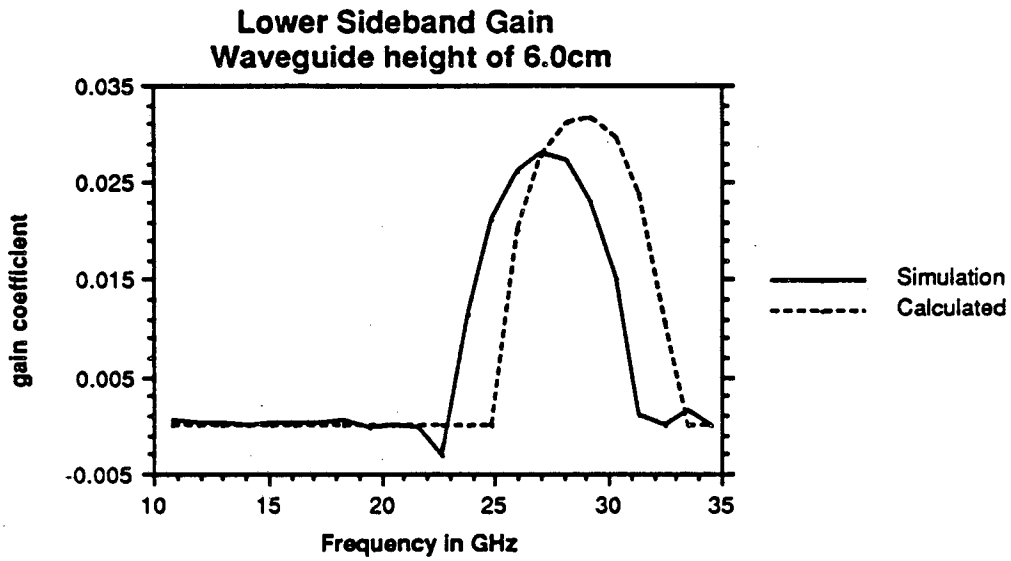

(b)

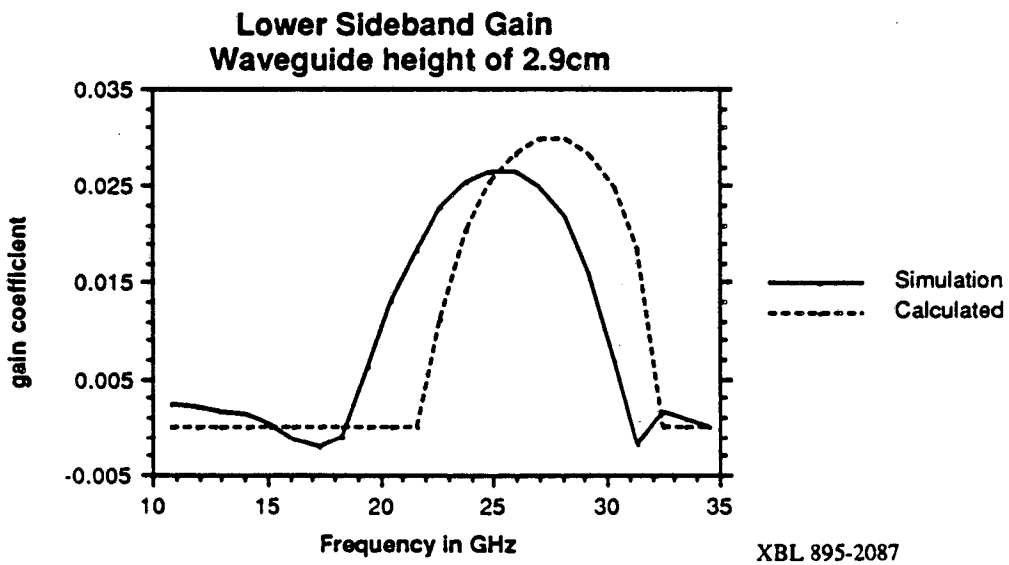

XBL 895-2087

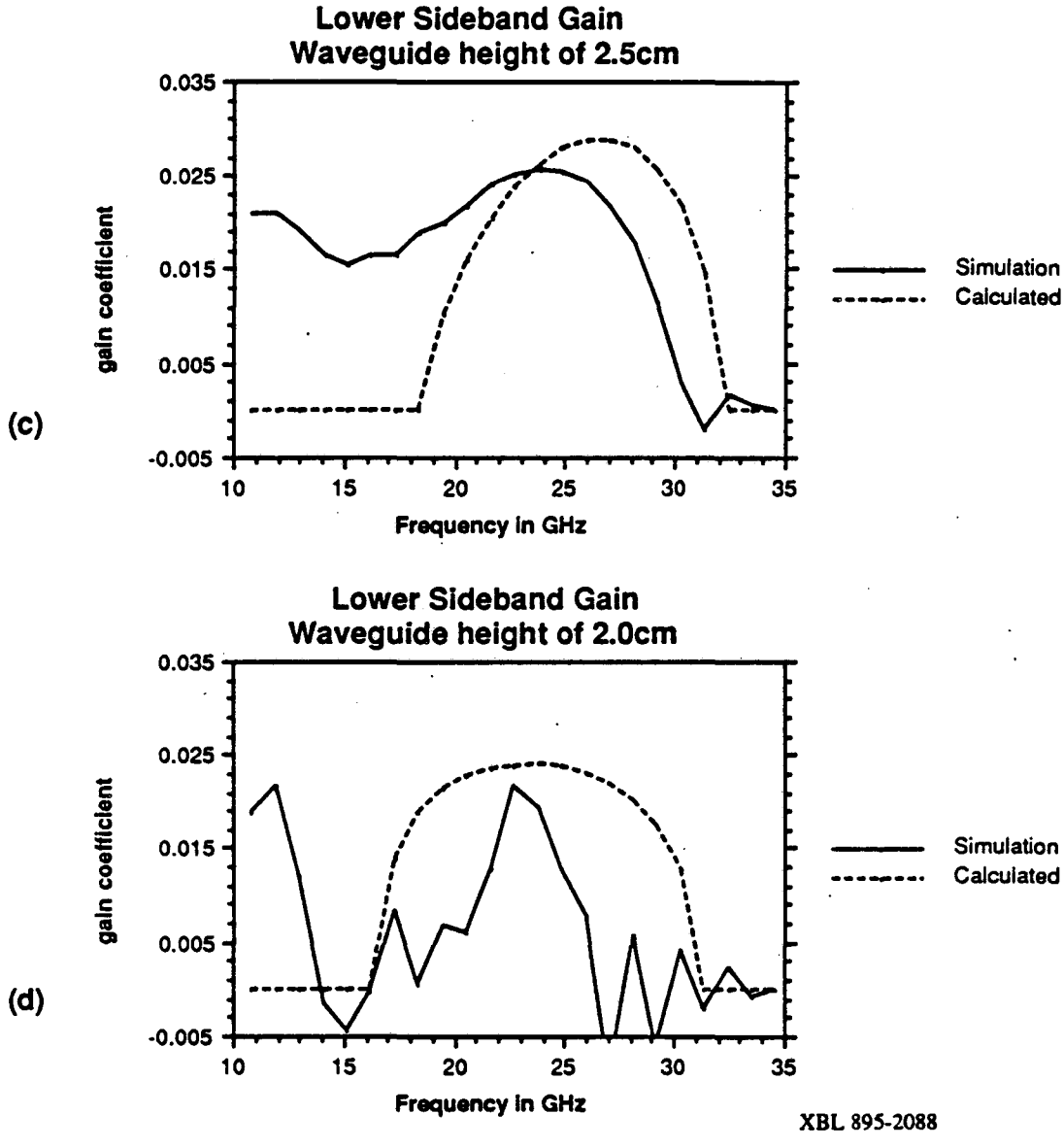

Figure 5.24 Comparisons of simulation and theory. The slow radiation phase ϕ_s was ignored in the dispersion calculation, but is automatically included in the simulation. Note that the gain curves are relatively close in (a) and (b) except for the frequency shift. In (c) there is a substantial discrepancy between the curves although the size and location of the right hand peak is about right. The simulation exhibits two lower sideband peaks, the leftmost just barely visible before the plot goes offscale. In (d) there is also a discrepancy between the curves although the size and location of the peaks are about right. As the waveguide height decreases, the dispersion increases and small variations in input parameters can have a large effect.

(a)

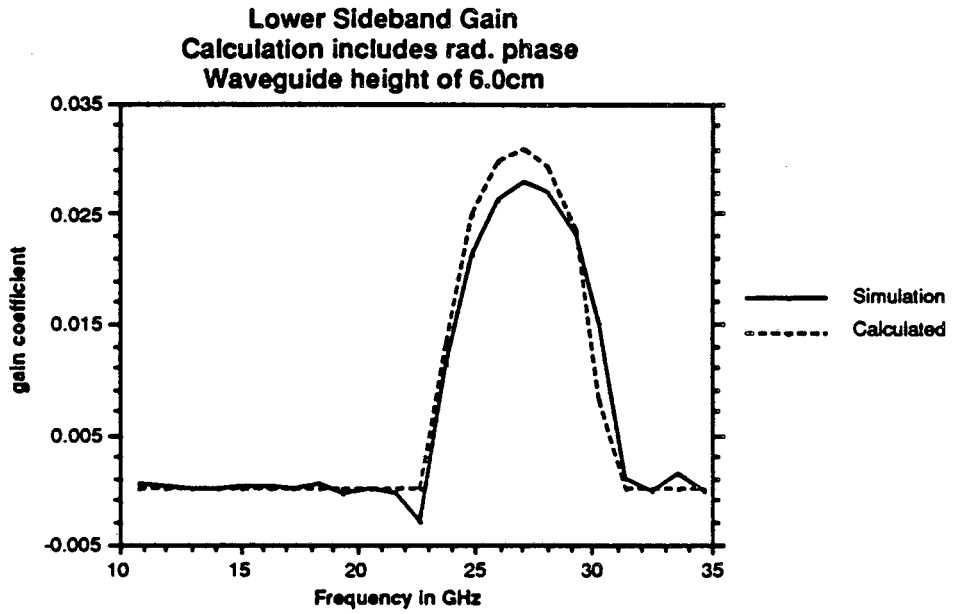

(b)

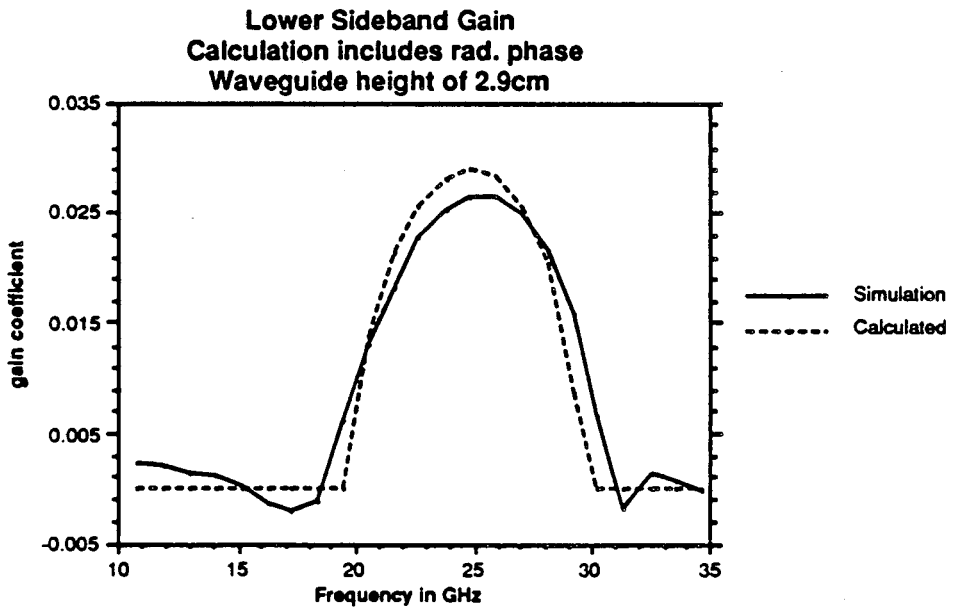

XBL 895-2089

(c)

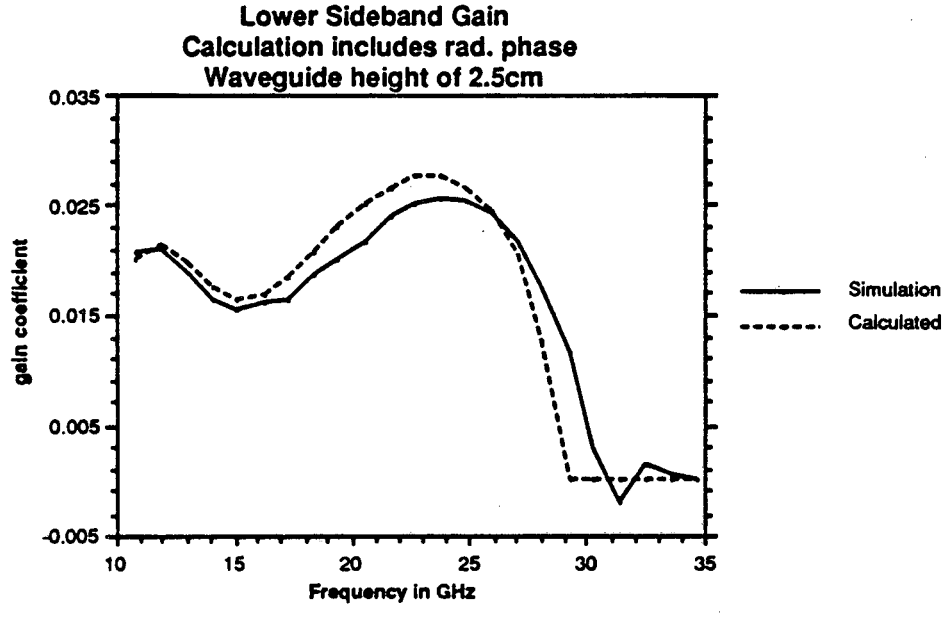

(d)

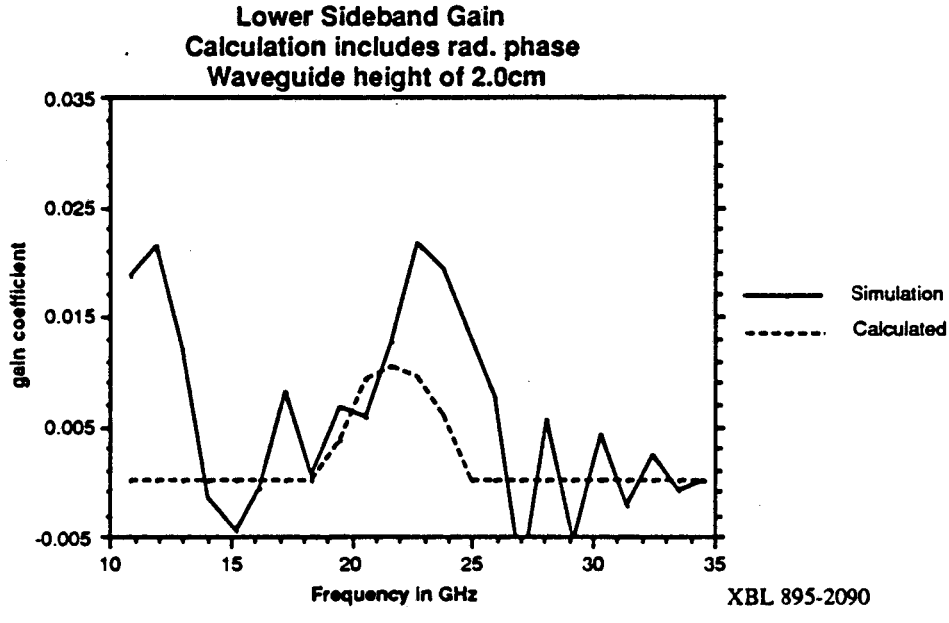

XBL 895-2090

Figure 5.25 When the slowly varying phase of the fundamental is added to the dispersion analysis, there is rather good agreement with the simulation. Note the double sideband peak in (c). This shows both upper and lower Stokes waves. In (d) there is only rough agreement between the dispersion analysis and the simulation. Not only are the results of the dispersion analysis more sensitive to inputs, but the raggedness of the simulation curves suggest that the computer had a hard time fitting the data. The simulation curves may not have been such good exponentials.

(a)

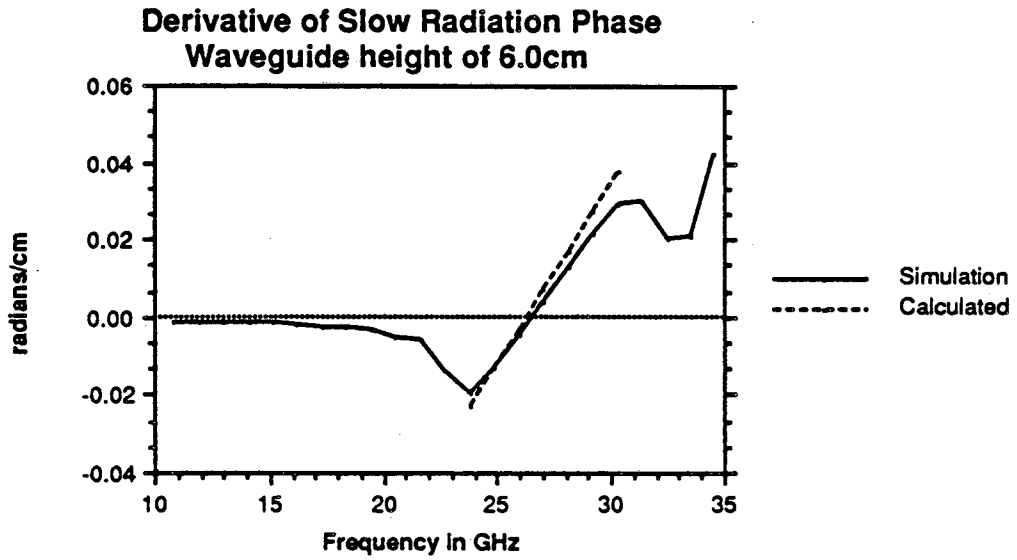

(b)

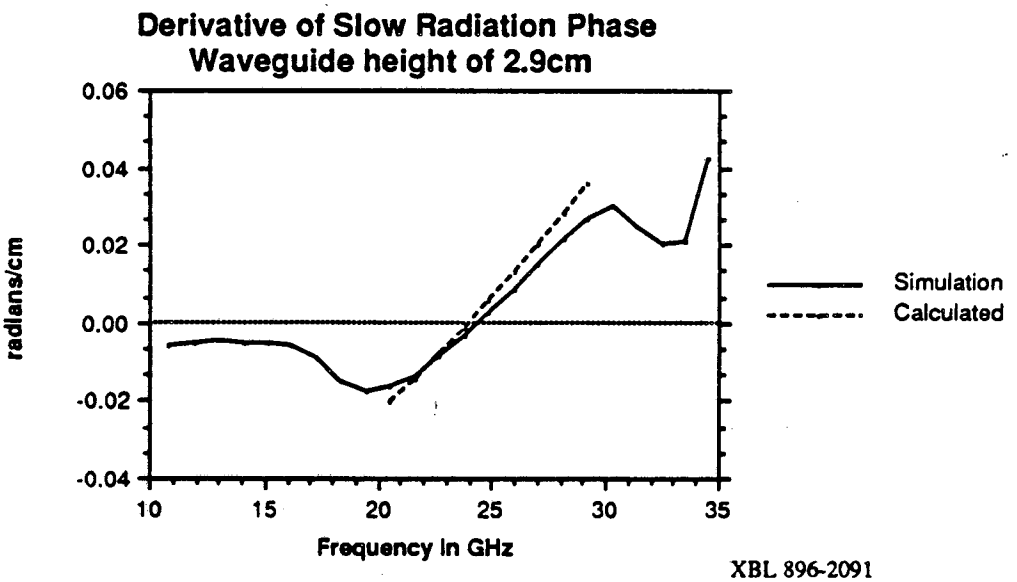

XBL 896-2091

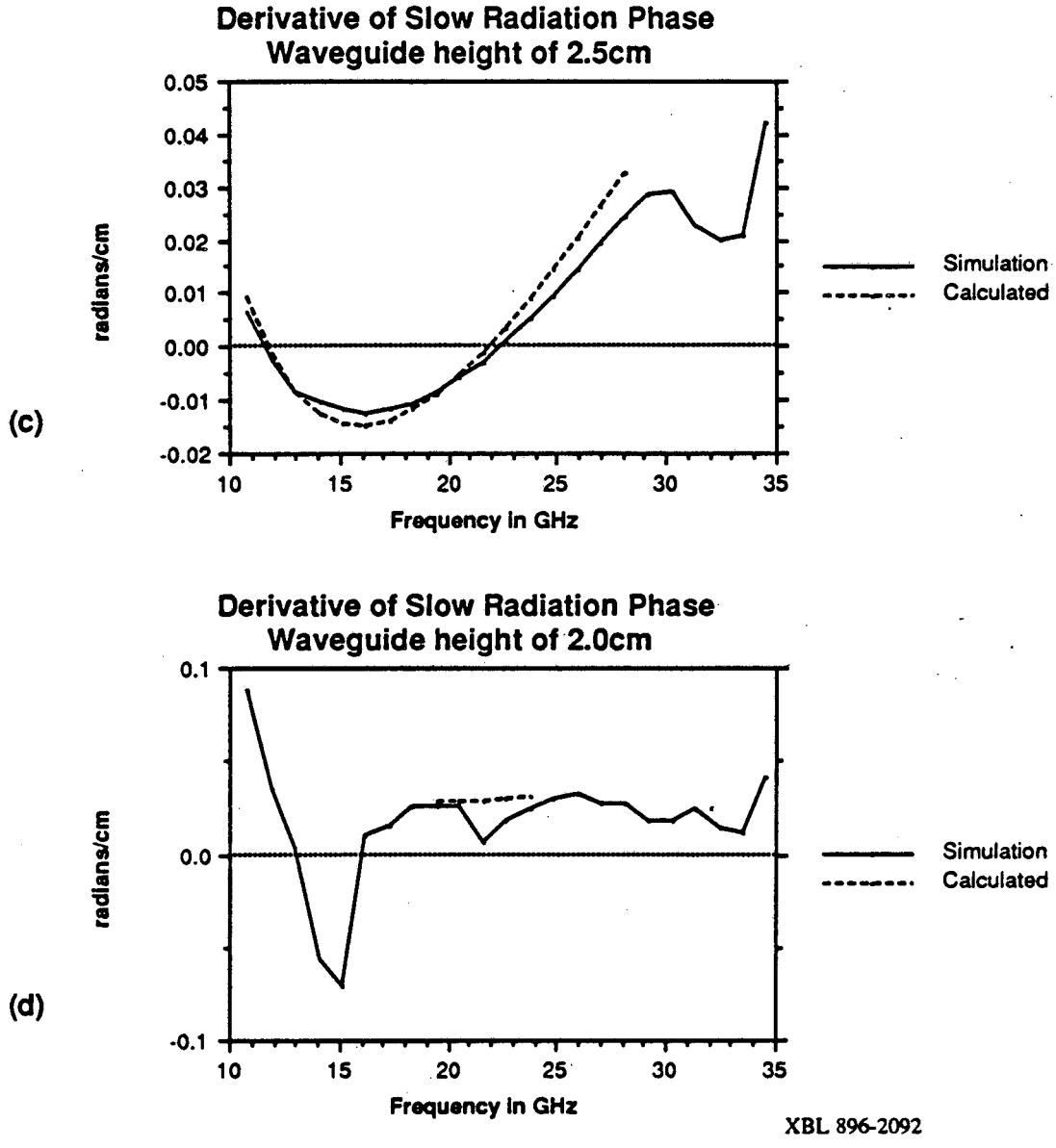

Figure 5.26 These are plots of the slope of the slowly varying phase of the various radiation frequencies which correspond to the imaginary part of the sideband gain. The curve designated *calculated* shows points only where the gain was nonzero and a definite value for the phase can be assigned. Note that where a peak is present in the gain curve, except for (d), the phase slope passes through zero. In (c) the double peak is then visible. In (d), exact phase matching can never be achieved. The curve passes through zero, but it appears more like noise in the simulation.

Note that for the cases where phase matching is possible, i.e. (a) through (c), the imaginary part of the gain passes through zero when there is a peak in the real gain curve. This is an additional way to determine the location of the sideband peak. In (c) for both figures, two Stokes wave peaks are visible. For the parameters given, one would expect the lower peak to be at 11.6 GHz from the relation (5.7.33b). There is quite good agreement. For (a) and (b) this peak exists, but is off the scale of the plots. For (d) there is only rough agreement with the theory. The regime in (d), however, is one where phase matching is impossible. Sideband gain can occur only because Δk_L is small enough. The curves don't match exactly because the dispersion analysis is rather sensitive to the inputs in this regime. Also the simulation curve looks somewhat noisy because the fit to an exponential is not as accurate as the other simulations. In all, the dispersion analysis seems to do a rather good job for predicting behavior in a three-wave process.

In Fig. 5.27 is a plot of sideband location versus waveguide dispersion γ_t. It shows both solutions of (5.7.33b) representing the upper and lower Stokes waves. For the upper Stokes wave, the peak moves away from the fundamental as the dispersion is increased. However, one eventually reaches a point at which phase matching is no longer possible. In this regime, the sideband peak starts moving back towards the fundamental.

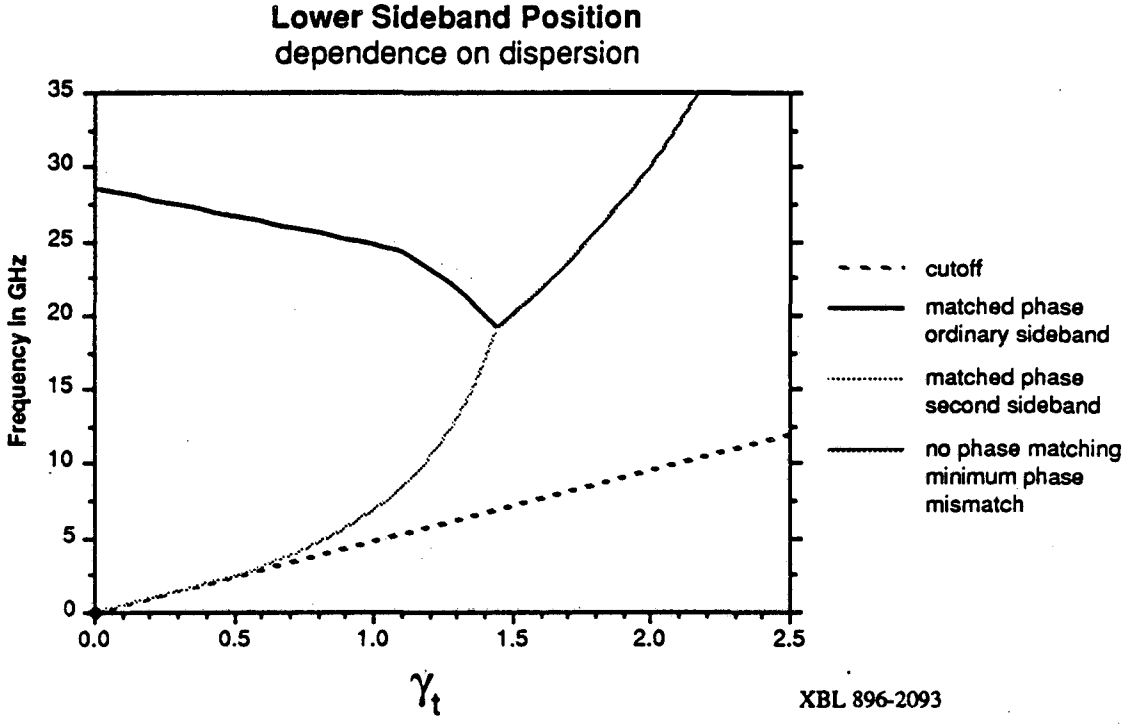

Figure 5.27 The various phase matching conditions for the lower FEL sideband are plotted. This uses the parameters of Table VI. When phase matching can be achieved, two sideband peaks are possible. For small dispersion, the lower peak is so close to the waveguide cutoff that it will probably not be seen. When phase matching becomes impossible, the peak starts to move back towards the fundamental.

Note that just because the phase matching condition gives a location for a sideband it doesn't mean that the sideband will be actually unstable and grow. For the parameters used here, the sideband is unstable up to about $\gamma_t \approx 1.6$. From previous analyses one expects something special to happen when $v_{group} = v_{particle}$. This happens at a little over $\gamma_t = 2.1$. We can see that even if the sideband was unstable, the sideband location would be exactly on top of the fundamental. Therefore, it is strictly impossible to see a sideband when $v_{group} = v_{particle}$, though this is an unnecessarily strong condition for no sideband growth.

5.9 Four-Wave Analysis

In the last section, it was shown that when the computer simulation was restricted to interactions between three waves, the agreement between the complicated computer simulation and the simple dispersion analysis performed was quite good. However, three-wave interactions cannot explain all of the phenomena of sideband generation in an FEL. Most obviously, the upper sideband is shown to grow when the FEL electron distribution is well centered in the bucket. In the three-wave analysis, the upper sideband never grows. In this section it will be shown that when four-wave interactions are allowed as well as three-wave interactions, then all the relevant physics of sideband growth can be explained.

We will start by utilizing all of the equations (5.7.30) and (5.7.31) to do a dispersion analysis of the four-wave system. The four waves are the FEL fundamental, the synchrotron oscillation, and the upper and lower FEL sidebands. If we assume that $\tilde{a}_{0L}$ and $\tilde{a}_{0u}$ both go as $e^{\rho z}$, then we can derive a sixth order equation for ρ that is

$$\rho^6 - 2i(k_L + k_u)\rho^5 + 4\left(k_\sigma^2 - k_L k_u\right)\rho^4 - 8ik_\sigma^2(k_L + k_u)\rho^3 + \left(F_L + F_u - 16k_\sigma^2 k_L k_u\right)\rho^2 +$$

$$2i[F_L(k_\sigma - k_u) - F_u(k_\sigma + k_L)]\rho + 4k_\sigma(F_L k_u - F_u k_L) = 0 \quad , \qquad (5.9.1)$$

where

$$F_L = \frac{8\pi Ie}{abm_e c^3} \frac{\cos\frac{m\pi}{2}\sin\frac{n\pi}{2}}{(1+\delta_{m0})} \frac{a_{w0}}{a_{s0}} \frac{k_\sigma^2}{\gamma} F_{ave}^L \frac{\omega_L^2}{\omega_s^2} \quad , \tag{5.9.2a}$$

and

$$F_u = \frac{8\pi Ie}{abm_e c^3} \frac{\cos\frac{m\pi}{2}\sin\frac{n\pi}{2}}{(1+\delta_{m0})} \frac{a_{w0}}{a_{s0}} \frac{k_\sigma^2}{\gamma} F_{ave}^u \frac{\omega_u^2}{\omega_s^2} \quad . \tag{5.9.2b}$$

The analysis is a little tricky now since from the matching conditions (5.7.33), there are two Stokes waves and two anti-Stokes waves. If we take the frequencies that people usually associate with sidebands(the upper Stokes and anti-Stokes waves represented by the +'s in 5.7.33), then the dispersion relation (5.9.1) has no real roots. This is not entirely unexpected since in a four-wave analysis, the two resulting frequencies must grow at the same rate, which is not what we observe in computer simulations of sidebands. As will be shown later, the upper sideband is driven by a process that is not related to exponential gain. However, if we examine roots at all the other possible combinations of Stokes and anti-Stokes waves, we find that there are indeed some frequencies that exhibit exponential growth in a four wave process. To actually observe this, the trick is to find a part of the spectrum where we expect to see growth from a four-wave process, but not a three-wave process. Otherwise the three-wave process, which generally exhibits higher growth, will completely overwhelm the four-wave process. According to the dispersion equation, the combination of the lower anti-Stokes wave and the upper Stokes wave is unstable. Also the lower Stokes wave and the upper anti-Stokes wave is unstable.

One unexpected property of the lower anti-Stokes wave is that it occurs well below the FEL fundamental. In fact for waveguides with small dispersion, it occurs near the waveguide cutoff.

In Figs. 5.28 and 5.29 we look at a situation where a four-wave instability can be easily distinguished from a three-wave process. Using the parameters of the previous section, we find that the waveguide with a height of 2.5 cm has a lower anti-Stokes wave at about 7.6 GHz. The three-wave dispersion relation predicts no exponential growth at this frequency. The four-wave dispersion equations predicts an exponential gain coefficient of 0.017 at this frequency.

Two simulations were done for this comparison. In the first simulation, only those frequencies below the fundamental were allowed to grow. Since the anti-Stokes peak that we are looking for is actually below both Stokes peaks and the fundamental, a four-wave process is still quite possible. This simulation should have a minimum of additional complications to the physics. The second simulation used the full spectrum necessary to include the contributions from all possible sideband peaks.

2.5cm waveguide case

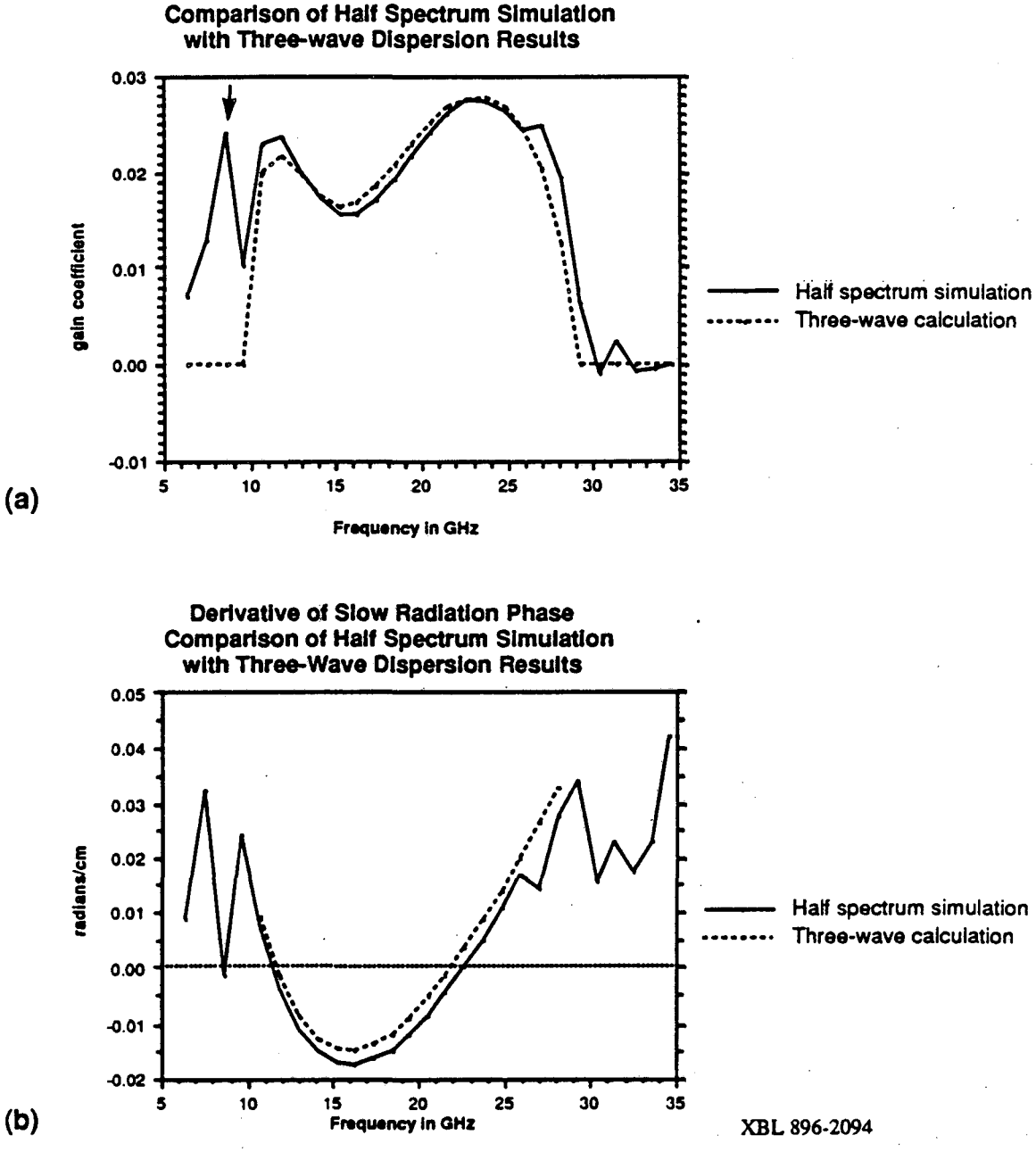

Figure 5.28 Comparison of single-particle-per-bucket computer simulation and three-wave dispersion analysis. In the simulation, only frequencies below the fundamental were allowed to grow. (a) is the real root and (b) is the imaginary root. An arrow in (a) marks where there is a substantial deviation between the simulation and the three-wave theory. The peak's location and height are just where they would be predicted by a four-wave dispersion analysis.

2.5cm waveguide case

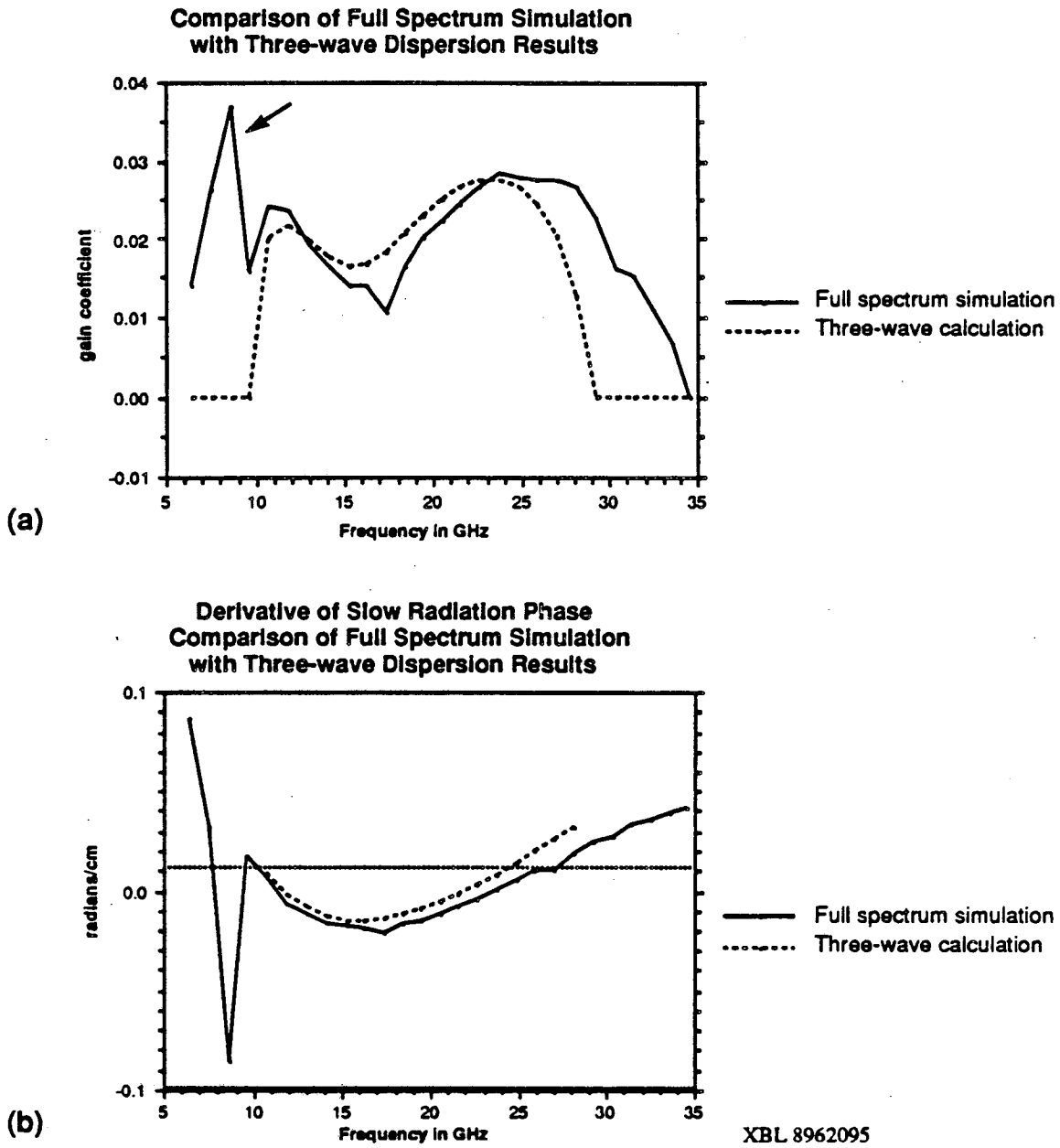

Figure 5.29 Comparison of single-particle-per-bucket computer simulation and three-wave dispersion analysis. In the simulation, the full spectrum was allowed to grow although only frequencies below the fundamental are plotted here. (a) is the real root and (b) is the imaginary root. An arrow in (a) marks where an additional peak is expected from a four-wave dispersion analysis. There is some discrepancy between the simulation and the calculated curve, much more than in 5.28. The additional differences must be from interaction with frequencies above the fundamental.

In Fig. 5.28, there is a comparison between a one particle per bucket computer simulation and the three-wave dispersion equation. For most of the spectrum, there is quite good agreement between the three-wave analysis and the simulation. There is, however, a major discrepancy below 10 GHz. The marked peak has a location close to the 7.6GHz peak predicted by a four-wave dispersion analysis, and is a reasonably good fit to an exponential. The height of the peak in the simulation is somewhat larger than the 0.017 predicted by the theory, though this is not unreasonable since this peak represents a four-wave interaction that includes the upper Stokes wave. Since this Stokes wave is also participating in a three-wave instability, it's higher growth rate should influence the gain of the lower anti-Stokes wave. The fact that the phase derivative curve passes through zero near the peak is strong evidence that it is a sideband interaction and not just the lower FEL resonance described in section 4.1.

The simulation in Fig. 5.29 is very similar to that of Fig. 5.28. In these simulations, frequencies above the fundamental were allowed to interact with those below the fundamental. There are small shifts in the location and height of the peaks on the sideband gain curve. We need some additional physics to explain these shifts.

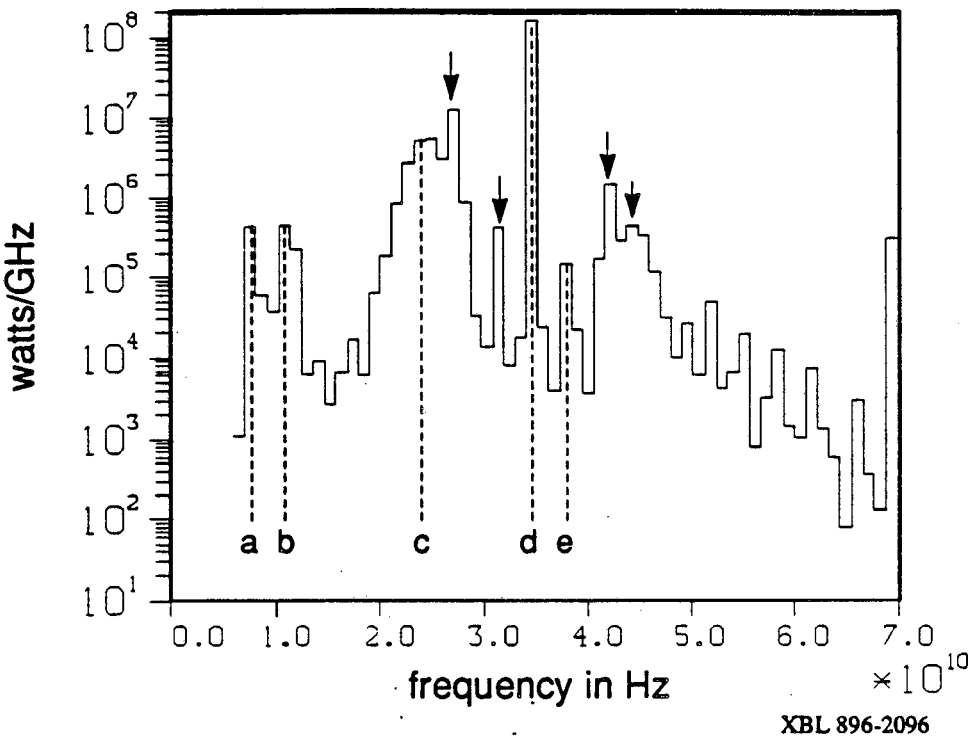

Figure 5.30 Full spectrum at 3.5 meters for the 2.5cm height waveguide. Dashed lines identify **a**, lower anti-Stokes wave; **b**, lower Stokes wave; **c**, upper Stokes wave; **d**, fundamental; **e**, upper anti-Stokes wave. The arrows show which peaks result from the beat wave of two strong peaks acting on the beam current.

Theoretically, the upper anti-Stokes wave and the lower Stokes wave can exhibit a four-wave instability. This upper anti-Stokes wave is predicted to be at about 38.7GHz. If we examine the spectrum of the full spectrum simulation shown in Fig. 5.30, this peak is visible, but it is not the peak that people usually assume is the upper sideband.

We need only one more physical process to explain the structure of the spectrum shown in Fig. 5.30. It is also a four-wave process, but it is not an exponential instability.

If there are two waves at different frequencies that both have a fairly large amount of power in them, then the beat wave created by these frequencies will form a moving ponderomotive well that can then act on the electron beam. The electron beam will be modulated by this potential. Radiation will be emitted at new frequencies that go as the old radiation frequencies plus or minus the frequency of the electron beam modulation. If this electron beam modulation moves at a speed close enough to the ponderomotive phase defined by the wiggler field and one of the new frequencies, then there will be substantial amplification of the new frequencies. This is not an instability. It is rather more similar to a pendulum forced at a frequency quite different from it's resonance frequency. Those peaks that are a result of this forcing are marked with arrows in Fig. 5.29. Now the need for the Stokes and anti-Stokes terminology is apparent. In free space where the sidebands are symmetric around the fundamental, there is no difference between the anti-Stokes wave and the forced upper sideband. In a waveguide, what people usually refer to as the upper sideband is actually a forced wave that is symmetrically located around the fundamental with the lower sideband. Dispersion causes the Stokes and anti-Stokes waves to be asymmectrically placed around the fundamental.

To illustrate the physics of what has just been described, a number of simulations were performed. The results are shown in Figs. 5.31 and 5.32. In these simulations, the single-particle-per-bucket simulation with the 2.5cm height waveguide was used. In addition to the fundamental, a signal at 5kW was injected at a frequency lower than the fundamental. To make the interpretation of the results easier, only those frequencies larger than the fundamental were allowed to grow.

What was observed was that the frequency that was the "mirror image" of the input frequency around the fundamental was driven quite hard and achieved large amplitudes in just 50cm. This is just what one would expect if it was a beat wave between the fundamental and the lower input frequency that was driving the current. This effect was rather insensitive to the value of the lower input frequency, which should indicate that this is not a resonance effect.

Fig. 5.32 shows the power in the forced frequency versus distance. Since the forced modulation of the electron beam moves at a different speed than optimal for amplifying the forced radiation frequency, the signal will be alternately amplified and damped.

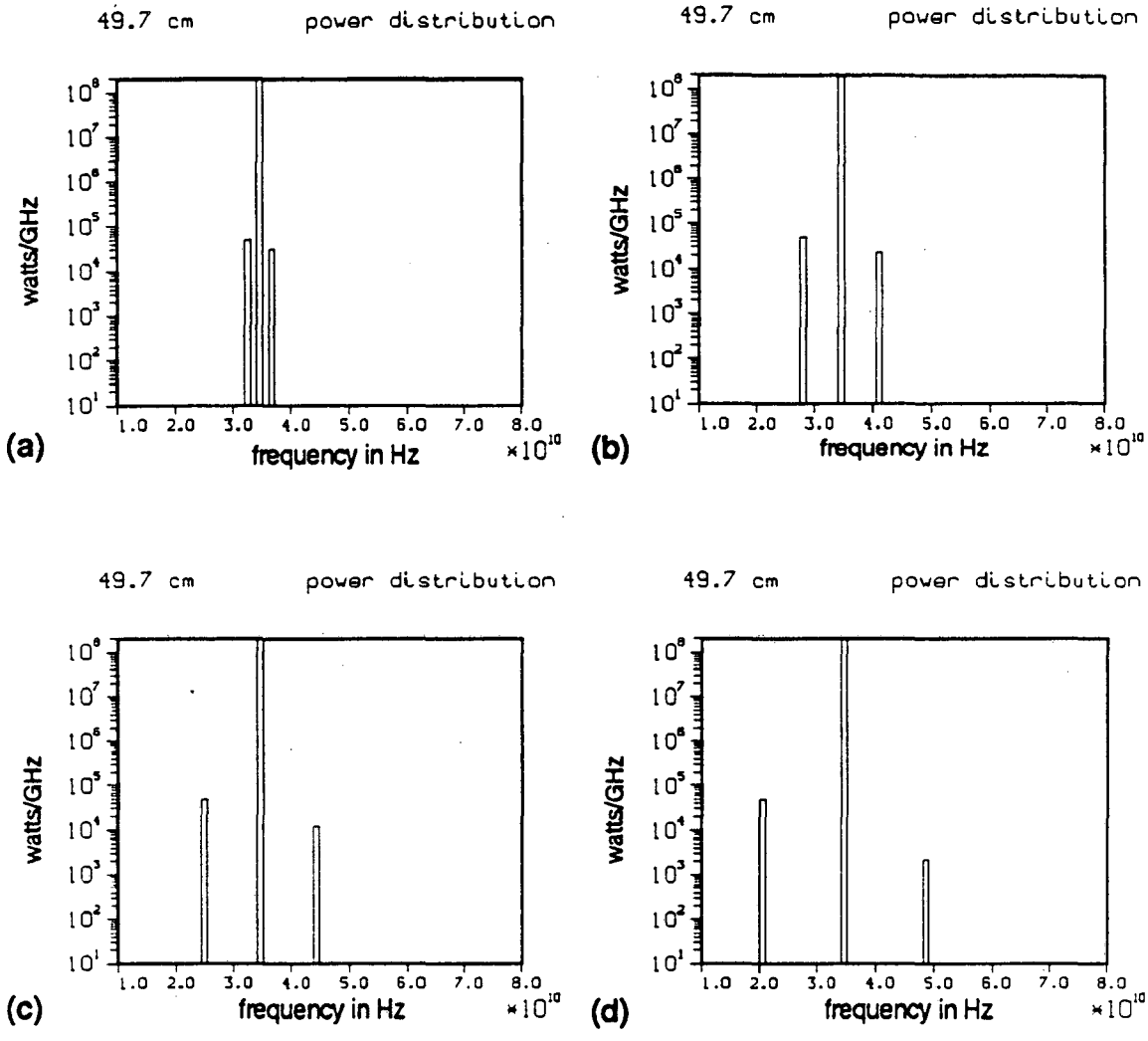

XBL 896-2097

Figure 5.31 Simulations all start with 200MW in the fundamental and 5kW at a lower frequency. Only frequencies larger than the fundamental are allowed to grow. The input frequencies are 32.4GHz, (a); 28.1GHz, (b); 24.9GHz, (c); 20.5, (d). Note that by 50cm, the upper forced frequency is almost the same in magnitude as the input frequency. This is rather insensitive to exactly what the input frequency actually is.

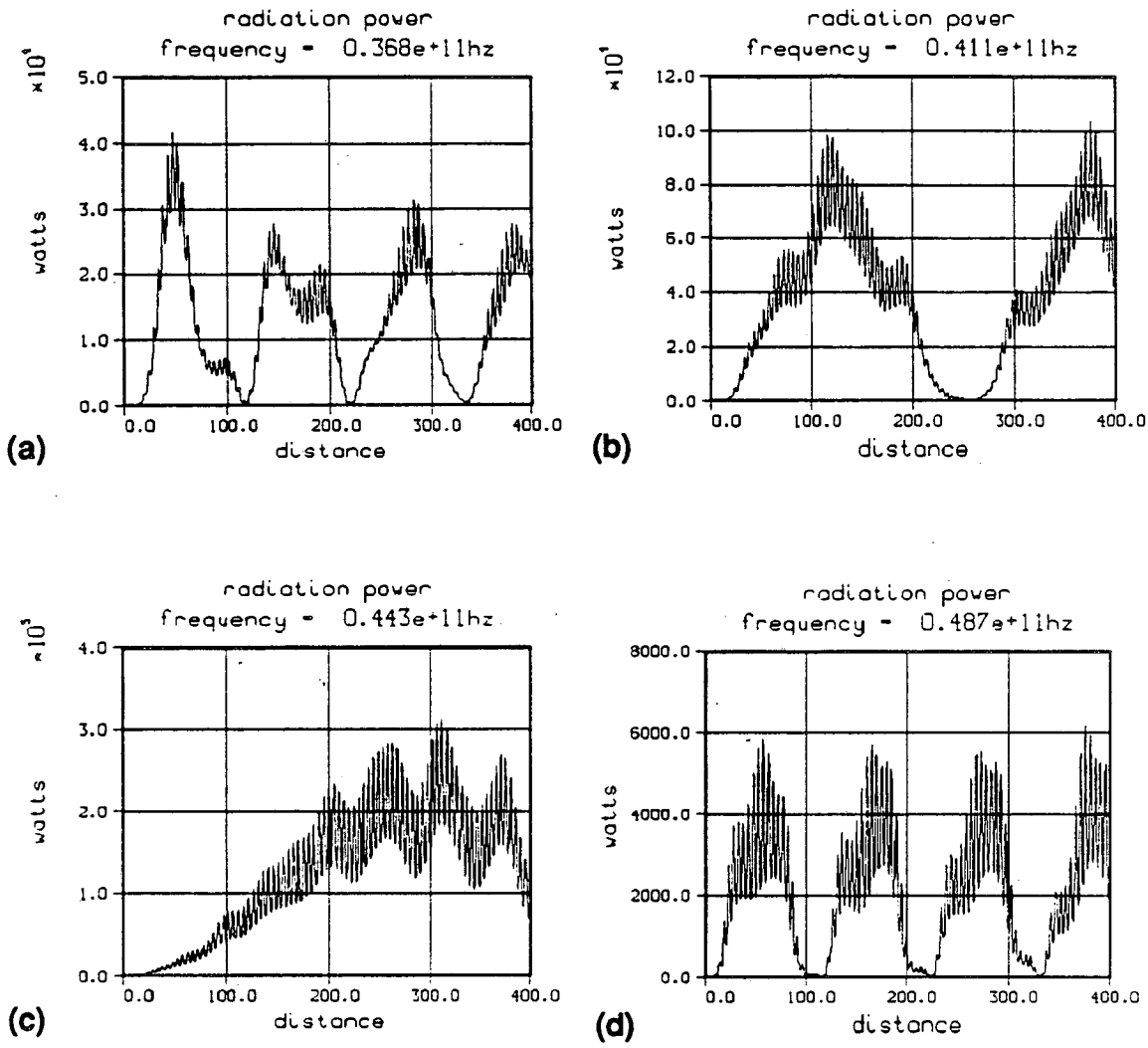

XBL 896-2098

Figure 5.32 Simulations all start with 200MW in the fundamental and 5kW at a lower frequency. Only frequencies larger than the fundamental are allowed to grow. The input frequencies are 32.4GHz, (a); 28.1GHz, (b); 24.9GHz, (c); 20.5, (d). Since the electron beam modulation moves at a different speed than the frequency that is being amplified, it will eventually get out of phase and the frequency that had been amplified will now be damped.

The upper lobe of the saturated FEL spectrum that has generally been labeled the upper sideband is in fact just frequencies that are amplified in this manner. Since the "upper" sideband lobe is just forced by the lower sideband lobe, it will not attain the same amplitude as the lower sideband unless the forced electron beam modulation is moving at exactly the same speed as the ponderomotive phase of the forced frequency. This amplification and subsequent damping can also explain why the upper lobe of the sideband spectrum is often seen to disappear after initial amplification. While any two frequencies with large power can interact in this fashion, it is more likely to observe spectra that have a shape that is symmetric around the fundamental, since initially the fundamental has the largest power of any frequency.

This beating of two frequencies can amplify a third frequency at the startup of an FEL as well as in the saturated regime. This will be shown in the next section. It is also further justification that this is not a process actually related to the sideband instability.

Thus we can see that sidebands are primarily driven by a three-wave instability, with the upper sideband spectrum resulting primarily through the lower sideband spectrum beating against the fundamental. In a waveguide, four-wave instabilities are also

possible and complicate the spectrum. In all, this section and the previous one contain all the physics necessary to describe the complicated spectrum shown in Fig. 5.30.

5.10 Explanation of ELF Sideband Results

Experiments were performed intended to measure sideband growth at the ELF facility at Livermore. In this section some simulations were performed to show that the experiment was flawed in that no amplification of sidebands could have been measured.

The experiment had the parameters shown in Table VII. The peak wiggler field was chosen to put the fundamental, at 36GHz, at the top of the gain curve. A tunable magnetron was used to inject at a second frequency that varied between 31GHz and 34GHz. A set of tunable filters was used to look at the spectrum from 31-36GHz and from 34-40GHz. No apparent amplification of the sideband(lower frequency) was observed.

Table VII. Simulation parameters

Relativistic energy γ	6.85	
Energy spread $\Delta\gamma$	±0.4	
Wiggler peak field	3.65	kG
Wiggler wavelength	9.8	cm
Beam current	900	amps
Waveguide size	9.8 × 2.9	cm
Input radiation:		
5kW at 36GHz (fundamental)		
1-5kW at 31-34GHz		

To see why this happened, we first have to look at the FEL gain curve. The curve in Fig. 5.33 is calculated by fitting an exponential curve to the radiation field amplitudes in the startup section of the experiment just described. Since the simulation used is 1-D, the results may not be accurate as far as exact experimental measurements are concerned, but the basic physics can be understood.

The first thing to note is that the gain curve fills the entire frequency regime that the measurements were made in. It would therefore be rather difficult to separate the gain due to the FEL sideband interaction and the gain due to FEL startup.

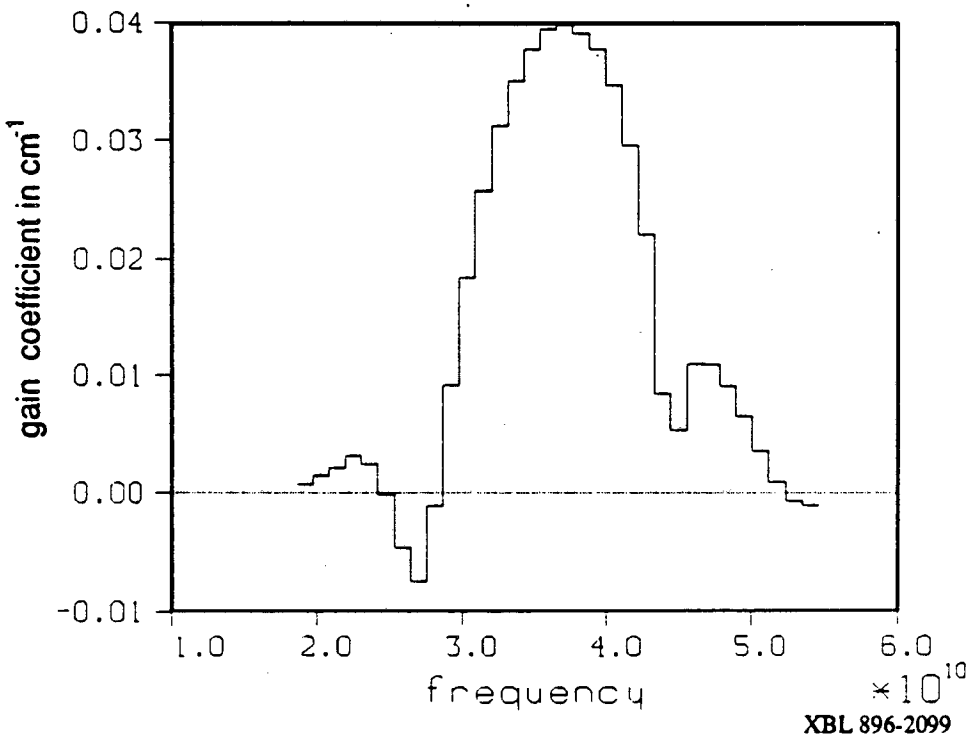

Figure 5.33 Startup gain curve for the experimental parameters of Table VII.

A second problem with the parameters used is illustrated in Fig. 5.34a. The gain curve for the lower sideband lies completely out of range of the lower input in the experiment. The lower sideband curve has a peak at 29.3GHz.

In the simulations that follow, we calculate first what the expected results would be if the tunable magnetron was set to give 5kW at 33.8GHz. The physics of this case has little to do with sidebands. In the next case, we will inject 5kW at the actual sideband frequency of 29.3GHz. It will be seen from Fig. 5.33 that this frequency has a startup gain close to zero. Therefore, if strong gain is observed it should be due to sideband interaction.

Fig. 5.35 shows the power output of the simulation for the input signal at 33.8GHz. This shows a severe case of the forcing of new frequencies from the beating of two strong radiation waves as described in the previous section. The forcing is strong enough to create many frequencies since both input signals are high on the gain curve and are strongly amplified. Note that in the plot of the total power versus distance there is a local saturation of the total power at a little over 150MW near 1.5 meter into the wiggler. This is the same as the case where only the fundamental frequency was

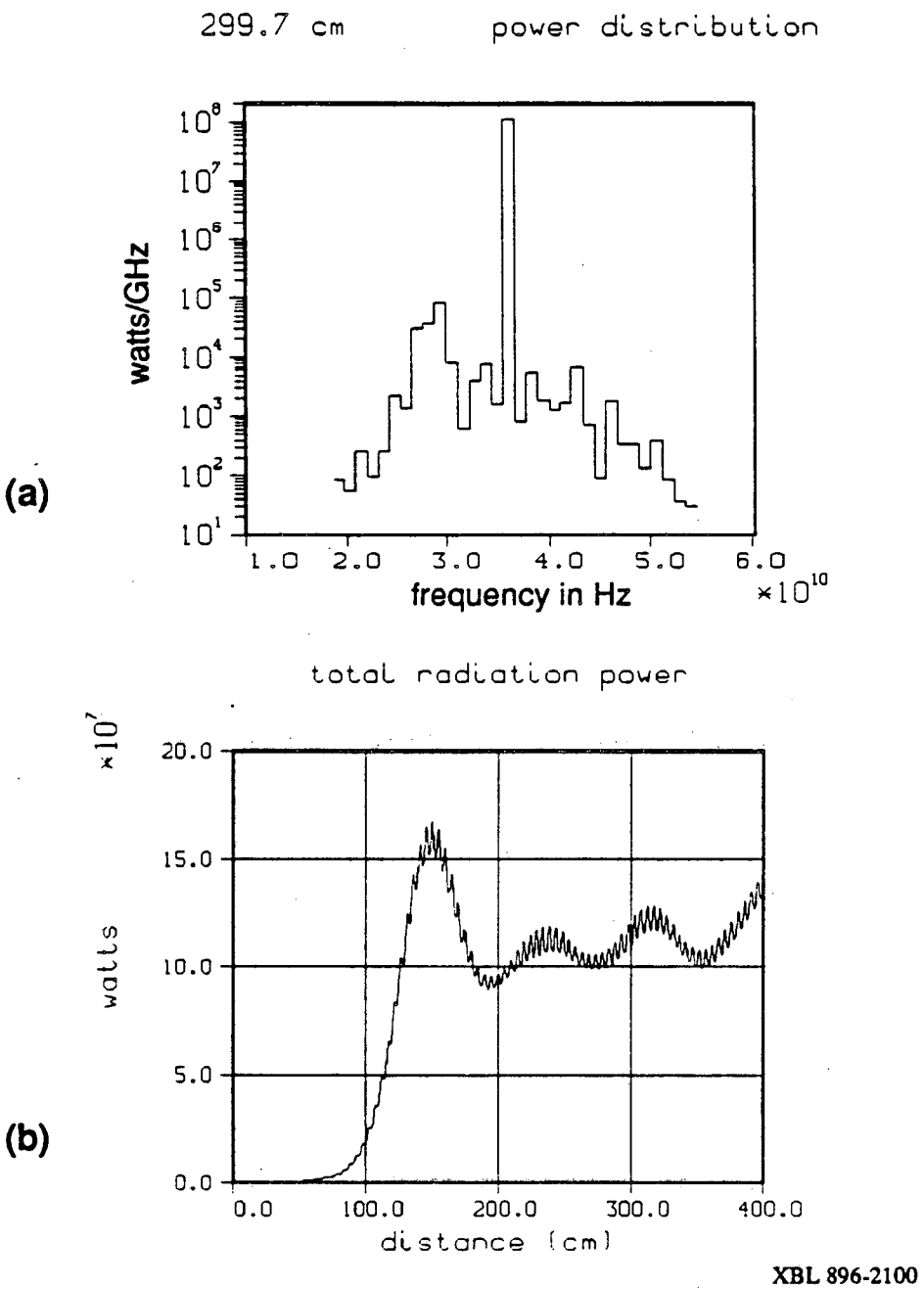

Figure 5.34 Plots for the simulation where only the fundamental was injected. Lower sideband peak is at about 29.3GHz.

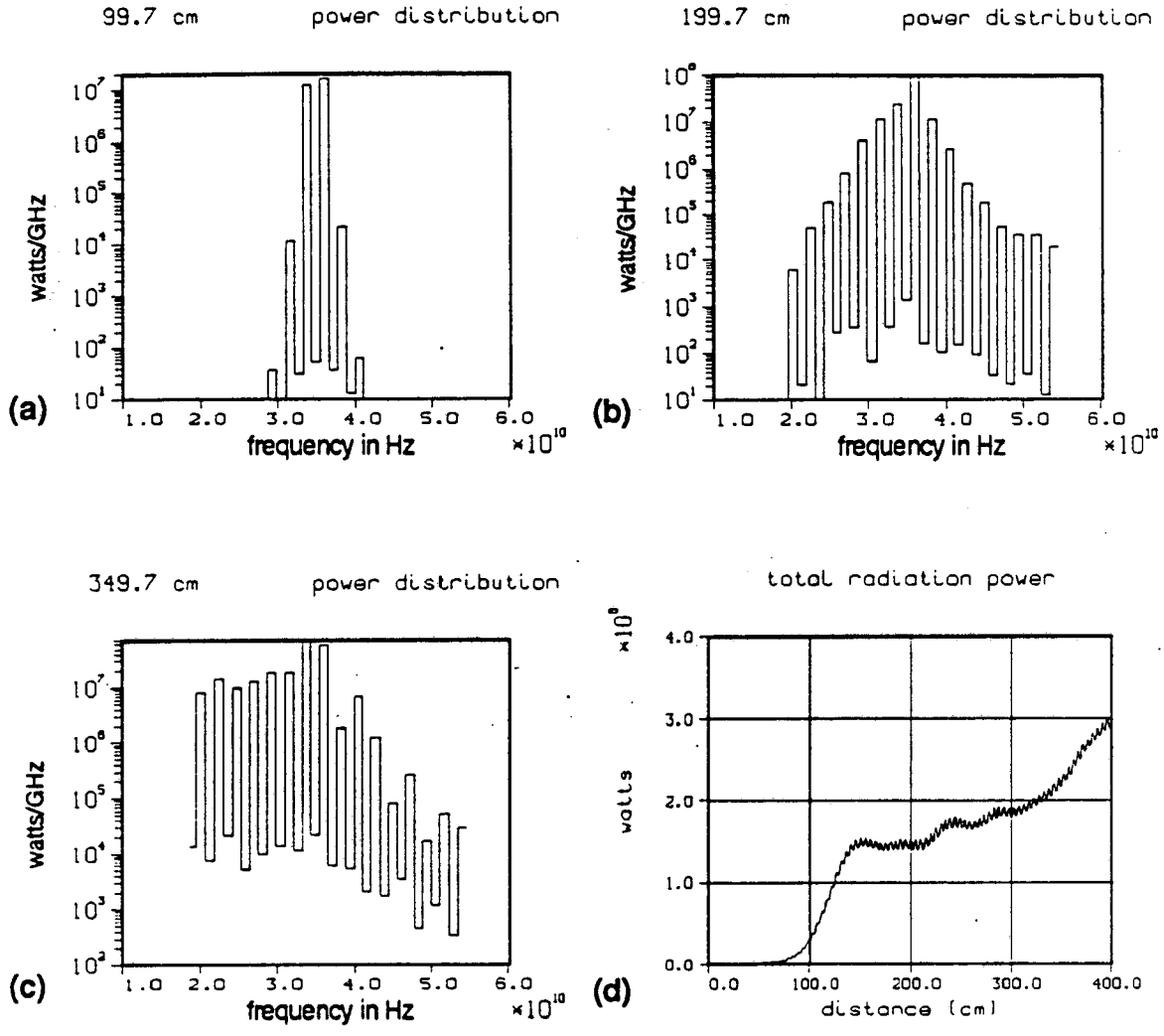

XBL 896-2101

Figure 5.35 Power produced with inputs of 36GHz and 33.8GHz at 5kW each. The peak of the gain curve is set to be close to 36GHz. The beating of the waves creates waves at new frequencies that are separated by the frequency of the beat wave. Since there is strong amplification, these waves in turn produce others. Near the end of the wiggler in (c), much of the radiation fills the spectrum below the fundamental frequency (36GHz). The simulation only calculates down to 18GHz so it is possible that there is even more power in the spectrum below this point.

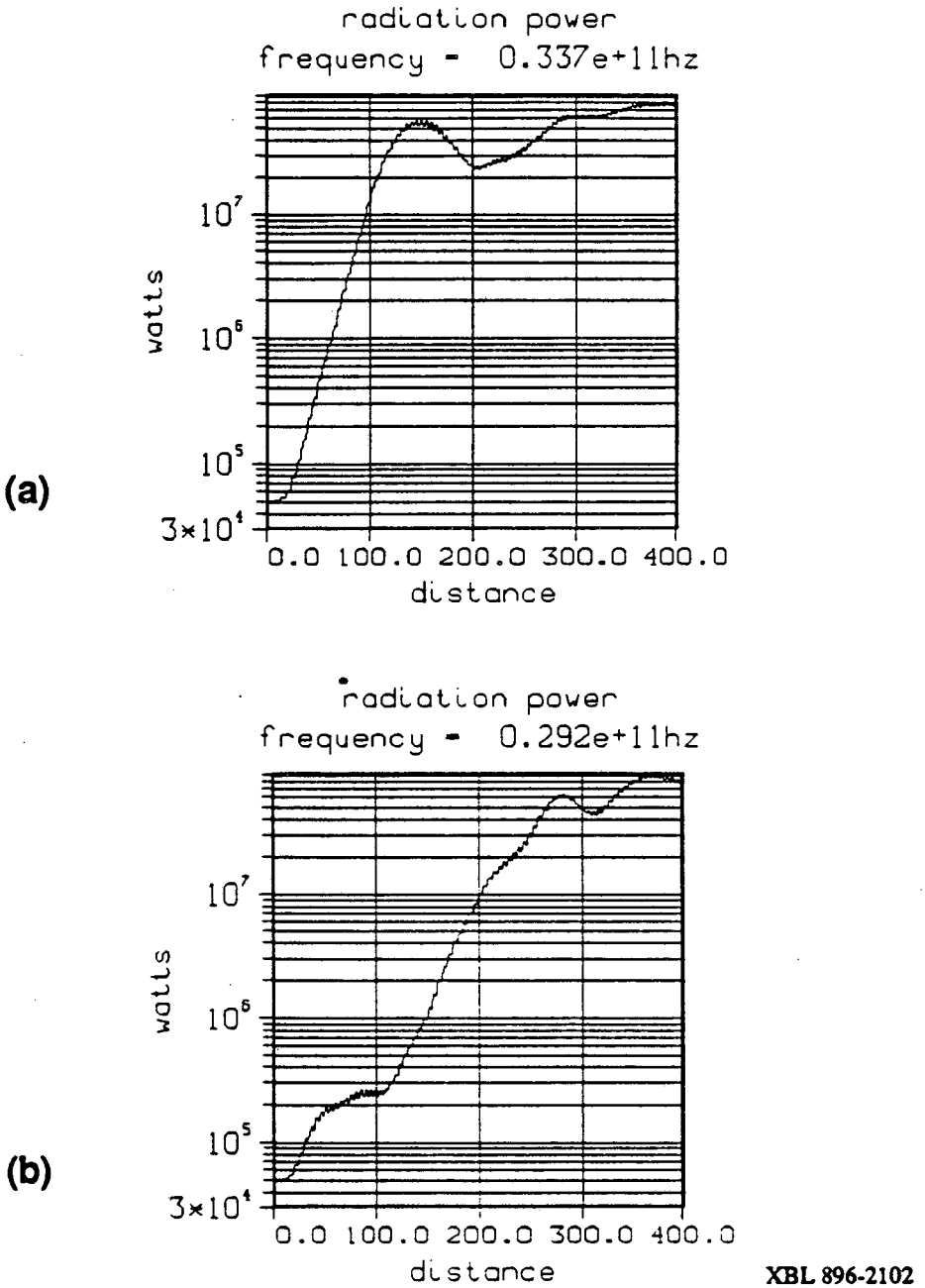

Figure 5.36 Plots of the power of the lower injected frequency for two different frequencies. In (a), the injected frequency is on the gain curve and just gets amplified exponentially like the fundamental with slightly lower gain. In (b) the input signal is off the gain curve and therefore experiences little gain after the startup region until the fundamental reaches its eventual saturation value. In this regime the signal is at the peak of the sideband gain curve and it is amplified exponentially.

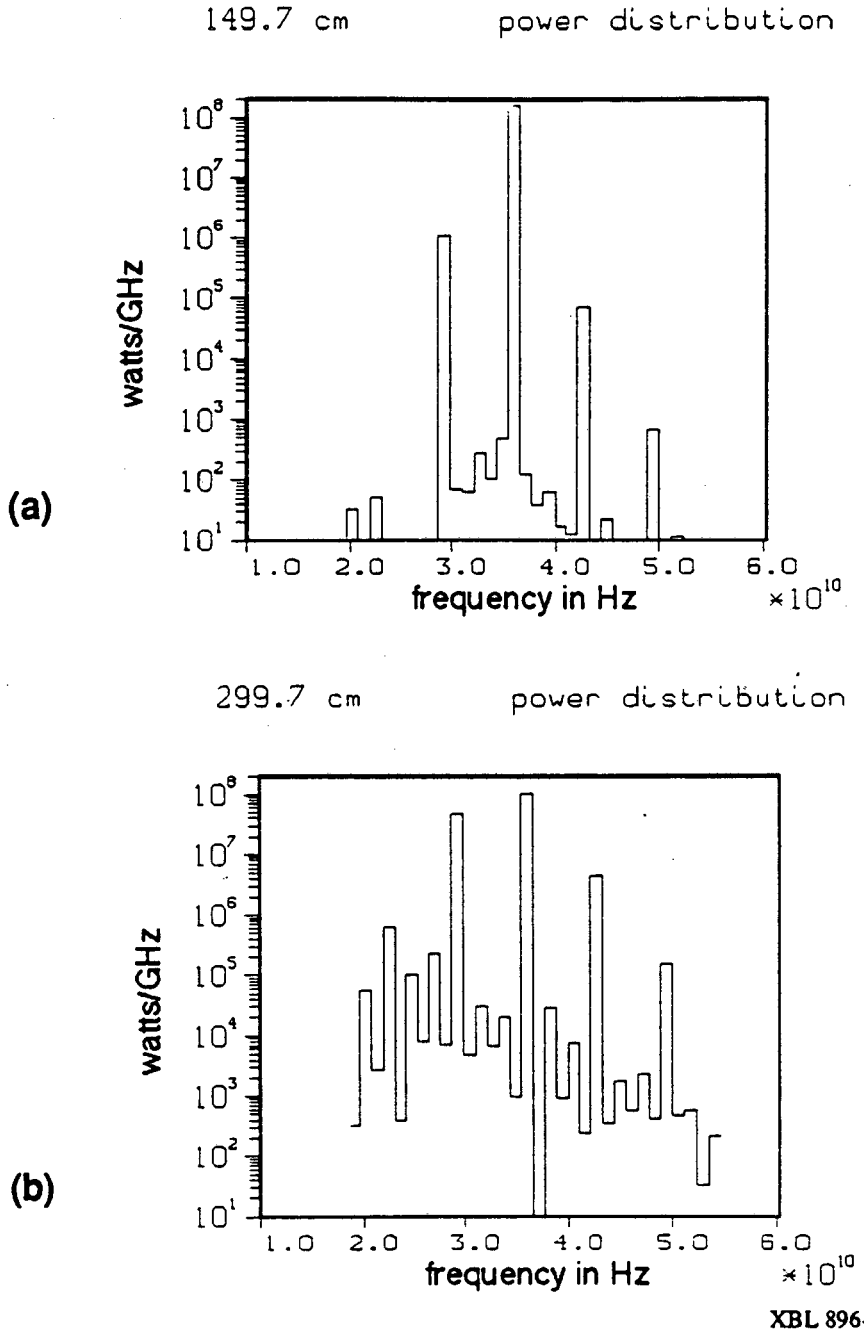

Figure 5.37 When the lower input signal is at 29.3GHz, it is possible to see the amplification of the sidebands. Near the end of the wiggler, in (b), it can be seen that there is significant power only at the fundamental and the lower and upper sidebands.

amplified. After this point the total power increases due to more power being pumped into additional frequency components. A large proportion of the power produced could not have been measured in the experiment since it is in frequencies outside the tunable filters. Thus the experiment might have measured a decrease in total power produced.

It might have been possible to see sideband amplification if the correct lower frequency was used as input. It is fortuitous that the peak of the sideband gain lies at a point that has near zero gain in an unbunched beam. Fig. 5.36 shows the power of the lower injected signal versus distance for both the previous example and for a 29.3GHz lower input. One can see that the 33.8GHz input is amplified exponentially from the beginning, just like the fundamental. The 29.3GHz case shows little gain before the saturated regime is reached. After the electron bunching is complete, there is exponential gain. Fig. 5.37 shows that for the given length of wiggler, there is significant power primarily in the fundamental and the upper and lower sidebands. Thus the simulation shows that if one looked at the right frequencies, one might have been able to measure sideband gain.

It has been pointed out by Bill Fawley, that in a simulation that included space charge effects, the synchrotron wavelength would be increased. According to some calculations he has made, this would place the lower sideband at about 32GHz which was within the range of frequencies searched in the experiment. However, because the lower frequency was on the gain curve and because the injected signals were of comparable intensity, the beat interaction between the two frequencies would have overpowered any sideband interaction. It might have been possible to measure sidebands in this case, but only if the signal injected at the sideband frequency was many orders of magnitude less than thefundamental. Even then, a very careful measurement of the gain curve in both the startup regime and the saturated regime would have been necessary to establish sideband gain.

The sideband amplification experiment did not work because of the fact that the injected signals were on the fundamental gain curve. If all radiation is injected at the beginning of the FEL, then a sideband gain experiment is quite difficult. If one could design an experiment such that the sideband signal to be amplified is injected after saturation of the FEL, then the physics of the experimental results would be much clearer.

Chapter 6

Conclusion

6 Conclusion

In this work the sideband instability has been explained in a manner that gives a direct physical interpretation. While the sideband instability in a waveguide has been accurately described, it also provides insight into the FEL sideband instability in general.

For FEL sidebands in free space, it is difficult to use the output spectrum to differentiate between a stimulated scattering process and a system of forced currents. The upper sideband is where the anti-Stokes wave is predicted to be and the lower sideband is where the Stokes wave is predicted to be. The way to prove the case is to design a system that can preferentially damp either the upper or lower sideband. If the lower sideband is damped, then the sideband instability should be completely absent. If the upper sideband is damped, the sideband instability should still cause amplification of the lower sideband. An oscillator with some form of Fabry-Perot device in the optics might be able to accomplish this experiment.

The analysis of this thesis produced some unexpected results that can be tested. Fully four sideband peaks are possible from stimulated scattering processes in a

waveguide. These consist of two Stokes waves and two anti-Stokes waves. Three of these peaks are below the fundamental in frequency(two Stokes and one anti-Stokes) and one is above the fundamental(one anti-Stokes). Because of waveguide dispersion, no pair of frequencies are located symmetrically around the fundamental. Therefore, additional peaks in the sideband spectrum are possible from beat wave interactions between any combination of the FEL fundamental and the four stimulated scattering peaks.

The primary driving force of the FEL sideband instability is a three-wave interaction where the three waves are the FEL fundamental, the electron synchrotron oscillation, and the Stokes wave(lower sideband). What people have called the upper sideband is driven by a beat wave interaction between the FEL fundamental and the Stokes wave. In free space, all frequencies move at about the speed of light, and the sidebands tend to be rather close to the fundamental. For these circumstances we would expect the lower and upper sideband power to be roughly equal. In a waveguide where the upper and lower sidebands can move at substantially different speeds and can be relatively far from the fundamental, it has often been observed in computer simulations that the upper sideband is orders of magnitude less in power than the lower sideband.The reason for this is that the beat wave between the FEL fundamental and the lower sideband can no longer interact strongly with the upper sideband.

In a waveguide it is also possible to have instabilities between four waves. These interactions are weaker than the three-wave instabilities and are therefore difficult to observe unless the peaks are located reasonably far from the other peaks in the spectrum. Not all combinations of Stokes and anti-Stokes waves can interact in this fashion.

The sideband instability disappears when the three-waves scattering process is no longer possible. It was shown in sections 5.8 and 5.9 that at the frequency of the sideband peak, there is no slowly varying phase. This means that the frequency at the sideband peak travels at the same speed as it would travel in a waveguide without the electron beam. The sideband peaks exist where this phase matching occurs or where the phase mismatch is at a minimum. If the phase mismatch is too great, then no amplification of the sidebands is possible. This occurs well before the group velocity of the FEL fundamental reaches the electron beam velocity.

The work performed in this thesis suggests some possibilities for future studies of FEL sidebands in waveguides. Some suggestions follow.

Effects due to nonlinearities in the FEL bucket could be examined by deriving equations similar to (5.7.26) and (5.7.27) where ψ' is not assumed to be small. This would be equivalent to studying the coupling between a harmonic oscillator(radiation Helmholtz equation) and a fully nonlinear pendulum(particle motion). Effects due to finite electron distributions could be examined by using the equations of motion in a kinetic analysis similar to Kroll and Rosenbluth[42] or Riyopoulos and Tang[46].

The work of section 5.7 could easily be expanded to include coupling between transverse modes at different frequencies in the saturated FEL regime. This is different than the thesis work of Jonathan Wurtele where the coupling between transverse modes of the same frequency was examined[5]. This could be accomplished by writing k_s and k_π as k_s^{mn} and k_π^{mn}, where the waveguide mode for each radiation wave is not necessarily the same. The phase matching conditions (5.7.29) would then be used to see which waves could interact strongly.

References

[1] N.M. Kroll, P.L. Morton, M.N. Rosenbluth, *IEEE J. Quant. Elect.*, **QE-17**, 1436 (1981).

[2] R.Bonifacio, C. Pelligrini, L.M. Narducci, *Optics Comm.*, **50**, 373 (1984).

[3] A. Szoke, V.K. Neil, and D. Prosnitz, *Physics of Quantum Electronics, Vol. 7*, Addison-Wesley, Reading, MA, 175(1980).

[4] Jackson, J.D., *Classical Electrodynamics*, 2nd Ed., Wiley, New York(1975).

[5] J.S. Wurtele, PhD Thesis, Univ. of Calif., Berkeley (1985).

[6] W.B.Colson, *Physics of Quantum Electronics, Vol. 5*, Addison-Wesley, Reading, MA, 157(1978).

[7] A.J. Lichtenberg and M.A. Lieberman, *Regular and Stochastic Motion*, Springer-Verlag, New York(1983).

[8] Garrison, and Wong, *Physics of Quantum Electronics, Vol. 8*, Addison-Wesley, Reading, MA, 349(1982).

[9] A.M.Sessler and E.J. Sternbach, "Scaling of the FEL Equations and Hamiltonian Formulation of an FEL," Lawrence Livermore National Laboratory ELF note #95(1984).

[10] E.J. Sternbach, "Comments and Errata on Scaling of the FEL Equations and Hamiltonian Formulation of an FEL," Lawrence Livermore National Laboratory ELF note #104(1984).

[11] R.Bonifacio, F. Casagrande, C. Pelligrini, *Optics Comm.*, **61**, 55 (1987).

[12] E.J. Sternbach, "Generalization of the KMR FEL Equations for the Low Energy Regime," Lawrence Livermore National Laboratory Research Memo #88-26.

[13] T.J. Orzechowski et al., *Nuc. Instr. and Meth.*, **A250**, 144(1986).

[14] G.N. Watson, *A Treatise on the Theory of Bessel Functions, 2nd Ed.*, Cambridge University Press, London, Chap. 2(1962).

[15] N.M. Kroll and W.A. McMullin, *Phys. Rev. A*, **17**, 300(1978).

[16] J.B. Murphy, C. Pellegrini, and R. Bonifacio, *Optics Comm.*, **53**, 197(1985).

[17] W.B. Colson and A.M. Sessler,"Free Electron Lasers,"*Annual Reviews of Nuclear and Particle Science*, **35**, 25(1985).

[18] J.M.J. Madey, *Nuovo Cimento*, **B50**, 64(1979).

[19] A. Szoke, V.K. Neil, and D. Prosnitz, *Physics of Quantum Electronics, Vol. 7*, Addison-Wesley, Reading, MA, 571(1980).

[20] T.J. Orzechowski et al., *Phys. Rev. Lett.*, **57**, 2172(1986).

[21] J.S. Wurtele, A.I.P. Conf. Proc. on Laser Acceleration of Particles, Malibu 1985, p. 305.

[22] Sternbach, E.J., *Nuc. Instr.and Meth.*, **A272**,323(1988).

[23] Eyges,L., *The Classical Electromagnetic Field*, Dover, New York(1980).

[24] R. Courant and D. Hilbert, Methods of Mathematical Physics, 1st Ed., Interscience, London, Chap. 5(1953).

[25] Morse and Feshbach, *Methods of Theoretical Physics Vol. I* , Chap. 7, McGraw-Hill, New York (1953).

[26] Bateman, *Tables of Integral Transforms Vol. I*, McGraw-Hill, New York(1954).

[27] E.J. Sternbach, "Formalism for the Study of Multiple Frequency Effects in a Waveguide FEL," Lawrence Livermore National Laboratory Research Memo #88-27.

[28] M. Born and E. Wolf, *Principles of Optics, 6th Ed.*, Pergamon, New York, p.112 (1980).

[29] A.P. Banford, The Transport of Charged Particle Beams, E. & F.N. Spon Ltd., London(1966).

[30] A. Yariv, *Quantum Electronics, 2nd Ed.*, Wiley, New York, Chap. 6(1975).

[31] E.T. Scharlemann, "Single -pass Free Electron Laser Amplifiers," in *Free Electron Laser Handbook*, Ed. Colson, Pellegrini, Renieri, Elsevier Science Publishing, New York, to be published.

[32] E.T. Scharlemann, *SPIE*, **738**, 129(1987).

[33] Y.J. Chen, E.T. Scharlemann, A.M. Sessler, *Nuc. Instr. and Meth.*, **A272**, 485(1988).

[34] A.Ting, P. Sprangle, B. Hafizi, C.M. Tang, "Guided Radiation Beams in Free Electron Lasers," NRL Memorandum Report 6207.

[35] E.T. Scharlemann, W.M. Fawley, B.R. Anderson, and T.J. Orzechowski, *Nuc. Instr. and Meth.*, **A250**, 150(1986).

[36] W.M. Fawley, D. Prosnitz, E.T. Scharlemann, *Phys. Rev.*, **A30**, 2472 (1984).

[37] E.T. Scharlemann, J. Appl. Phys., 58, 2154(1985).

[38] T.J. Orzechowski and E.T. Scharlemann, "The C-Band Mode in ELF," Lawrence Livermore National Laboratory ELF note #122P&E(1985).

[39] E.J. Sternbach, "Efficiency Enhancement in Microwave FELs," Lawrence Livermore National Laboratory ELF note #130P(1986).

[40] A. Sharma and V.K. Tripathi, *Physics of Fluids*, **31**, 3375(1988).

[41] C. Joshi et al., *IEEE J. Quant. Electr.*, **QE-23**, 1571(1987).

[42] N.M. Kroll and M.N. Rosenbluth, "Sideband Instabilities in Trapped Particle Free-Electron Lasers" in *Physics of Quantum Electronics, Vol. 7*, (Addison-Wesley), p.147.

[43] W.B. Colson, *Nuc. Instr. and Meth.*, **A259**, 168(1987).

[44] R.C. Davidson and J.S. Wurtele, *Phys. Fluids*, **30**, 557(1987).

[45] R.C. Davidson and J.S. Wurtele, *Phys. Fluids*, **30**, 2825(1987).

[46] S. Riyopoulos and C.M. Tang, "The Structure of the Sideband Spectrum in Free Electron Lasers," Naval Research Laboratory, NRL Memorandum Report 6118.

[47] S. Riyopoulos and C.M. Tang, "Stochastic Electron Detrapping in FEL's Caused by Sidebands,"*Nuc. Instr. and Meth.*, **A272**, 448(1988).

[48] W.M. Sharp and S.S. Yu, "Validity of 1D Free Electron Laser Sideband Models," *Nuc. Instr. and Meth.*, **A272**, 397(1988).

[49] W.M. Sharp and S.S. Yu, "2-D Vlasov Treatment of FEL Sidebands," Lawrence Livermore National Laboratory, UCRL-94846(Submitted to *The Physics of Fluids*).

[50] W.M. Fawley, E.T. Scharlemann, S.S. Yu, A.M. Sessler, E.J. Sternbach, "Stabilization of the Sideband Instability in the Two-Beam Accelerator," Lawrence Livermore National Laboratory TBA note #30(1986).

[51] S.S. Yu, W.M. Sharp, W.M. Fawley, E.T. Scharlemann, A.M. Sessler, E.J. Sternbach, *Nuc. Instr. and Meth.*, **A259**, 219(1987).

[52] J. Masud et al., *Phys. Rev. Lett.*, **58**, 763(1987).

[53] K. Kim, *Nuc. Instr. and Meth.*, **A259**, 396(1987).

[54] Y.R. Shen, *The Principles of Nonlinear Optics*, John Wiley &Sons, New York (1984), chapter 9.

[55] A. Yariv, *Quantum Electronics, 2nd Ed.*, John Wiley & Sons, New York(1975), chapter 17.

[56] T.J. Orzechowski, J.C. Clark, W.M. Fawley, D.B. Hopkins, A.M. Sessler, and A.L. Throop, "Amplification of the Sidebands in ELF," Lawrence Livermore National Laboratory ELF note #131(1986).

[57] A.L. Throop, personal communication.

[58] T.C. Marshall, *Free-Electron Lasers*, Macmillan, New York(1985).

[59] D.A.G. Deacon, L.R. Elias, J.M.J. Madey, G.J. Ramian, H.A. Schwettman, and T.I. Smith, *Phys. Rev. Lett.*, **38**, 892(1977).

[60] M. Billardon, P. Elleaume, J.M. Ortega, C. Bazin, M. Bergher, M. Velghe, Y. Petroff, D.A.G. Deacon, K.E. Robinson, and J.M.J. Madey, *Phys. Rev. Lett.*, **51**, 1652(1983).

[61] T.J. Orzechowski et al., *Phys. Rev. Lett.*, **54**, 889(1985).

[62] L.R. Elias and G. Ramian, *Free Electron Generators of Coherent Radiation*, eds., C.A. Brau, S.F. Jacobs, and M.O. Scully, SPIE, **453**, 137(1983).

LAWRENCE BERKELEY LABORATORY
TECHNICAL INFORMATION DEPARTMENT
1 CYCLOTRON ROAD
BERKELEY, CALIFORNIA 94720